Dissertation
submitted to the
Combined Faculties for
Natural Sciences and Mathematics of the
Ruperto-Carola University of Heidelberg, Germany
for the Degree of
Doctor of Natural Sciences

presented by
Dipl.-Ing. Holger Frank Mest
born in Ziegenhain

Oral Examination: Jul 6th, 2011

Measurement of the β-Asymmetry in the Decay of Free Polarized Neutrons with the Spectrometer PERKEO III

Referees: Prof. Dr. Hartmut Abele
Prof. Dr. Hans-Christian Schultz-Coulon

Abstract: Measurement of the β-Asymmetry in the Decay of Free Polarized Neutrons with the Spectrometer PERKEO III

The charged current in Weak Interaction, mediated by the W-boson, is maximally parity violating in the Standard Model of particle physics. Studies of neutron decay are very suitable to get access to this property of the Standard Model due to the absence of a nuclear structure, compared with nuclear beta decay. High precision experiments in this field are intended to test the Standard Model and the extensions.

In this thesis the first asymmetry measurement with the new neutron decay spectrometer PERKEO III is described. During a nine-month beamtime at the Institute Laue Langevin the β-asymmetry A in the decay of free polarized neutrons was measured. For the first time, a pulsed neutron beam was used. This significantly improved the experimental systematics. The data analysis confirmed the clean systematics, resulting in new values and improved uncertainties on the β-asymmetry A and the ratio of axialvector to vector coupling λ. Compared to the current world average given by the Particle Data Group (PDG), the uncertainty of this measurement is smaller by a factor of 5.

Zusammenfassung: Messung der β-Asymmetrie im Zerfall freier polarisierter Neutronen mit dem Spektrometer PERKEO III

Im Standardmodell der Teilchenphysik ist der geladene Strom der schwachen Wechselwirkung, vermittelt durch das W-Boson, maximal paritätsverletzend. Untersuchungen zum Zerfall freier Neutronen sind besonders geeignet, um Zugang zu dieser Eigenschaft des Standardmodells zu erhalten, da hier Formfaktor-Korrekturen deutlich kleiner sind als beim Kern-Betazerfall. Präzisionsexperimente auf diesem Gebiet sind demzufolge in der Lage, das Standardmodell und seine Erweiterungen zu überprüfen und gegebenenfalls auszuschließen.

Diese Arbeit beschreibt die aktuelle Asymmetrie Messung mit dem neuen Spektrometer PERKEO III. Während einer neun-monatigen Strahlzeit am Institut Laue Langevin wurde die Elektron-Asymmetrie im Zerfall freier polarisierter Neutronen gemessen. Erstmalig wurde hierbei ein gepulster Neutronenstrahl verwendet, wodurch einige systematische Effekte signifikant verbessert werden konnten. Dies wurde durch die Auswertung der Daten bestätigt, die neue Werte und Unsicherheiten für den Koeffizienten der Elektron-Asymmetry A und das Verhältnis von Axialvektor- zu Vektor-Kopplung λ liefert. Verglichen mit dem aktuellen Mittelwert der Particle Data Group (PDG) konnte die Unsicherheit auf den Koeffizienten A um den Faktor 5 verringert werden.

Contents

Chapter 1

Introduction

The parity P[1] was assumed to be one of the fundamental symmetries of the universe. After the proposal of a possible parity violation in 1956 by Lee and Yang [LY56], the famous Wu-experiment confirmed this prediction in the decay of ^{60}Co [Wu57]: our universe distinguishes between left- and right-handedness and the parity P is violated in processes of the Weak Interaction.

Some interesting questions arose: is parity P in general violated (Standard Model), or does this symmetry *disappear* due to a spontaneous symmetry breaking[2] at some energy (physics beyond). And if so, are there still remnants of the phase before this symmetry breaking, or parity symmetric properties accessible today (left-right symmetric models, SUSY[3]).

The present work concerns the decay of free neutrons ($\tau = 885.7(8)$ s, PDG [NG10]), a semi-leptonic process of the Weak Interaction,[4] which violates parity P. Neutrons are simple baryonic candidates for such processes. Hence, studying neutron decay has the advantage of an absence of a nuclear structure, compared with nuclear β-decay. In the decay of a free polarized neutron the spin of the neutron is correlated with the momenta of the decay products. A precise knowledge of the correlation coefficients allows detailed tests of the Standard Model and physics beyond.

The β-asymmetry correlation coefficient A for instance can be used to derive $\lambda = g_A/g_V$, the ratio of the axialvector- to the vector-coupling. This quantity is important in several parts of physics (e.g. cosmology) and can be used to

---

[1] Spatial mirroring at the origin.

[2] Without spontaneous symmetry breaking the W and Z bosons were predicted to be massless in the Standard Model.

[3] Super symmetric extension of the Standard Model. In SUSY each fermion has a bosonic super-partner and each boson has a fermionic super partner.

[4] A semi-leptonic process describes a Weak Interaction, where leptons and quarks are involved, in contrast to leptonic and non-leptonic processes.

determine V_{ud}, one element of the CKM[5] matrix. Since V_{ud} is close to unity, its contribution to the unitarity of the Standard Model is important. Therefore, it is substantially to know these quantities as precisely as possible.

Using the spectrometer PERKEO III, the β-asymmetry correlation coefficient A was determined during a nine-month beamtime at the research reactor of the Institute Laue Langevin in Grenoble. For the first time, a pulsed neutron beam was used in this kind of measurement, which considerably improved constraints on systematic effects. This is accompanied by an additional step forward in acquired statistics.

After a short introduction to the theoretical basics and motivations (chapter 2), the experimental setup (chapter 3) and the measurement (chapter 4) are described. The main part of this work focuses on the evaluation of the measured data and determination of corrections and uncertainties of the final result (chapter 5). Finally, the result is compared with previous asymmetry measurements and used to test the Standard Model and physics beyond, e.g. unitarity of the CKM matrix, left-right symmetric SM extensions and right-handed scalar and tensor models (chapter 6 and 7).

---

[5] Cabibbo Kobayashi Maskawa matrix. This matrix transforms the mass eigenstates of the down-type quarks to the weak eigenstates.

Chapter 2

Theoretical Background

"Le 1$^{\text{er}}$ Mars 1896, Henri Becquerel a découvert la radioactivité."[1] In this way Henri's son Jean began his recollections of the observations made by his father [Pai77]. This date can be regarded as the discovery day of radioactivity. Becquerel's observations have shaken the prevailing state of knowledge to its very foundations. A short time later, the radiative particles α, β and γ were identified.

Until today, the state of knowledge has been greatly increased. A few years after the electroweak unification [Gla61, Wei67, Sal68], three of the four known interactions were unified in the so-called Standard Model of particle physics. During the past 40 years, this theoretical model was very successful in its predictions (section 2.1). Only very few experimental results cannot be described with the Standard Model (e.g. neutrino-oscillation [Ahm04]). However, there remain still big open questions:

- Shortly after the Big Bang the universe was most probably symmetric in all its properties. Why is there an asymmetry between matter and antimatter today?
- What is the origin of P and CP violation?
- Why are there exactly three generations of quarks and leptons and what is the origin of flavor change?
- Why are there so many free parameters?
- And particularly, how does gravitation finally fit into the Standard Model?

Several extensions to the Standard Model are discussed since years: e.g. left-right symmetric theories, super-symmetric models, grand unified theories. These models were not confirmed to date, presumably since their respective energy scale is not accessible yet.

---

[1] "On the first of March 1896, Henri Becquerel discovered radioactivity."

At high energies collider experiments like the LHC at CERN try to answer the open questions. Experiments at low energies are not expected to discover new particles. On the other hand, they are very suitable for precise determination of particular model parameters. Thus for example, cold and ultra cold neutrons[2] are used to measure neutron decay observables with a precision of the order $\mathcal{O}(1 \cdot 10^{-3})$, e.g. [Ser05, Sch08]. Through detailed knowledge of these parameters, the Standard Model as well as the extensions can be tested.

The β-decay of a free neutron is a semi-leptonic process of the Weak Interaction:

$$\mathrm{n} \xrightarrow{\tau_\mathrm{n}} \mathrm{p} + \mathrm{e}^- + \overline{\nu}_\mathrm{e} \,, \tag{2.1}$$

where a neutron decays to proton p, electron e^- and electron anti-neutrino $\overline{\nu}_\mathrm{e}$. The continuous β-spectrum in weak three-body decays was first observed by Sir James Chadwick[3] in 1914 [Cha14], which Pauli explained in 1930 by proposing the neutrino as a new particle.[4] After the prediction of parity violation in 1956 by Lee and Yang [LY56], the famous Wu-experiment confirmed this in the decay of ^{60}Co [Wu57].

The β-asymmetry measurement, described in this thesis, covers some of the open questions of the Standard Model. For example, quark mixing and parity violation are addressed.

In this chapter some physical basics on Weak Interaction, the Standard Model and parity violation will shortly be described with the focus on physics that explains the semi-leptonic decay of free neutrons. Later the observables in this decay are derived and finally a brief introduction to possible tests of the Standard Model and physics beyond is given.

2.1 The Standard Model of Particle Physics

James Clerk Maxwell was the first who succeeded in the unification of two physical models: he unified electricity and magnetism [Max65]. Later this

---

[2] Neutrons with kinetic energies of some meV (cold) and some 100 neV or below (ultra cold).

[3] Chadwick later proposed the existence of the neutron in 1932 [Cha32].

[4] Niels Bohr even speculated that it might be necessary to abandon the idea of energy conservation, to describe the continuous beta spectrum [Boh32].

electromagnetic interaction was unified with the Weak Interaction to the QFD[5] or Electroweak Interaction [Gla61, Wei67, Sal68].

The Standard Model (SM) is an approach to unify QFD ($\mathrm{SU(2)_L \times U(1)}$) and QCD (Quantum ChromoDynamics, $\mathrm{SU(3)_C}$). The resulting gauge group is:

$$\mathrm{SU(3)_C \times SU(2)_L \times U(1)}\ . \tag{2.2}$$

The SM describes the elementary particles as well as the forces. It contains 12 spin-½ fermions (six quarks and six leptons), four spin-1 gauge bosons and a predicted spin-0 Higgs boson. The Standard Model is probably incomplete, since the gravitational interaction is not included [Wei92]. Nevertheless, it was very successful during the last 40 years. Seven of these 16 Standard Model particles (tau neutrino, charm, bottom, top, W, Z, gluon) were predicted by the model, before they were observed experimentally (the gluon was observed indirectly).

The predicted spin-0 Higgs boson, which is assumed to give mass to the W and Z bosons, is still not found. Actual measurements suggest a Higgs mass between 115 and 185 GeV [NG10].

Some properties of the Standard Model are:

- Energy, momentum, angular momentum, charge, color, baryon number and the three lepton numbers ($L_\mathrm{e}, L_\mu, L_\tau$) are conserved.
- The parities P, C and CP are only violated in QFD, the charged current is even maximally parity-violating, since it only couples to left-handed fermions and right-handed anti-fermions.
- Only the charged QFD current can change the flavor of quarks, therefore isospin is not conserved in QFD.
- The parity CPT is conserved due to the Lorentz invariance of the theory.

As mentioned above, there are still several open questions in this model. For example, the occurrence of parity violation is not explained but just implemented, as only left-handed fermions and right-handed anti-fermions participate in Weak Interaction, see eq. (2.6). This would imply that parity is not a fundamental symmetry. Some extensions to the Standard Model, which address this and other questions, are introduced in section 2.3.

---

[5] Quantum Flavor Dynamics.

2.2 Weak Interaction in the Standard Model

Shortly after Pauli postulated the neutrino, Fermi developed the first Lorentz invariant theory of the β-decay, based on a local coupling of four spin-½ fields [Fer34]. A more general Lagrange density is [Fie37]:

$$\mathcal{L} = \sum_{j=1}^{5} \left(g_j \, \overline{\mathrm{p}} \, \mathcal{M}_j \, \mathrm{n} \, \cdot \, \overline{\mathrm{e}} \, \mathcal{M}_j \, \nu \right) + \mathrm{h.c.}\,, \tag{2.3}$$

where g_j is an arbitrary coupling constant for the coupling of a $\overline{\mathrm{p}}\mathrm{n}$ field to a $\overline{\mathrm{e}}\nu$ field. The five possible couplings of $\mathcal{M}_j \otimes \mathcal{M}_j$ are:

$$\mathbb{1} \otimes \mathbb{1}\,,\; \gamma^{\mu} \otimes \gamma_{\mu}\,,\; \sigma^{\mu\nu} \otimes \sigma_{\mu\nu}\,,\; \gamma^{\mu}\gamma_5 \otimes \gamma_{\mu}\gamma_5\,,\; \gamma_5 \otimes \gamma_5\,, \tag{2.4}$$

which denote scalar, vector, tensor, axialvector and pseudoscalar couplings.

Parity Violation and V–A Theory

Gamow and Teller noted in 1936 [GT36] that linear combinations of the terms in eq. (2.3) also construct a scalar Lorentz invariant Lagrangian. In the non-relativistic limit, which is valid in the decay of free cold neutrons, they already observed that the pseudoscalar term vanishes. Additionally the following selection rules for the total lepton spin S were obeyed:

Coupling	Selection Rule
Scalar-Scalar SS Vector-Vector VV	$\}\; S = 0, S_z = 0$
Axialv.-Axialv. AA Tensor-Tensor TT	$\}\; S = 1, S_z = 0, \pm 1$

Hence, SS and VV transitions result in a spin singlet (Fermi transition), while AA and TT transitions yield a spin triplet of leptons (Gamow Teller transition). Theoretically the transitions SS and VV as well as AA and TT can interfere (Fierz term), but none of these interferences were found experimentally so far. Therefore only the vector and the axialvector currents are included in the so-called V–A theory:

$$\mathcal{L} = -\frac{G_{\mathrm{F}}}{\sqrt{2}} \, \overline{\mathrm{p}} \, \gamma^{\mu} \left(1 + \lambda \, \gamma_5\right) \mathrm{n} \, \cdot \, \overline{\mathrm{e}} \, \gamma_{\mu} \left(1 - \gamma_5\right) \nu + \mathrm{h.c.}\,, \tag{2.5}$$

introducing the Fermi constant G_F and $\lambda \equiv g_\mathrm{A}/g_\mathrm{V}$, denoting the ratio of axialvector to vector coupling constant. Equation (2.5) is essentially Fermi's original description extended by the axialvector contribution. The operator $(1-\gamma_5)$ projects the neutrino field to its left-handed part:

$$\frac{1}{2}\,(1-\gamma_5)\,\nu = \nu_\mathrm{L}\ , \tag{2.6}$$

which means that only left-handed neutrinos and right-handed antineutrinos participate in the Weak Interaction.[6]

After the discovery of the *strange* particles, quark mixing was proposed in Weak Interaction [Cab63], which is able to describe the flavor changing decay of the Kaon. The CKM matrix (Cabibbo Kobayashi Maskawa) transforms the mass eigenstates of the down-type quarks d, s, b to the corresponding weak eigenstates d', s', b' [KM73]:

$$\begin{pmatrix} d' \\ s' \\ b' \end{pmatrix} = \begin{pmatrix} V_\mathrm{ud} & V_\mathrm{us} & V_\mathrm{ub} \\ V_\mathrm{cd} & V_\mathrm{cs} & V_\mathrm{cb} \\ V_\mathrm{td} & V_\mathrm{ts} & V_\mathrm{tb} \end{pmatrix} \cdot \begin{pmatrix} d \\ s \\ b \end{pmatrix}\ . \tag{2.7}$$

Knowing the values of three CKM matrix elements experimentally, e.g. from the first row, allows to test the Standard Model unitarity:

$$1-\Delta = |V_\mathrm{ud}|^2 + |V_\mathrm{us}|^2 + |V_\mathrm{ub}|^2\ , \tag{2.8}$$

with Δ denoting the deviation from unitarity.

From quark mixing the final V–A Lagrangian density follows:

$$\mathcal{L} = -\frac{G_\mathrm{F}}{\sqrt{2}}\,|V_\mathrm{ud}|\;\bar{\mathrm{p}}\,\gamma^\mu\,(1+\lambda\,\gamma_5)\;\mathrm{n}\;\cdot\;\bar{\mathrm{e}}\,\gamma_\mu\,(1-\gamma_5)\;\nu + \mathrm{h.c.}\ . \tag{2.9}$$

Propagator

In 1935 Yukawa proposed that Weak Interaction is mediated by an exchange of a boson between the two involved currents. This boson should be massive (in contrast to the photon in QED) to explain the short range of this force [Yuk35]. The Electroweak unification [Gla61, Wei67, Sal68] followed Yukawa's proposal, introducing charged ($W^\pm$) and neutral (Z) gauge bosons. In the Lagrangian

---

[6] This is generalized for all fermions in the Standard Model.

these bosons are expressed with so-called propagator terms. The charged propagator W is [Nac86]:

$$W(q^2) = -\mathrm{i}\,\frac{\left(g_{\mu\nu} - \frac{q_\mu q_\nu}{m_\mathrm{W}^2}\right)}{q^2 - m_\mathrm{W}^2}\,, \tag{2.10}$$

where $g_{\mu\nu}$ denotes the metric tensor, q the momentum transfer and m_W the mass of the W boson. In neutron decay this propagator couples the hadronic to the leptonic current, see fig. 2.1. Since the mass of the W boson is much larger than the maximum momentum transfer in the decay of a free neutron (80 GeV vs. 1 MeV), the propagator can be assumed as constant. A constant in momentum space transforms to a $\delta(x)$-function in real space, which is equivalent to the current-current interaction, described by Fermi. Figure 2.1 shows the Feynman diagrams of the neutron decay with and without the propagator.

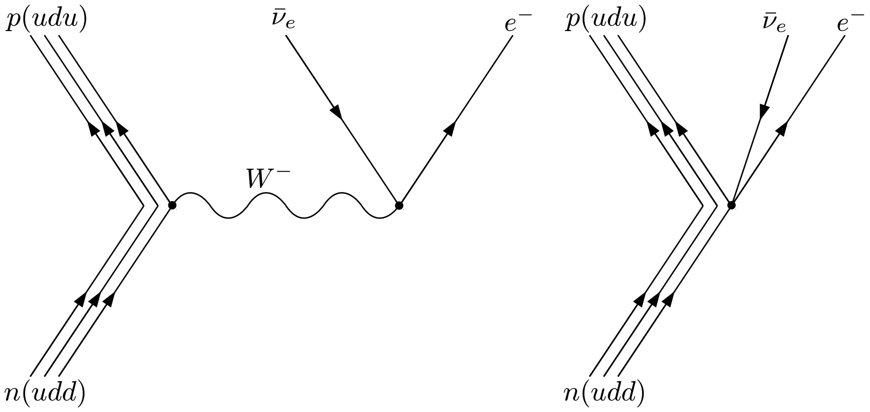

Figure 2.1: Left: Feynman diagram of the semi-leptonic neutron decay. **Right:** in the low energy limit, the propagator W is constant in momentum space, which is equivalent to a $\delta(x)$-function in real space. Therefore the Feynman diagram simplifies to a current-current interaction in a single vertex.

2.2.1 Observables in Neutron Decay

The transition matrix element of the neutron decay follows from eq. (2.9):[7]

$$|M_\mathrm{fi}|^2 \propto 1 + 3\,|\lambda|^2\,. \tag{2.11}$$

---

[7] Here the branching ratio between Fermi and Gamow Teller transitions is seen.

Using Fermi's Golden Rule, the neutron decay probability becomes:

$$\mathrm{d}\Gamma(E) = \frac{2\,\pi}{\hbar}\,|M_{\mathrm{fi}}|^2\,F(E)\,\mathrm{d}E\;, \tag{2.12}$$

introducing the phase space factor $F(E)$, which is the corrected theoretical phase space factor $F_{\mathrm{theo}}(E)$ (see derivation in appendix A.2):

$$F_{\mathrm{theo}}(E) = (E_0 - E)^2 \cdot (E + m_{\mathrm{e}}) \cdot \sqrt{(E + m_{\mathrm{e}})^2 - m_{\mathrm{e}}^2} \quad \text{and} \tag{2.13}$$

$$F(E) = F_{\mathrm{theo}}(E) \cdot (1 + \delta_{\mathrm{R}}(E)) \cdot (1 + R(E)) \cdot F_{\mathrm{C}}(E)\;, \tag{2.14}$$

where E denotes the kinetic energy[8] and m_{e} the mass of the electron. The corrections are: outer radiative correction $\delta_{\mathrm{R}}(E)$, recoil correction $R(E)$ and coulomb correction $F_{\mathrm{C}}(E)$. Assuming massless neutrinos, the released energy of the neutron decay reaction in eq. (2.1) is:

$$Q = m_{\mathrm{n}} - m_{\mathrm{p}} - m_{\mathrm{e}} = 782.3\,\mathrm{keV}\;, \tag{2.15}$$

where m_{n} and m_{p} denote the masses of neutron and proton. The endpoint energy E_0 of the continuous electron spectrum used in eq. (2.13) is Q with a minor correction due to the proton recoil:

$$E_0 = Q - \frac{(Q + m_{\mathrm{e}})^2 - m_{\mathrm{e}}^2}{2\,m_{\mathrm{p}}} = 781.6\,\mathrm{keV}\;. \tag{2.16}$$

The neutron lifetime can be derived from eq. (2.12) [MS06]:

$$\begin{aligned} \frac{1}{\tau} &= \int_0^{E_0} \frac{\mathrm{d}\Gamma}{\mathrm{d}E}\,\mathrm{d}E \cong \frac{0.47}{60\,\pi^3} \cdot \frac{g_{\mathrm{V}}^2 (E_0 + m_{\mathrm{e}})^5}{\hbar^7 c^6} \cdot (1 + 3\,|\lambda|^2) \\ &= |V_{\mathrm{ud}}|^2 \cdot \frac{1 + 3\,|\lambda|^2}{4908.7(1.9)\,\mathrm{s}}\;. \end{aligned} \tag{2.17}$$

---

[8] Throughout this document E and $E_{\mathrm{e}} = E + m_{\mathrm{e}}$ denote the kinetic and the total energy of an electron.

Angular Distribution and Correlation Coefficients

From eq. (2.9) the description of polarized neutrons decay is derived [JTW57]:

$$\begin{aligned} \mathrm{d}\Gamma = & \frac{G_\mathrm{F}^2\,|V_\mathrm{ud}|^2}{(2\,\pi)^5}\,F(E)\,|M_\mathrm{fi}|^2\,\mathrm{d}E\,\mathrm{d}\Omega_\mathrm{e}\,\mathrm{d}\Omega_\nu \\ & \times\left[1+a\,\frac{\mathbf{p}_\mathrm{e}\cdot\mathbf{p}_\nu}{E_\mathrm{e}\,E_\nu}+b\,\frac{m_\mathrm{e}}{E_\mathrm{e}}+\langle\sigma_\mathrm{n}\rangle\cdot\left(A\,\frac{\mathbf{p}_\mathrm{e}}{E_\mathrm{e}}+B\,\frac{\mathbf{p}_\nu}{E_\nu}+D\,\frac{\mathbf{p}_\mathrm{e}\times\mathbf{p}_\nu}{E_\mathrm{e}\,E_\nu}\right)\right]\,, \end{aligned} \tag{2.18}$$

where $\mathbf{p}_\mathrm{e}$, $\mathbf{p}_\nu$, E_e and E_ν are the momenta and total energies of electron and anti-neutrino respectively. The coefficient b denotes the Fierz term, which is non-zero only in left-handed scalar and tensor interactions beyond the Standard Model. The coefficients A, B and D correlate the expectation value of the neutron spin polarization $\langle\sigma_\mathrm{n}\rangle$ with the momenta of the decay products, see right plot in fig. 2.2, while a relates the electron- to the neutrino-momentum. The proton correlation C can be derived from the electron and the neutrino coefficients A and B.

Observable	**Dependence on λ**	**Violation of**	**PDG Value**
A	$-2\cdot\frac{\|\lambda\|^2+\Re(\lambda)}{1+3\,\|\lambda\|^2}$	Parity	$-0.1173(13)$
B	$2\cdot\frac{\|\lambda\|^2-\Re(\lambda)}{1+3\,\|\lambda\|^2}$	Parity	$0.9807(30)$
C	$x_\mathrm{c}\cdot\frac{4\,\Re(\lambda)}{1+3\,\|\lambda\|^2}$	Parity	$-0.2377(26)$
D	$2\cdot\frac{\Im(\lambda)}{1+3\,\|\lambda\|^2}$	Time reversal	$-4(6)\cdot10^{-4}$
a	$\frac{1-\|\lambda\|^2}{1+3\,\|\lambda\|^2}$		$-0.103(4)$
λ	1		$-1.2694(28)$
τ	$\frac{K}{\|V_\mathrm{ud}\|^2(1+3\,\|\lambda\|^2)}$		$885.7(8)\,\mathrm{s}$

Table 2.1: Observables in the decay of free polarized neutrons. The PDG values are from [NG10], including the kinetic factor $x_\mathrm{c}=0.27484$. The proton asymmetry is derived using $C=-x_\mathrm{c}(A+B)$.

Table 2.1 presents the main observables in the decay of free polarized neutrons, while the left plot in fig. 2.2 shows the dependence of the correlation coefficients a, A and B on λ.

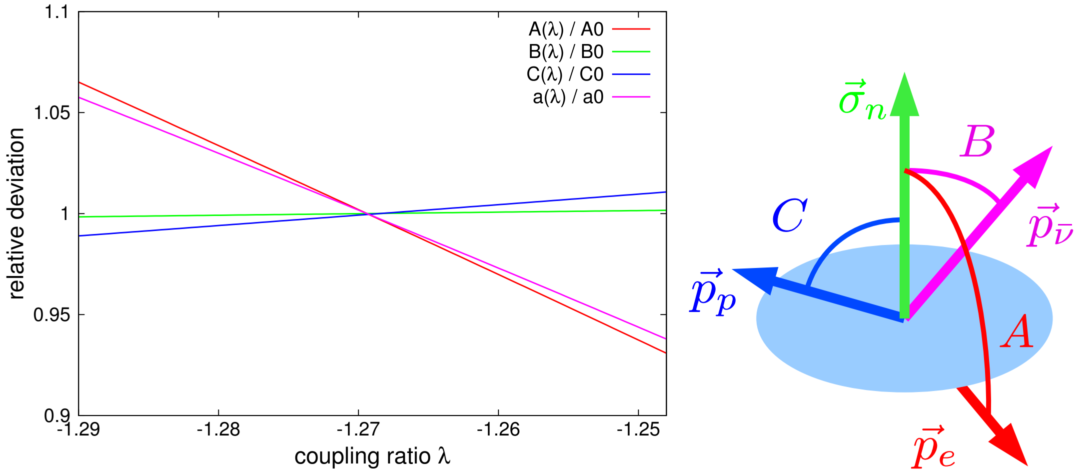

Figure 2.2: Left: normalized correlation coefficients A, B, C and a as function of λ. A and a show a higher sensitivity on λ compared with B and C. A measurement of these coefficients therefore is suitable for a precise determination of λ. **Right:** schematic of the correlations A, B and C, which relate the respective momenta to the spin of the neutron (green).

Since the corrections in eq. (2.14) are energy dependent, the β-asymmetry A in eq. (2.18) has to be corrected as well [Wil82][9]:

$$A'(E) = A\left[1 + A_{\mu M}\left(A_1\,\frac{E_0+m_\mathrm{e}}{m_\mathrm{e}} + A_2\,\frac{E+m_\mathrm{e}}{m_\mathrm{e}} + A_3\,\frac{m_\mathrm{e}}{E+m_\mathrm{e}}\right)\right] , \tag{2.19}$$

using:

$$A_{\mu M} = \frac{-\lambda + 2\,\kappa + 1}{-\lambda\cdot(1{+}\lambda)\cdot(1{+}3\,\lambda^2)}\cdot\frac{m_\mathrm{e}}{m_\mathrm{n}} \approx -1.7\cdot 10^{-3} \tag{2.20}$$

$$A_1 = \lambda^2 - \frac{2}{3}\,\lambda - \frac{1}{3} \approx 2.1 \tag{2.21}$$

$$A_2 = \lambda^3 - 3\,\lambda^2 + \frac{5}{3}\,\lambda + \frac{1}{3} \approx -8.7 \tag{2.22}$$

$$A_3 = 2\,\lambda^2\cdot(1+\lambda) \approx -0.87\,, \tag{2.23}$$

which yields an energy dependent correction on A of the order $1\cdot 10^{-2}$. The coefficients κ and therefore $A_{\mu M}$ describe the so-called weak magnetism. Additional external radiative corrections δA_R are approximately independent on

---

[9] In [Wil82] a different notation for λ is used: $\lambda = |g_\mathrm{A}/g_\mathrm{V}|$.

energy [GT92] and are included in the final systematic correction on A, see table 6.2:

$$A' = A \cdot (1 - \delta A_{\mathrm{R}}) \quad \text{with} \tag{2.24}$$

$$\delta A_{\mathrm{R}} = 9(5) \cdot 10^{-4} \,. \tag{2.25}$$

Experimental Asymmetry

From eq. (2.18) the experimental β-asymmetry $A_{\mathrm{exp}}(E)$ is derived. The spin dependent decay rate follows by integration over the solid angle Ω_{e}:

$$\begin{aligned} N^{\uparrow,\downarrow}(E) &= \int \frac{\mathrm{d}\Gamma}{\mathrm{d}\Omega_{\mathrm{e}}}\,\mathrm{d}\Omega_{\mathrm{e}} \\ &\propto F(E) \cdot (1 + 3\,|\lambda|^2) \cdot \int (1 \pm A\,\beta(E)\,\cos\theta)\,\mathrm{d}\Omega_{\mathrm{e}} \\ &\propto F(E) \cdot (1 + 3\,|\lambda|^2) \cdot (1 \pm \frac{1}{2} A\,\beta(E))\,, \end{aligned} \tag{2.26}$$

where $\beta(E) = |\mathbf{p}_{\mathrm{e}}|/E_{\mathrm{e}} = v(E)/c$ is the normalized velocity and θ the polar angle between neutron spin $\langle \sigma_{\mathrm{n}} \rangle$ and electron momentum $\mathbf{p}_{\mathrm{e}}$. The experimental asymmetry is defined as:

$$A_{\mathrm{exp}}(E) \equiv \frac{N^{\uparrow}(E) - N^{\downarrow}(E)}{N^{\uparrow}(E) + N^{\downarrow}(E)} = \frac{1}{2} A\,\beta(E)\,. \tag{2.27}$$

Therefore, by fitting the function $\beta(E)$ to the experimentally derived asymmetry spectrum $A_{\mathrm{exp}}(E)$, the correlation coefficient A is determined.

2.3 Physics Beyond the Standard Model

The Standard Model describes the strong, weak and electromagnetic interactions. The corresponding gauge group $\mathrm{SU(3)_C} \times \mathrm{SU(2)_L} \times \mathrm{U(1)}$ is found to be a fundamental symmetry group of nature with the three coupling constants:

$$\begin{array}{lcl} \mathrm{SU(3)_C} & \rightarrow & g_3 \equiv \alpha_S \\ \mathrm{SU(2)_L \times U(1)} \left\{ \begin{array}{c} \\ \\ \end{array} \right. & \begin{array}{c} \rightarrow \\ \rightarrow \end{array} & \begin{array}{l} g_2 \equiv g \;\; = e_0 / \sin\theta_{\mathrm{W}} \\ g_1 \equiv g' = e_0 / \cos\theta_{\mathrm{W}}\,, \end{array} \end{array}$$

where θ_W denotes the Weinberg angle and e_0 the elementary charge. These coupling constants are different at the energy scales accessible today. This rises the question, whether the SM gauge group is really a fundamental symmetry, or it is part of a higher symmetry $\mathcal{G}$:

$$\mathcal{G} \supset \mathrm{SU}(3)_\mathrm{C} \times \mathrm{SU}(2)_\mathrm{L} \times \mathrm{U}(1) \,. \tag{2.28}$$

GUT SU(5)

The smallest irreducible group satisfying eq. (2.28) is SU(5) [GG74]. Some properties of this Grand Unifying Theory (GUT) are:

- The three coupling constants and forces are unified at energies of 10^{15} GeV
- The ratio between quark an lepton masses can be derived
- The equality of electron and proton charge is explained
- The Weinberg angle θ_W is predicted

To obtain three different forces, it is assumed that below the energy scale of 10^{15} GeV the symmetry is spontaneously broken to the gauge symmetry of the Standard Model. The remaining drawbacks of this SU(5) GUT are that there are still about 20 free parameters and neither the reason for the existence of exactly three quark and lepton generations nor the origin of parity violation can be explained. Gravity is still missing and the prediction for the proton lifetime is two orders of magnitude below the experimental limit, given by the particle data group PDG.

GUT SO(10)

Another possible group satisfying eq. (2.28), which includes SU(5), is SO(10). In this representation neutrinos are massive particles and the proton lifetime is longer. Between the SO(10) mass scale and the Standard Model mass scale several intermediate symmetry breakings appear, e.g. left-right symmetry breaking, see below.

Supersymmetry SUSY

In Supersymmetry fermions and bosons are combined with their super-partners in so-called super-multiplets: a fermion with a sfermion and a boson with a bosino [VA72]. These super-partners obey the opposite spin-statistics: a sfermion is bosonic and a bosino is fermionic. Therefore, the total number of particles is doubled. In exact SUSY the particles would have the same mass as their super-partners. Since experimentally no super-partner was found so far, SUSY must be broken.

The Minimal Supersymmetric Standard Model (MSSM) is the minimal extension to the Standard Model that realizes supersymmetry. It was proposed in 1981 to stabilize the weak scale and solve the hierarchy problem [DG81].

In the low energy range several SUSY models propose limits on e.g. neutron-EDM,[10] which will be experimentally accessible within the next decade. Besides this they propose supersymmetric contributions to weak decay correlation coefficients, like in neutron decay [ERM05, PRMT07, RMS08].

2.3.1 Left-Right Symmetric Models

The symmetry group of the simplest left-right symmetric extension to the Standard Model is:

$$\mathrm{SU}(3)_\mathrm{C} \times \mathrm{SU}(2)_\mathrm{R} \times \mathrm{SU}(2)_\mathrm{L} \times \mathrm{U}(1)\ . \tag{2.29}$$

It is one of the intermediate symmetries in SO(10) GUT. The left-right symmetry is spontaneously broken at the energy scale of the mass of the right-handed charged boson W_R, which is at least one order of magnitude above the mass of the left-handed boson W_L [CA11]. At energies above this scale there is no difference between left and right. After symmetry breaking parity violation appears, since the right-handed current is suppressed due to the high mass of the W_R boson. Similarly to quark mixing, the weak eigenstates of the charged bosons $W_\mathrm{L,R}$ can be expressed as an admixture of the mass eigenstates $W_{1,2}$:

$$\begin{pmatrix} W_\mathrm{L} \\ W_\mathrm{R} \end{pmatrix} = \begin{pmatrix} \cos\zeta & -\sin\zeta \\ \mathrm{e}^{\mathrm{i}\phi}\sin\zeta & \mathrm{e}^{\mathrm{i}\phi}\cos\zeta \end{pmatrix} \cdot \begin{pmatrix} W_1 \\ W_2 \end{pmatrix}\ , \tag{2.30}$$

where ϕ denotes the CP-violation phase and ζ the mixing angle. In the manifest left-right symmetric model the formalism to describe both left- and right-handed contributions is identical [Bég77]. Therefore the additionally introduced parameters are mass ratio δ and coupling ratio λ':

$$\delta = \left(\frac{m_{W_1}}{m_{W_2}}\right)^2 \quad \text{and} \quad \lambda' = \frac{g'_\mathrm{A}}{g'_\mathrm{V}}\ . \tag{2.31}$$

---

[10] EDM: electric dipole moment

The parameter λ' is the same for left- and right-handed currents. Before the impact on the correlation coefficients is described, two definitions are made:

$$r_{\mathrm{F}} = \frac{\delta \cdot (1+\tan\xi) - \tan\xi \cdot (1-\tan\xi)}{\delta \tan\xi \cdot (1+\tan\xi) + (1-\tan\xi)} \approx \frac{\delta - \tan\xi}{1-\tan\xi} \approx \delta - \xi\,, \tag{2.32}$$

$$r_{\mathrm{GT}} = \frac{\delta \cdot (1-\tan\xi) + tan\xi \cdot (1+\tan\xi)}{(1+\tan\xi) - \delta \tan\xi \cdot (1-\tan\xi)} \approx \frac{\delta + \tan\xi}{1+\tan\xi} \approx \delta + \xi\,. \tag{2.33}$$

These two functions denote Fermi- and the Gamov-Teller-contributions of the right-handed interaction. The neutron decay observables A, B and τ become [Döh90]:

$$A = -2 \cdot \frac{\lambda'\,(\lambda'+1) - r_{\mathrm{GT}}\,\lambda'\,(r_{\mathrm{GT}}\,\lambda' + r_{\mathrm{F}})}{(1+r_{\mathrm{F}}^2) + 3\,\lambda'^2\,(1+r_{\mathrm{GT}}^2)}\,, \tag{2.34}$$

$$B = 2 \cdot \frac{\lambda'\,(\lambda'-1) - r_{\mathrm{GT}}\,\lambda'\,(r_{\mathrm{GT}}\,\lambda' - r_{\mathrm{F}})}{(1+r_{\mathrm{F}}^2) + 3\,\lambda'^2\,(1+r_{\mathrm{GT}}^2)}\,, \tag{2.35}$$

$$\tau = \frac{ft^{0^+\to 0^+}}{f^{\mathrm{R}}\,\ln 2} \cdot \frac{2\cdot(1+r_{\mathrm{F}}^2)}{(1+r_{\mathrm{F}}^2) + 3\,\lambda'^2\,(1+r_{\mathrm{GT}}^2)}\,. \tag{2.36}$$

The constant $f^{\mathrm{R}} = 1.71385(34)$ includes the integrated phase space $F(E)$ and the corrections in eq. (2.14) [Kon10], while $ft^{0^+\to 0^+} = 3071.81(83)$ s denotes the ft-value of the super-allowed nuclear beta decay [HT09].

The Standard Model is included in this model in case of mixing angle $\xi = 0$, mass ratio $\delta = 0$ and $\lambda' = \lambda$.[11] Using experimentally determined values for A, B and τ including their uncertainties, limits on λ', ξ and δ can be derived. In section 6.3.2 this analysis is performed using the results of this measurement.

2.3.2 Scalar and Tensor Interactions

The V–A theory omits scalar S and tensor T interactions, described in eq. (2.3). Two possible contributions of these interactions can be tested using the observables of neutron decay measurements.

---

[11] λ' is not necessarily the same as the left-handed λ.

2.3.2.1 Left-Handed Scalar and Tensor Contributions, Fierz Term

In this model non-vanishing Fierz interference terms b and b_ν appear. In [Kon10] the current limits for left-handed scalar and tensor contributions from neutron decay measurements (used parameters: A, B, C, a and τ) are presented together with limits from nuclear β-decay. At present the latter limits are more than one order of magnitude smaller compared to those derived from neutron decay [SBNC06]. Therefore, tests on left-handed scalar and tensor contributions are omitted in this work.

The Fierz interference term b in eq. (2.18) modifies the number of unpolarized neutron decay events from $N(E)$ to $N'(E)=N(E)\cdot(1+b\,m_\mathrm{e}/(E+m_\mathrm{e}))$. From this unpolarized spectrum it is difficult to obtain reliable limits on b, due to differential non-linearities of the detector response function, which are much larger than the integral non-linearities, see fig. 5.1 and 5.2a.

The measured asymmetry spectrum $A_\mathrm{exp}(E)$, eq. (2.27), is also sensitive to a non-zero term b. The derivation of b from this spectrum has the advantage that $A_\mathrm{exp}(E)$ is a relative measurement, which is not very sensitive to differential non-linearities. In the numerator $N^\uparrow(E)-N^\downarrow(E)$, the Fierz term cancels, but not in the denominator. The experimental asymmetry becomes:

$$A'_\mathrm{exp}(E) = A_\mathrm{exp}(E)\cdot\frac{1}{1+b\,\frac{m_\mathrm{e}}{E+m_\mathrm{e}}}\,. \tag{2.37}$$

Prospectively it is planned to derive the Fierz term b using the results of this measurement.

2.3.2.2 Right-Handed Scalar and Tensor Contributions

In the right-handed scalar and tensor model the Fierz interference terms b and b_ν are zero [EM91, SBNC06]. The remaining free parameters are the coupling constants g_V, g_A, g_S and g_T,[12] each in a left- and right-handed presentation, distinguished with a $'$ for right-handed couplings. As in the manifest left-right

---

[12] VAST denotes vector, axialvector, scalar and tensor.

symmetric model, some assumptions are made to reduce the number of free parameters:

$$\frac{g'_V}{g_V} = 1\,, \quad \frac{g'_A}{g_A} = 1\,, \quad \frac{g'_S}{g_V} = -\frac{g_S}{g_V}\,, \quad \frac{g'_T}{g_A} = -\frac{g_T}{g_A}\,. \tag{2.38}$$

The observables in neutron decay become [GJL95, Sch07a, Abe09]

$$A = -2\cdot\frac{\lambda^2 + \lambda + \lambda\, x\, y + \lambda^2 y^2}{1 + 3\lambda^2 + x^2 + 3\lambda^2 y^2}\,, \tag{2.39}$$

$$B = 2\cdot\frac{\lambda^2 - \lambda + \lambda\, x\, y - \lambda^2 y^2}{1 + 3\lambda^2 + x^2 + 3\lambda^2 y^2}\,, \tag{2.40}$$

$$C = 4\, x_C\cdot\frac{\lambda + \lambda^2 y^2}{1 + 3\lambda^2 + x^2 + 3\lambda^2 y^2}\,, \tag{2.41}$$

$$a = \frac{1 - \lambda^2 - x^2 + \lambda^2 y^2}{1 + 3\lambda^2 + x^2 + 3\lambda^2 y^2}\,, \tag{2.42}$$

$$\tau = \frac{f t^{0^+\to 0^+}}{f^R\cdot \ln 2}\cdot\frac{2\cdot(1 + x^2)}{1 + 3\lambda^2 + x^2 + 3\lambda^2 y^2}\,, \tag{2.43}$$

where the introduced parameters λ, x and y are:

$$\lambda = \frac{g_A}{g_V}\,, \quad x = \frac{g_S}{g_V} \quad \text{and} \quad y = \frac{g_T}{g_A}\,. \tag{2.44}$$

The Standard Model is included in this model in case of scalar contribution $x=0$ and tensor contribution $y=0$. Using experimentally determined values for A, B, C, a and τ including their uncertainties, limits on x, y and λ can be derived. This is done in section 6.3.3, applying the results of this measurement.

Chapter 3

Spectrometer PERKEO III and Experimental Setup

The spectrometer PERKEO III, developed in 2006 [Mär06, MM09], is the successor of the spectrometer PERKEO II [Sch08, Sch07b, Mun06, Rei99, Abe97] and foreseen to continue the precision measurements in neutron decay of the *ANP group* at the *Physikalisches Institut* in Heidelberg. The first measurement with PERKEO III was done from October 2006 to April 2007 with the intention to measure – for the first time – the weak magnetism coefficient κ in β-decay.

To perform the β-asymmetry measurement in 2008/09, PERKEO III was installed at the ILL (Institut Laue Langevin) in Grenoble. The beam facility PF1B and the neutron guide H113 were well known from previous asymmetry measurements.

In this chapter the spectrometer PERKEO III and the experimental setup is described. For the first time the β-asymmetry is measured using a pulsed neutron beam, see section 3.1.2 and 3.4. Later the data acquisition and storage system is explained, as well as the development of new ADC[1] modules.

3.1 Neutron Source at the ILL

The ILL is an international neutron research center. The institute was founded in 1971 and still operates the most intense neutron sources in the world, serving beams of neutrons to a suite of about 40 instruments. The thermal power of the reactor is about 54 MW (compare to e.g. nuclear power plant *Gundremmingen B+C, Germany* with $P = 2.5\,\text{GW}$).[2]

---

[1] Analog to Digital Converter

[2] From: http://www.world-nuclear.org/info/inf43.html

The hot neutron flux of the reactor core at nominal power is:

$$\Phi = 1.5 \cdot 10^{15}\,\mathrm{s}^{-1}\mathrm{cm}^{-2}\ . \tag{3.1}$$

The neutrons are moderated to energies of less than 0.1 µeV to about 10 eV (from *ultra cold* to *intermediate*) and distributed to the various experiments by use of neutron guides. This broad energy range together with other properties (e.g. absence of electrical charge, $m_\mathrm{n} \cong m_\mathrm{p}$, limited lifetime) render neutrons very interesting for a variety of experiments from different areas in physics (e.g. material science, biophysics, nuclear- and particle-physics, ...).

3.1.1 Neutron Guide H113

The neutron guide H113 was designed and assembled in the year 2000 [Häs02]. It is the first realization of a so-called ballistic super-mirror neutron guide, that transports the *cold* neutrons under a small glancing angle to the beam facility PF1B. The capture flux density at the exit of H113 is $\Phi_\mathrm{c} = 2 \cdot 10^{10}\,\mathrm{s}^{-1}\mathrm{cm}^{-2}$ [Abe06]. It can be derived from the flux density

$$\Phi = \int_v \Phi(v)\,\mathrm{d}v\ , \tag{3.2}$$

weighted with the reciprocal of the velocity v:

$$\Phi_\mathrm{c} = \int_v \Phi(v)\,\frac{v_0}{v}\,\mathrm{d}v\ , \tag{3.3}$$

where $v_0 = 2200\,\mathrm{m/s}$ is the velocity of thermal neutrons. The capture flux is significant, since the efficiency of most neutron detectors is proportional to the dwell-time of a particle, which is reciprocally proportional to the velocity. For cold neutrons ($v < v_0$) the capture flux is higher than the flux.

A few characteristic data on the neutron guide H113:[3]

- Ballistic neutron guide with super-mirror type:[4] $m = 2$
- Length: 76 m, radius: 4000 m
- Energy of neutrons at temperature of liquid deuterium: $T \cong 25\,\mathrm{K}$ → *cold* neutrons, $E \approx 2\,\mathrm{meV}$, $\lambda_\mathrm{mean} = 4 \ldots 4.5\,\mathrm{Å}$

---

[3] From: http://www.ill.eu/.../pf1b/characteristics/

[4] Relative neutron reflection angle of the used coating material, normalized to the angle of natural Ni with $m = 1$.

- Non-polarized beam cross-section: $6 \times 20\,\mathrm{cm}^2$
- Polarized beam cross-section: $6 \times 8\,\mathrm{cm}^2$
- Non-polarized capture flux: $2 \cdot 10^{10}\,\mathrm{s}^{-1}\mathrm{cm}^{-2}$
- Polarized capture flux: $3 \cdot 10^{9}\,\mathrm{s}^{-1}\mathrm{cm}^{-2}$
- Beam divergence: $\theta \cong 7\,\mathrm{mrad}$

Super-mirrors consist of multiple (typically 100) Ni/Ti layers of varying thickness in contrast to conventional one-layer nickel coatings. The advantage of super-mirror guides is that the critical angle of total reflection is about twice that of conventional nickel guides, so that the transmission is increased by up to a factor of four. The disadvantage is that neutron reflection losses are higher for angles above $m = 1$. The reflectivity of a single layer nickel coating is about 98–99 %. In H113, this value decreases linearly to $\approx 90\,\%$ at $m \cong 2$ [Häs02].

3.1.2 Neutron Velocity Selector

The velocity distribution of the moderated cold neutrons from the guide H113 is almost[5] Maxwellian. However, one of the requirements of using a pulsed beam is having a narrow velocity distribution, see section 3.4.1. This selection is realized by using a neutron velocity selector (by Astrium GmbH, formerly Dornier, company of the Daimler Group).

The technical principle of a velocity selector is based on that of a turbine. Helical slits in the surface of a rotating cylinder transmit only neutrons with a corresponding velocity. Therefore the blades of the turbine are coated with a neutron absorber – in this case $^{10}\mathrm{B}$, see fig. 3.1a and table 3.1 on page 38.

Hence, a fraction of about 80 % of the total flux is absorbed and a large intensity of γ-radiation is created. The rotational speed can be controlled in the range from 3000 to 28300 rpm, which corresponds to neutron wavelengths of 0.45–4.3 nm.

The selector was installed between the exit of the neutron guide H113 and the polarizer (section 3.1.3). To get the maximum transmission of neutrons at the chosen neutron wavelength of $\lambda = 5\,\text{Å}$, the rotational speed was set to 25470 rpm during the neutron decay measurements.

---

[5] Due to wavelength dependent transmission and a not ideal thermalization, the Maxwellian distribution is modified.

Some characteristic properties of the selector [Dai]:

- Rotor diameter: 290 mm, rotor length: 250 mm
- Number of blades: 72
- Material of blades: carbon fiber in epoxy, loaded with 35 g/m^2 of ^{10}B
- Speed range: 3000–28300 rpm, speed constancy: 0.2 %
- Neutron wavelength range: 0.45–4.3 nm
- Width of transmitted neutron spectrum: $\Delta\lambda/\lambda \cong 10\,\%$

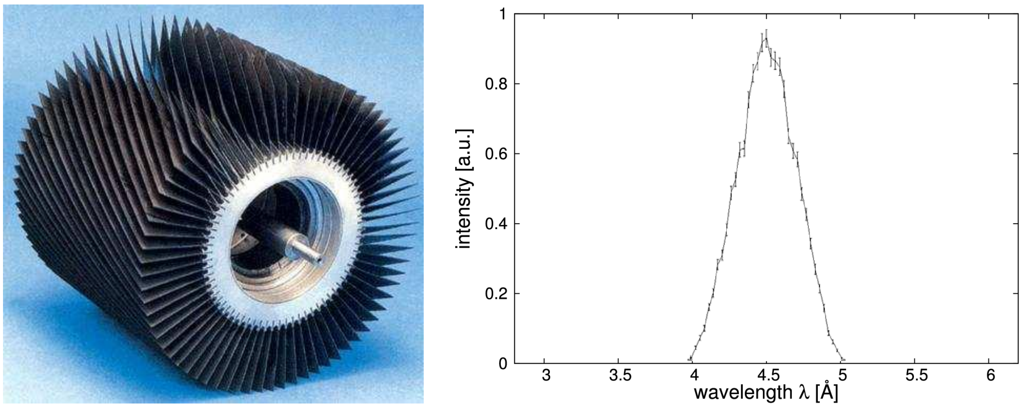

(a) Picture of the boron coated neutron-absorbing blades of the turbine.

(b) Wavelength transmission function. The FWHM is about 10 % of the nominal wavelength.

Figure 3.1: Velocity selector from Astrium / Dornier. Plots from [Dai].

3.1.3 Polarization of the Neutron Beam

The β-asymmetry coefficient A correlates the spin of the neutron $\langle \sigma_n \rangle$ with the momentum of the electron $\mathbf{p}_e$, see eq. (2.18). Hence, the neutron beam has to be spin-polarized.

The polarization $\mathcal{P}$ is a measure for the purity of a particle beam with respect to the chosen spin state:

$$\mathcal{P} = \frac{X^{\uparrow} - X^{\downarrow}}{X^{\uparrow} + X^{\downarrow}} \quad \Rightarrow \quad \frac{X^{\downarrow}}{X^{\uparrow}} = \frac{1-\mathcal{P}}{1+\mathcal{P}}\,, \quad \mathcal{P} \in [0,1]\,, \tag{3.4}$$

with $X^{\uparrow}$ as number of neutrons in the chosen spin state and $X^{\downarrow}$ as the impurity contribution. Thus, the resulting electron spectra from neutron decay $N^{\uparrow,\downarrow}$ can be described as:

$$N^{\uparrow} = \frac{1}{2} n^{\uparrow}(1+\mathcal{P}) + \frac{1}{2} n^{\downarrow}(1-\mathcal{P}) \quad \text{and} \tag{3.5}$$

$$N^{\downarrow} = \frac{1}{2} n^{\uparrow}(1-\mathcal{P}) + \frac{1}{2} n^{\downarrow}(1+\mathcal{P}) \,, \tag{3.6}$$

where $n^{\uparrow,\downarrow}$ denote the fully polarized spectra. The experimental asymmetry is defined as:

$$A_{\text{exp}} = \frac{N^{\uparrow} - N^{\downarrow}}{N^{\uparrow} + N^{\downarrow}} = \frac{n^{\uparrow} - n^{\downarrow}}{n^{\uparrow} + n^{\downarrow}} \cdot \mathcal{P} \,. \tag{3.7}$$

The technical realization of a polarizer is done by using a stack of super-mirrors with layers of magnetic materials. These are – in contrast to a neutron guide – inside a constant magnetic field. Depending on the direction of the magnetic moment of the neutrons (spin) this additional magnetic potential is either attractive or repulsive. By choosing an appropriate coating material and suitable magnetic field strength, the super-mirrors transmit only neutrons with one of the two possible spin-directions (more details in [SS89]). The other neutrons are absorbed by e.g. Gadolinium Gd (see table 3.1), which produces a high intensity of γ-radiation. Therefore the polarizer as well as the velocity selector are placed in the *casemate*, which is sufficiently shielded by at least 20 cm of lead and 50 cm of concrete.

The fraction of transmitted neutrons with $\mathcal{P} \approx 98.5\,\%$ is about 25 % [Sch04]. With a second polarizer in *crossed geometry* [Kre05b] the polarization could be increased up to $\mathcal{P} \cong 99.7\,\%$ with the disadvantage of losing another factor of two in transmission and therefore statistics. The current measurement was performed with one polarizer, to achieve the aimed statistics. The value of the polarization $\mathcal{P}$ is one part of the three blinded quantities in the data analysis, see section 6.1.

A polarization measurement over the beam area was done several times during the beamtime to derive the value of $\mathcal{P}$ and to detect a possible time dependent degradation, see section 4.3. Figure 3.2 shows the wavelength-dependence of the polarization, measured in 1999 with a different polarizer.

An alternative method of neutron polarization using ^{3}He-cells is described in appendix B.1.

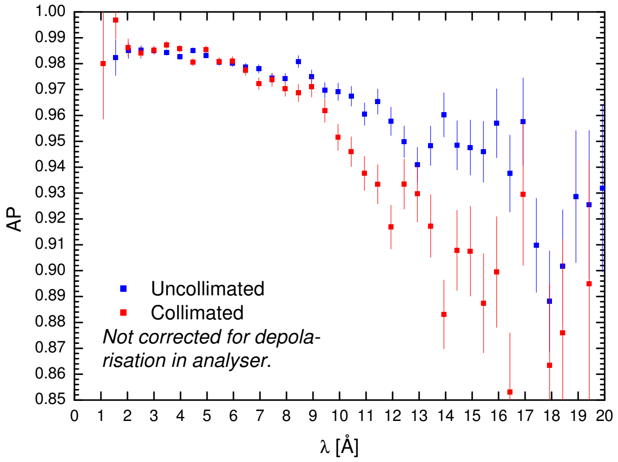

Figure 3.2: Wavelength dependent polarization of a super-mirror polarizer at PF1B [SPP02]. Note: the plot presents $\mathcal{A} \cdot \mathcal{P}$, the product of polarization and analyzer-strength, with $\mathcal{P} \approx \mathcal{A}$.

3.2 Beamline

The beamline guides the neutrons from the polarizer to the chopper and the spectrometer. It is composed of:

- Radio frequency spinflipper
- Collimation system
- Magnetic holding field

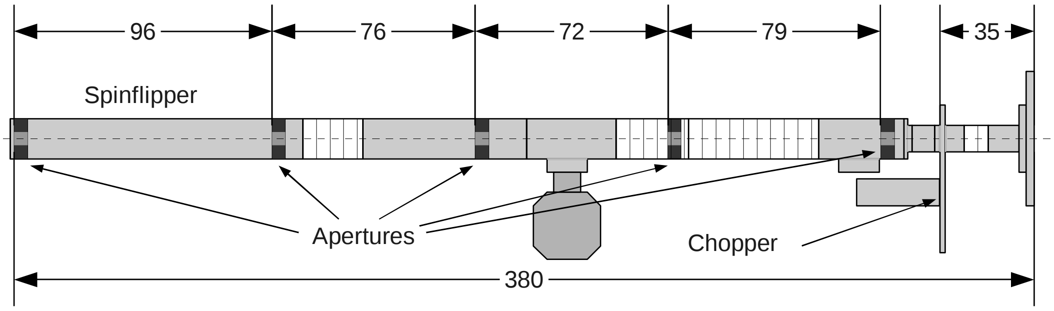

Figure 3.3: Schematic of the beamline with spinflipper, five apertures of the collimation system and chopper. The total length is about 3.8 m. All given measures are in cm.

Figure 3.3 shows a schematic of the assembled beamline, which the neutrons enter through an aluminum window of $d = 200\ \mu\text{m}$. The individual components are described in this section.

3.2.1 Spinflipper and Magnetic Holding Field System

The used AFP (adiabatic fast passage) spinflipper is a system of a static magnetic field $\mathbf{B}_0(z)$ parallel to the neutron spin and an AC field $\mathbf{B}_{\mathrm{RF}}$ perpendicular to $\mathbf{B}_0(z)$. The spin of a particle in a magnetic field $\mathbf{B}$ is precessing with the Larmor frequency:

$$\omega_1 = \gamma\,\mathbf{B} \overset{\text{neutron}}{=} 1.83 \cdot 10^8\,\mathrm{s}^{-1} \cdot \mathbf{B}\,[\mathrm{T}]\,, \tag{3.8}$$

with γ denoting the gyromagnetic ratio. The static field $\mathbf{B}_0(z)$ has a longitudinal gradient, and the RF field oscillates with ω_{RF}, which is chosen to be the same as $\omega_1(\mathbf{B}_0(z))$ at the defined spin-flip point $z = z_0$. When these quantities are transformed to the rotating frame of the neutron spin, the effective magnetic field becomes:

$$\mathbf{B}_0' = \mathbf{B}_0 - \frac{\omega_1}{\gamma}\,, \tag{3.9}$$

which is equal to zero at the spin-flip point $z = z_0$. The effective field

$$\mathbf{B}_{\mathrm{eff}} = \mathbf{B}_0' + \mathbf{B}_{\mathrm{RF}} \tag{3.10}$$

rotates continuously, while the neutrons pass the spinflipper and the spin is inverted at the exit of the spinflipper, details in [Baz93]. Figure 3.4 shows the several magnetic fields acting on the spin (different notations were used: $H \Leftrightarrow B$, $H_1 \Leftrightarrow B_{\mathrm{RF}}, \ldots$).

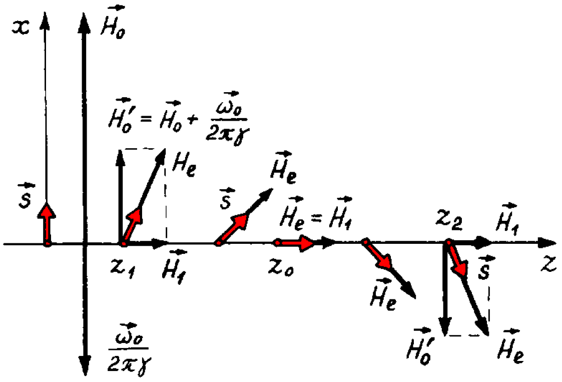

Figure 3.4: Principle of the RF spinflipper in the rotating frame of the neutron: a constant field H_0 and a rotating field H_1 act on the spin of the neutron (red arrow). At $z = z_0$ the z-component of the spin is 0 and at $z = 2\,z_0$ the spin is completely inverted (figure from [Baz93]).

Since the spinflipper is either switched on or off, the spin flip efficiency $\mathcal{F}$ does only influence one of the two spin-directions. Similar to eq. (3.6) and using the same definitions for $n^{\uparrow,\downarrow}$, $N^{\uparrow,\downarrow}$, the experimental asymmetry becomes (using polarization $\mathcal{P}=1$):

$$N^{\uparrow} = n^{\uparrow} \,, \tag{3.11}$$

$$N^{\downarrow} = \frac{1}{2} n^{\uparrow}(1-\mathcal{F}) + \frac{1}{2} n^{\downarrow}(1+\mathcal{F}) \quad \text{with } \mathcal{F} \lesssim 1 \quad \Rightarrow \tag{3.12}$$

$$A_{\text{exp}} = \frac{n^{\uparrow} - n^{\downarrow}}{n^{\uparrow} + n^{\downarrow}} \cdot \mathcal{F} \,. \tag{3.13}$$

The value of the spin flip efficiency during the 2009 beamtime, which was measured together with the polarization $\mathcal{P}$, is close to unity [Sol11]:

$$\mathcal{F} = 1.000^{(+0)}_{(-1)} \,. \tag{3.14}$$

Throughout their flight towards the spectrometer the spin of the neutrons is guided. When they leave the spinflipper (still transversely polarized) an additional magnetic holding field is applied to maintain the existing polarization $\mathcal{P}$. Close to the spectrometer the spin is turned from transversal to longitudinal direction (flight direction), since the magnetic field of PERKEO III is oriented longitudinally, see fig. 3.5.

3.2.2 Collimation System

The neutron guide H113 has an intrinsic beam divergence of $\theta \cong 7\,\text{mrad}$, see section 3.1.1 and [Abe06]. The collimation system is used to guide and shape the beam. This was realized by placing five apertures with an average distance of 80 cm inside the beamline, see fig. 3.3. The base material of these apertures is lead, while the complete surface is covered with ^{6}LiF tiles or ^{6}Li rubber[6]. The orifice of the apertures is $6\times6\,\text{cm}^2$. The spatial characterization of the beam was measured at several longitudinal positions, e.g. behind each of the apertures and at the center of the spectrometer, see section 4.2.

---

[6] The isotope ^{6}Li is a good neutron absorber. In table 3.1 several neutron absorbers are compared.

3.3 Spectrometer PERKEO III

The schematic in fig. 3.5 shows the spectrometer PERKEO III, the collimation system and the chopper. The magnetic field (marked in red) guides the charged particles from neutron decay out of the decay volume (center part) and projects them to the detection system located in the two detector vessels, symmetric with respect to the plane through the center of the decay volume.

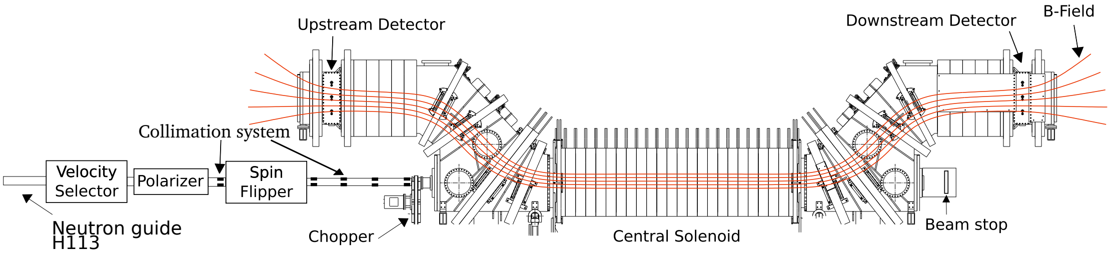

Figure 3.5: Complete PERKEO III setup including beamline, collimation system, chopper and spectrometer with its three parts: decay volume in the center and two symmetric detector vessels. The applied magnetic field, emphasized in red, guides the charged particles away from the neutron beam.

A few characteristics of the spectrometer:

- Total length: 8 m, total weight: 8 t
- Decay volume: length: 2.7 m, inner diameter: 50 cm
- Number of solenoids: 22 at the decay volume, 2×14 at the detector vessels
- Magnetic field strength: in decay volume $B_{\mathrm{max}} \cong 150\,\mathrm{mT}$, at detectors $B_{\mathrm{det}} \cong 80\,\mathrm{mT}$
- $2\times 2\pi$ detection system for decay products
- Symmetric magnetic field and electron detection design

The main components of PERKEO III (e.g. magnetic field system, electron detection system, ...) are described in this section.

3.3.1 Magnetic Field System and Magnetic Mirror Effect

Due to the Lorentz force a charged particle gyrates perpendicular to an applied magnetic field B. The gyration radius is a function of the field strength and the perpendicular momentum $p_\perp$:

$$r = \frac{p_\perp}{q\,B} \cong \frac{p_\perp[\mathrm{MeV/c}]}{3 \cdot B[\mathrm{T}]}\,\mathrm{cm} \quad \text{with} \tag{3.15}$$

$$p^2 = p_\perp^2 + p_\parallel^2 = \text{const}\,. \tag{3.16}$$

In PERKEO III the gyration radii are:

$$r_{\text{decay}} \leq 2.6\,\mathrm{cm} \quad \text{in the decay volume and} \tag{3.17}$$

$$r_{\text{det}} \leq 3.6\,\mathrm{cm} \quad \text{using also eq. (3.25)}\,. \tag{3.18}$$

The charged particle beams from neutron decay (e.g. electrons) are guided by the magnetic field and therefore can be separated from the neutron beam. In this way it is possible to project them to a detection system outside the neutron beam.

Because of magnetic field variations in the decay volume of PERKEO III, decay particles can be reflected to the wrong detector due to the magnetic mirror effect. Before the requirements on the design of the magnetic field are defined, some basics will be described first.

Concept of Adiabatic Invariance – Magnetic Mirror Effect

The term *Adiabatic Invariance* can be described by introducing the *action integrals* J_i of a mechanical system:

$$J_i = \oint p_i\,\mathrm{d}q_i \quad i = 1,2,3\,, \tag{3.19}$$

where p_i and q_i denote the general canonical conjugate variables. These action integrals J_i are constants or *invariants of motion*, if the variation of the system p_i and q_i is *slow* compared to the motion of the particles within this system. In case of particle motion in an inhomogeneous magnetic field, the adiabaticity criterion is [Dub07]:

$$\gamma \equiv \frac{2\pi r}{B}\left|\frac{\partial B}{\partial z}\right| \ll 1\,, \tag{3.20}$$

with the gyration radius r and the B-field gradient in z-direction.

Following [Jac02], the two adiabatic invariants for motion of charged particles inside an inhomogeneous magnetic field are:

$$B \cdot r^2 = \text{const.} \quad \text{and} \quad \frac{p_\perp^2}{B} = \text{const.}\ . \tag{3.21}$$

Using eq. (3.16) together with the adiabatic invariance gives:

$$p_\parallel^2(z) = p^2 - p_\perp^2(z) \overset{(3.21)}{=} p^2 - p_{\perp,0}^2(z_0) \cdot \frac{B(z)}{B_0(z_0)}\ , \tag{3.22}$$

where $p_\parallel(z)$ is only a function of $B(z)$, assuming that momentum and magnetic field have a negligible dependence on the plane coordinates x and y. $B_0(z_0)$ and $p_{\perp,0}(z_0)$ denote the magnetic field strength and perpendicular momentum of a particle at a defined spatial point $z = z_0$, e.g. the decay point of the neutron. If the motion of that particle is towards an increasing magnetic field $B(z)$, the longitudinal momentum $p_\parallel(z)$ becomes zero at a certain point and finally changes the sign, which is equivalent to the reflection at a *magnetic mirror*.

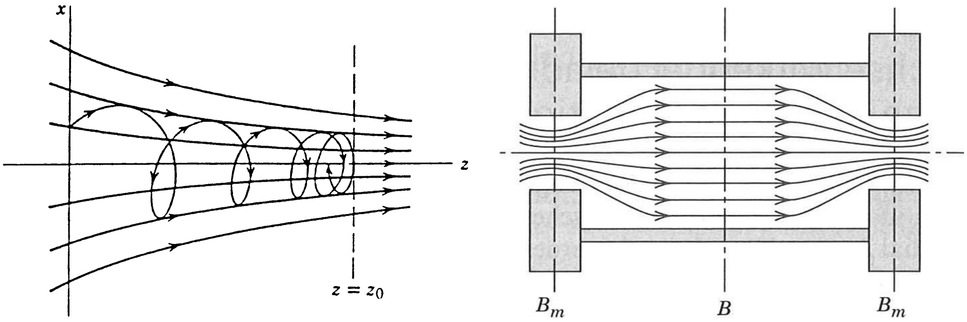

(a) Reflection of a gyrating charged particle at position $z = z_0$ due to the gradient of the magnetic field. Here, $p_\parallel(z_0)$ becomes 0.

(b) Example of a *magnetic bottle*. The charged particles do not overcome the magnetic barrier at the side walls.

Figure 3.6: Two examples for the effects of a magnetic mirror [Jac02].

In fig. 3.6 two examples of the magnetic mirror effect are shown: the reflection of a charged particle at an increasing magnetic field (fig. 3.6a) and a magnetic bottle, where particles are trapped between two magnetic barriers (fig. 3.6b).

Using eq. (3.22) the critical decay angle θ_{crit} for reflection at the magnetic mirror is a function of the decay point z and the ratio of the magnetic field $B(z)$ at this point to B_{max} (θ is the polar angle between $\mathbf{p}_{\mathrm{e}}$ and $\mathbf{p}_{\mathrm{n}}$, which is along $\mathbf{B}$):

$$\sin^2\theta_{\mathrm{crit}}(z) = \frac{p^2_{\perp,0}(z)}{p^2} = \frac{B_0(z)}{B_{\mathrm{max}}} \,. \tag{3.23}$$

In other words, all charged particles, which are created with $\theta_{\mathrm{decay}} \geq \theta_{\mathrm{crit}}$ with an initial flight direction towards a positive gradient of the magnetic field, are reflected at the magnetic mirror and therefore are not attributed to the correct detector hemisphere. Thus, the magnetic mirror effect can have a strong influence on the asymmetry, which has to be determined and corrected, see below.

As shown in fig. 3.7, the normalized probability distribution of the decay particles is a function of the decay angle θ and the velocity $\beta = v/c_0$, see eq. (5.76):

$$\begin{aligned} \mathrm{d}N &= (1 + A\,\beta\cos\theta)\,\frac{1}{4\pi}\,\mathrm{d}\Omega\,, \quad \text{integration over } \phi \;\Rightarrow \\ &= (1 + A\,\beta\cos\theta)\,\frac{1}{2}\,\sin\theta\,\mathrm{d}\theta \equiv p(\theta)\,\mathrm{d}\theta\,, \end{aligned} \tag{3.24}$$

where A is the β-asymmetry correlation coefficient.

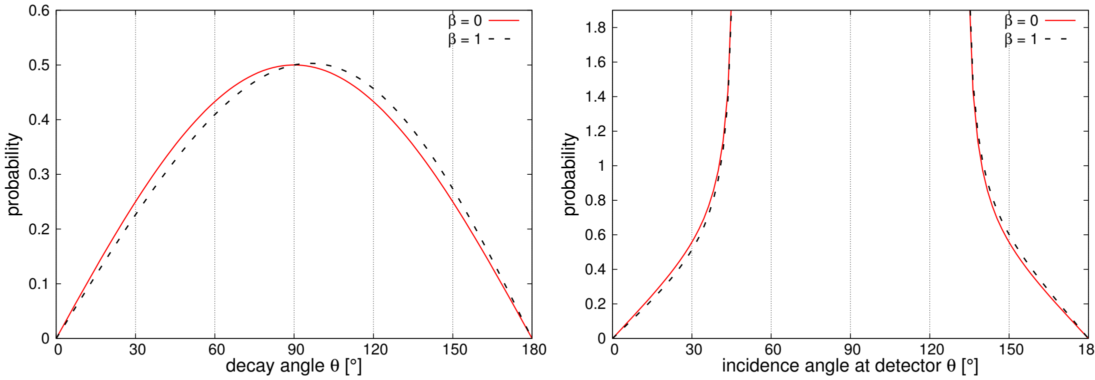

(a) Angular prob. distribution $\mathrm{d}N/\,\mathrm{d}\theta$ from eq. (3.24). Electrons with $\beta = 0$ in red and with $\beta = 1$ in dashed. The small shift is due to the asymmetry A.

(b) At the detectors the angular distribution diverges close to the limiting angle of 47°, see eq. (3.30). Angles $\theta > 90°$ pertain to incidents on the opposite detector.

Figure 3.7: Normalized probability distributions as function of the polar angle θ for electrons in the decay volume (left) and close to the detectors (right).

The majority of particles are created with θ close to 90°, which means that they start their motion to the detectors with an already small longitudinal momentum $p_{\|}(z)$. To minimize the magnetic mirror effect on the asymmetry, the gradient of the magnetic field inside the decay volume must be small. In summary, the requirements on the magnetic field design are:

- The magnetic field profile should be symmetrical about the center of the decay volume.
- The profile of the magnetic field has to be free of local minima to avoid creating magnetic bottles, which can store electrons for a certain time and therefore destroy their asymmetry information.
- Due to eq. (3.20) and (3.23) the magnetic field should be as homogeneous as possible inside the decay volume with a small negative gradient towards the two ends $\Rightarrow \theta_{\text{crit}}$ close to 90°.
- To reduce backscattering of electrons from the scintillation detectors (see section 5.1.4), the grazing incident onto the surface should be prohibited. This can be realized with a noticeable drop of the magnetic field strength close to the detectors, since (using eq. (3.21)):

$$\sin\theta_{\text{det}} = \sin\theta_{\text{decay}} \cdot \sqrt{\frac{B_{\text{det}}}{B_{\text{decay}}}} \,. \tag{3.25}$$

The magnetic field design of PERKEO III does satisfy these requirements. The field maximum along the beam axis is in the symmetry plane. $B(z)$ drops towards both ends of the decay volume (see fig. 4.3) by:

$$\left|\frac{\Delta B}{\Delta z}\right|_{\text{decay}} \cong \frac{(152.5 - 152.0)\,\text{mT}}{1\,\text{m}} \cong 0.5\,\text{mT/m}\,, \tag{3.26}$$

and towards the detectors by:

$$\left|\frac{\Delta B}{\Delta z}\right|_{\text{det}} \cong \frac{(152 - 80)\,\text{mT}}{2\,\text{m}} \cong 35\,\text{mT/m}\,. \tag{3.27}$$

With the radii from eq. (3.18) the adiabaticity in eq. (3.20) becomes:

$$\gamma_{\text{decay}} = \frac{2\pi \cdot 2.6\,\text{cm}}{0.15\,\text{T}} \cdot 0.5\,\text{mT/m} \lesssim 6 \cdot 10^{-4} \ll 1 \qquad \text{and} \tag{3.28}$$

$$\gamma_{\text{det}} = \frac{2\pi \cdot 3.6\,\text{cm}}{0.08\,\text{T}} \cdot 35\,\text{mT/m} \approx 0.1 \ll 1\,, \tag{3.29}$$

which fulfills the adiabaticity criterion. The angular distribution of the incident electrons at the detectors follows from eq. (3.24) and (3.25), using a variable transformation from θ_{decay} to θ_{det}:

$$\begin{aligned} \mathrm{d}N &= p(\theta_{\text{decay}})\,\mathrm{d}\theta_{\text{decay}} \\ &= p\left(\theta_{\text{det}}(\theta_{\text{decay}})\right)\cdot\frac{\mathrm{d}\theta_{\text{decay}}}{\mathrm{d}\theta_{\text{det}}}\,\mathrm{d}\theta_{\text{det}} = \ldots \\ &= \frac{\left(1 + A\,\beta\sqrt{1-\frac{\sin^2\theta_{\text{det}}}{B_{\text{det}}/B_{\text{decay}}}}\right)\sin\theta_{\text{det}}\cos\theta_{\text{det}}}{2\cdot B_{\text{det}}/B_{\text{decay}}\cdot\sqrt{1-\frac{\sin^2\theta_{\text{det}}}{B_{\text{det}}/B_{\text{decay}}}}}\,\mathrm{d}\theta_{\text{det}}\,, \end{aligned} \tag{3.30}$$

with the limiting angle $\theta_{\text{det}}^{\text{max}}$, given by the requirement of having a real value of the root:

$$\sqrt{1-\frac{\sin^2\theta_{\text{det}}}{B_{\text{det}}/B_{\text{decay}}}} \in \mathbb{R} \quad\Rightarrow\quad \theta_{\text{det}}^{\text{max}} = \arcsin\sqrt{\frac{B_{\text{det}}}{B_{\text{decay}}}} \cong 47^\circ\,. \tag{3.31}$$

The plots in fig. 3.7 show the angular dependent probability distributions of the electrons in the decay volume and at the detectors. In fig. 3.7b the effect of the adiabatic invariance is visible (const $= p_\perp^2/B$): due to the reduction of the magnetic field at the detectors the incident angle is limited (see eq. (3.31)), while the probability diverges at the limiting angle. Close to the detectors the magnetic field strength is $B \approx 80\,\text{mT}$, which corresponds to an upper limit of $\theta_{\text{det}}^{\text{max}} \cong 47^\circ \;\Rightarrow$ no grazing incident.

Besides this advantage, the low value for the B-field close to the detector has another benefit: the motion of electrons, which are backscattered from the scintillator (see section 5.1.4), is always towards an increasing magnetic field. Therefore about 50 % of the backscattered particles are reflected at the magnetic mirror and hit the same detector again.

To verify the absence of local minima, the profile of the magnetic field was measured before the beamtime. It turned out that there were two symmetric minima inside the decay volume. This was corrected before the measurement, see section 4.4.1 and fig. 4.3.

Correction of the Magnetic Mirror Effect

The wrong assignment of particles to the detection system due to the magnetic mirror effect has to be corrected. To derive this correction, the electrons which hit e.g. detector 1 have to be identified:

N_1: created in half-space of detector 1, initial momentum towards detector 1

N_2: created in same half-space, opposite flight direction, reflected at the magnetic mirror

N_3: created in half-space of detector 2, initial momentum in direction of detector 1, which overcome the maximum of the magnetic field

The individual values for N_i are derived as follows:

$$N_i^{\uparrow,\downarrow}(E) = F(E) \cdot \frac{1}{V} \int\limits_{H_j} \mathrm{d}^3 r \int\limits_{\theta_{i,1}}^{\theta_{i,2}} \frac{1}{2} \rho(\mathbf{r})(1 \pm A\,\beta(E)\cos\theta)\sin\theta\,\mathrm{d}\theta\,, \tag{3.32}$$

with the spatial dependent neutron density $\rho(\mathbf{r})$, the phase-space factor $F(E)$ and the corresponding integration limits $\theta_{i,1}$ and $\theta_{i,2}$ with $i=1,2,3$. H_j with $j=1,2$ denote the respective half-spaces of detector 1 and 2 inside the decay volume. Using eq. (3.23), (3.32) and $\theta_{\mathrm{crit}}=f(B(\mathbf{r}))$, the experimental asymmetry becomes [Rav95]:

$$\begin{aligned} A_{\mathrm{exp}} &= \frac{N^{\uparrow} - N^{\downarrow}}{N^{\uparrow} + N^{\downarrow}} \\ &= \frac{A\,\beta}{2} \cdot \frac{\int\limits_{H_1+H_2} \rho(\mathbf{r}) \sin\theta_{\mathrm{crit}}(\mathbf{r})\,\mathrm{d}^3 r}{\int\limits_{H_1+H_2} \rho(\mathbf{r})\,\mathrm{d}^3 r + \int\limits_{H_1} \rho(\mathbf{r}) \cos\theta_{\mathrm{crit}}\,\mathrm{d}^3 r - \int\limits_{H_2} \rho(\mathbf{r}) \cos\theta_{\mathrm{crit}}\,\mathrm{d}^3 r}\,. \end{aligned} \tag{3.33}$$

Introducing the definitions:

$$M = \frac{\int\limits_{H_1+H_2} \rho(\mathbf{r}) \sin\theta_{\mathrm{crit}}(\mathbf{r})\,\mathrm{d}^3 r}{\int\limits_{H_1+H_2} \rho(\mathbf{r})\,\mathrm{d}^3 r} \lesssim 1 \qquad \text{and} \tag{3.34}$$

$$k = \frac{\int\limits_{H_1} \rho(\mathbf{r}) \cos\theta_{\mathrm{crit}}(\mathbf{r})\,\mathrm{d}^3r - \int\limits_{H_2} \rho(\mathbf{r}) \cos\theta_{\mathrm{crit}}(\mathbf{r})\,\mathrm{d}^3r}{\int\limits_{H_1+H_2} \rho(\mathbf{r})\,\mathrm{d}^3r} \ll 1\,, \tag{3.35}$$

the corrections on the asymmetry at detector 1 and detector 2 follow:

$$A_{1,\mathrm{exp}}(E) = \frac{A_1\,\beta(E)}{2} \cdot \frac{M}{1+k} \quad \text{and} \quad A_{2,\mathrm{exp}}(E) = \frac{A_2\,\beta(E)}{2} \cdot \frac{M}{1-k}\,, \tag{3.36}$$

where k is a measure for the *asymmetry* of the magnetic field, weighted by the particle density $\rho(\mathbf{r})$ with respect to the central point of the decay volume, and M is sensitive to the homogeneity and the gradient of the magnetic field. The asymmetry correlation coefficients A_1 and A_2 for the two detectors are derived by fitting the function $\beta(E)$ to the respective asymmetry spectra $A_i(E)$, see eq. (5.76). Averaging A_1 and A_2 yields an even smaller correction:

$$\frac{1}{2}\left(\frac{M}{1+k} + \frac{M}{1-k}\right) = \frac{M}{1-k^2}\,, \tag{3.37}$$

since $k \ll 1$. The absolute values for M and k do not only depend on the magnetic field profile inside the decay volume, but also on the time of flight behavior and the density $\rho(\mathbf{r})$ of the neutron pulse,[7] see section 5.2.

3.3.2 Electron Detection System

The spectrometer PERKEO III provides a symmetric $2\times 2\pi$ detection system. To detect the electrons from neutron decay, plastic scintillators with six photomultipliers attached were used for each detector.

Plastic Scintillator

A plastic scintillator, which consists of a solid solution of organic scintillation molecules in a polymerized solvent, is sensitive to different types of radiation: e.g. X-ray, γ-ray, fast neutrons and charged particles. The scintillation light of a typical plastic scintillator has its maximum at $\lambda \approx 420\,\mathrm{nm}$ with a decay time of about 2 ns. Figure 3.8 shows a schematic and a picture of a PERKEO III

---

[7] The particle density $\rho(\mathbf{r})$ corresponds to the modified neutron density, according to the gyration-profile of the electrons.

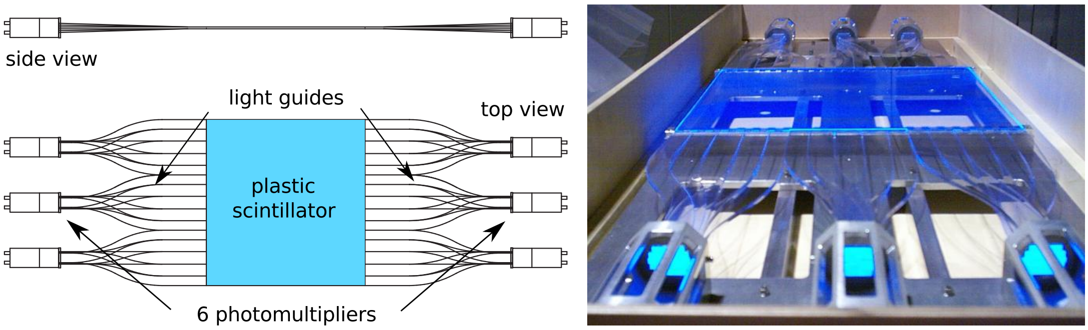

Figure 3.8: Schematic (left) and picture (right) of the scintillation detector. The six photomultipliers are connected via light guides to the $40 \times 40\,\mathrm{cm}^2$ plastic scintillator. In the picture the blue scintillation light is clearly visible.

detector. The photons from the scintillation process (blue light) are guided to the photomultipliers, where the optical energy is converted to an electrical signal. Some specific data on the used scintillators are [Bic]:

- Supplier and type: BICRON BC-400
- Refractive index: $n = 1.58$
- Light attenuation length: $x_{\mathrm{att}} = 160\,\mathrm{cm}$
- Maximum of wavelength distribution: $\lambda = 423\,\mathrm{nm}$

The size of the scintillator plate is about $40 \times 40\,\mathrm{cm}^2$, which covers the complete electron beam including the gyration radii. Since the photomultipliers are attached symmetrically on both sides, the total light attenuation can be described with a cosh-function. Assuming that the full covered area of the incoming electron beam is about $20 \times 20\,\mathrm{cm}^2$ [Dub08b], the non-uniformity from the intrinsic attenuation of the scintillation light at $x = 0.5 \cdot \mathrm{width}$ becomes:[8]

$$1 + \frac{\Delta E}{E} = \cosh \frac{0.5 \cdot \mathrm{width}}{x_{\mathrm{att}}} = \cosh \frac{10\,\mathrm{cm}}{160\,\mathrm{cm}} \cong 1 + 0.2\,\% \; . \tag{3.38}$$

Photomultipliers

Some specific data on the used photomultipliers (details in appendix B.3):

- Supplier and type: Hamamatsu R5504/R5924

---

[8] Because of the symmetric detector setup in x-direction (see fig. 3.8) and the Lambert-Beer-Law, which describes light absorption processes e.g. in a scintillator, the intensity follows the function $\mathrm{e}^{(x-x_0)/x_{\mathrm{att}}} + \mathrm{e}^{-(x-x_0)/x_{\mathrm{att}}}$, which is proportional to $\cosh \frac{(x-x_0)}{x_{\mathrm{att}}}$.

- Current amplification V_I: $1 \cdot 10^7$ at $B = 0\,\mathrm{T}$, $2.5 \cdot 10^5$ at $B = 1\,\mathrm{T}$
- Spectral response: 300–650 nm
- Wavelength of maximum response: 420 nm
- Number of mesh dynodes: 19
- Maximum high-voltage: 2300 V
- Quantum efficiency: $p \cong 26\,\%$ at 390 nm
- Cathode sensitivity: 70 µA/lm

With the given current amplification of the photomultipliers V_I and the approximate length of the created pulse $\Delta t \approx 20\,\mathrm{ns}$, the current and therefore the voltage of the resulting signal from one photo-electron can be estimated:

$$Q = V_\mathrm{I} \cdot e_0 = 10^7 \cdot 1.6 \cdot 10^{-19}\,\mathrm{As} = I \cdot \Delta t\;, \quad \Rightarrow \tag{3.39}$$

$$I = \frac{Q}{\Delta t} \cong 80\,\mu\mathrm{A} = \frac{U}{R}\;, \quad \text{with } R = 50\,\Omega \quad \Rightarrow \tag{3.40}$$

$$U \cong 4\,\mathrm{mV}\;. \tag{3.41}$$

This value of voltage U was chosen as discriminator threshold, see sec. 3.6.2.

Improvements since the last Beamtime

As mechanical stress due to thermal expansion of the scintillator was assumed to be one of the reasons for the poor detector function during the 2007-beamtime, the mounting of the scintillators to the support was modified. Once the detectors were mounted to the spectrometer, only water was used for cleaning, no Isopropanol or Aceton. The applied high-voltage of the photomultipliers has a strong influence on the position dependent detector response. Therefore the adjustment was performed very carefully. As a consequence of these measures, the detector uniformity could be increased noticeably compared to the PERKEO III measurement in 2007 (see section 5.1.2).

3.3.3 Vacuum System

One potential influence, which could disturb the particles inside the PERKEO III vacuum vessels, is scattering with the residual gas. This would result in a change of energy and direction of motion. The mean free path of particles depends on temperature, the type of the residual gas and pressure p. With the chosen pressure limit of $p < 1 \cdot 10^{-6}$ mbar the corresponding H_2O equivalent thickness of the residual gas is:

$$\begin{aligned} d &= \underbrace{\frac{l}{2}}_{\text{length}} \cdot \underbrace{\frac{p}{k_B T}}_{\text{residual density}} \cdot \underbrace{\frac{m_{\text{mol}}^{\text{H}_2\text{O}}}{N_A\,\rho_{\text{H}_2\text{O}}}}_{\text{recip. of H}_2\text{O density}} \\ &\approx 3 \cdot 10^{-2}\,\text{Å}\,, \end{aligned} \tag{3.42}$$

with l denoting the length of PERKEO III and temperature $T = 300$ K. To estimate the resulting energy loss of the residual gas, the parameters of the energy loss function in eq. (5.13) are taken from Monte Carlo simulations of the plastic scintillator BC400, see section 5.1.1 and eq. (5.9). On average, electrons of 1 keV loose about $2 \cdot 10^{-5}$ of the energy due to the residual gas at $p = 1 \cdot 10^{-6}$ mbar.[9]

For another reason it is important to have a low vacuum pressure: the used photomultipliers from company Hamamatsu with the attached voltage-divider circuits work well at ambient pressure or below a threshold of $p \leq 1 \cdot 10^{-4}$ mbar. To operate them in an intermediate pressure range can damage the voltage-divider network due to internal flash-over. Hence, the pressure was not only monitored but also an additional *kill-circuitry* was developed and installed. This protection system immediately disabled the high-voltage system of the photomultipliers in case of a pressure jump above a threshold of $p \geq 3 \cdot 10^{-5}$ mbar.

3.3.4 Beam Stop

Cold neutrons can easily be eliminated by capture in materials with a high neutron absorption cross section. Table 3.1 shows some commonly used materials in neutron physics together with their capture cross sections and absorption lengths. Most materials create primary γ-radiation, while others trigger secondary reactions, which could generate fast neutrons.

The properties of a neutron beamstop inside the spectrometer should be:

- Complete absorption of the neutron pulse,
- Minimal generation of γ-radiation,
- Small number of backscattered or secondary neutrons.

---

[9] The energy loss $\mathrm{d}E/\mathrm{d}x$ in organic scintillators increases for low particle energies, see section 5.1.1.

Isotope	**Cross section** σ **[barn]**	**Absorption length** ξ **[cm]**	γ**-ray**	**Secondary Fast Neutrons**
^{3}He	$5.3 \cdot 10^{3}$	$7.4\ (p \cong 1\,\text{bar})$	no	
^{6}Li	$9.4 \cdot 10^{2}$	$2.24 \cdot 10^{-2}$	no	93
^{10}B	$3.8 \cdot 10^{3}$	$1.92 \cdot 10^{-3}$	yes	0.5
^{113}Cd	$2.1 \cdot 10^{4}$	$8.56 \cdot 10^{-3}$	yes	
^{157}Gd	$2.6 \cdot 10^{5}$	$1.31 \cdot 10^{-4}$	yes	

Table 3.1: Commonly used materials as neutron absorbers with their cross sections and absorption lengths [Ndb]. The number of secondary fast neutrons (per 10^{6} captures) is only given for the materials used [LSI80].

Initial tests were performed with ^{6}LiF as absorber, which is the optimum material in continuous beam measurements. But in case of a pulsed neutron beam measurement some drawbacks appear. Therefore the beamstop had to be replaced by an enriched boron carbide $^{10}B_4C$ absorber (details in section 4.4.2).

3.3.5 Shielding

To protect the Perkeo III detection system from ambient (section 3.4.1) and beam related background (sections 4.4.2, 4.4.3 and 5.3.2), some 10 cm of boron plastic and lead were put between the beamline and the vessel of detector 1. This detector was also shielded against γ-ray coming from the casemate (polarizer and velocity selector). Because of space reasons, detector 2 could only be shielded by about 5 cm of lead against the γ-radiation from the beamstop. With these measures the time dependent radiation could be eliminated and the constant radiation background sufficiently reduced, see section 5.3.

3.4 Disc Chopper – Pulsed Neutron Beam

Previous neutron decay measurements with spectrometers of the Perkeo-family were performed with a continuous neutron beam. This method has the (only but considerable) advantage of having a quite high eventrate of decay products. During the first Perkeo III measurement in 2007 raw eventrates of about 50 kHz were obtained.

3.4.1 Advantages and Challenges of a Pulsed Neutron Beam

A neutron pulse, created by chopping the continuous beam, has a definite length in space–time, see fig. 3.9. By utilizing an appropriate chopper design and frequency, this pulsed beam allows to measure the decay products (signal) and the background during separate chosen time windows in the time of flight spectrum.

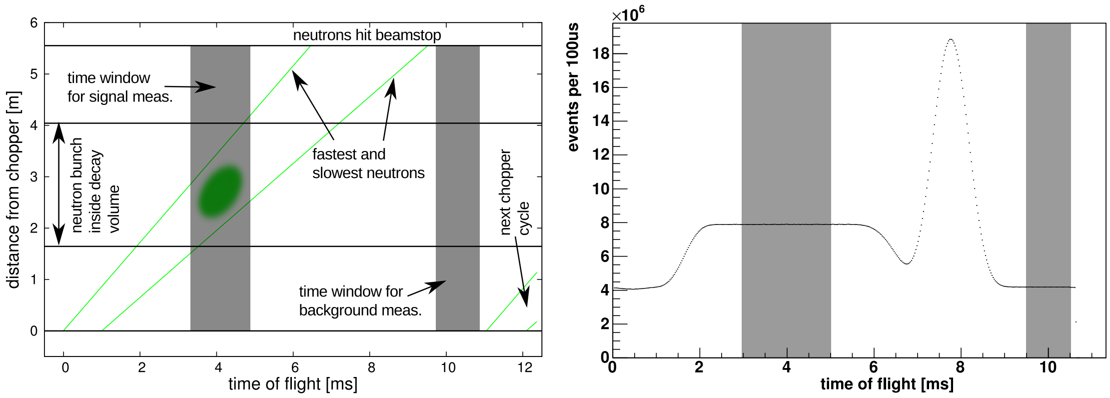

Figure 3.9: Left: space–time diagram of the pulsed beam. The green diagonal lines represent the limits for the neutron velocity distribution and the gray areas mark the time windows for signal- and background-measurement. The chopper opens at $t \equiv 0$ for a period of less than 1 ms. At $t \approx 4$ ms the neutron pulse is completely located inside the decay volume (signal time window). Later at $t \approx 10$ ms all neutrons are absorbed in the beamstop and the next chopper cycle has not yet started – the background is measured then.
Right: the ToF spectrum shows the raw measured events as function of the time of flight with respect to the chopper timing. The rise in countrate at $t \approx 8$ ms is caused by γ-radiation due to the neutron absorption at the beamstop.

The space–time diagram of one chopper cycle is shown in fig. 3.9 (left) together with the measured time of flight spectrum (right). The corresponding time windows for signal- and background-measurements are marked in gray. During its motion through the spectrometer towards the beamstop, the neutron pulse widens in space–time. The limiting particles are the fastest neutrons at the beginning of the opening function and the slowest at the end. This dispersion induces the necessity of using the velocity selector, see section 3.1.2. When the neutrons enter the decay volume at about $t \approx 2$ ms, the countrate measured with the Perkeo III detectors increases, see right plot in fig. 3.9. At $t \approx 10$ ms the neutron pulse is completely absorbed in the beamstop.

Beam Related Background

Since signal $S(E)$ and background $B(E)$ can be measured separately for every chopper period of $t \approx 10\,\text{ms}$, the background-free energy spectrum $N(E)$ can be determined using:

$$N(E) = S(E) - B(E)\ . \tag{3.43}$$

This subtraction is suitable under the following assumption: the measured background $B(E)$ during its time window has the same intensity and spectral distribution compared with the existing background during the signal time window, which is not directly measurable. This statement describes at the same time the advantage but also the challenge of a pulsed beam measurement. Several measures and analysis were performed during the beamtime and the data analysis to assure this condition (see sections 4.2 and 5.3).

Beam Independent Background

Since an external source of background radiation is not synchronized with the periodicity of the neutron pulse, beam independent background is exactly accessible in a pulsed neutron beam measurement, see section 5.3.3.

To determine the background in a continuous beam measurement, the neutron beam has to be switched off for a certain time, e.g. some minutes. But with disabled neutron beam, the present background is not exactly the same as with activated beam. There is one additional background source, the closed main shutter, while some other possible background sources are missing, e.g. beamstop and collimation system. Hence, a non-trivial procedure of background measurements with several neutron shutters at different positions and a subsequent data processing is necessary to estimate the existing background during the neutron decay measurement.

Edge Effect

The Edge Effect describes the influence of border conditions to the beam of charged decay products on their way towards the detectors. Electrons, which are created inside the decay volume of PERKEO III, are projected perfectly to the detectors independently of their energy E and decay angle θ. This does not hold for electrons created inside the two detector vessels, see fig. 3.5. In this case the projection depends on energy and decay angle of the particles [Mär06]. The resulting systematic effect on the measured spectra was of the order $\mathcal{O}(5 \cdot 10^{-2})$ in previous PERKEO II measurements [Mun06, Sch07a]. Using a pulsed neutron beam gives the opportunity to choose an appropriate time window for signal measurement and therefore a 100 % edge-free determination is possible.

3.4.2 Technical Realization and Implementation

Technically there are several principles to generate a pulsed neutron beam. Three of them are:

- Fermi Chopper: A Fermi chopper is a rotating system of several parallel blades, which are coated with a neutron absorber. During one 360° turn the chopper opens the beam twice. A schematic of a Fermi Chopper is shown in appendix B.2.
- ^{3}He-cell: As described in detail in appendix B.1, polarized ^{3}He absorbs neutrons with the corresponding spin. Therefore an appropriate system of spin-flipper and ^{3}He-cell is able to produce a pulsed polarized beam.
- Disc chopper: A rotating disc coated with a neutron absorber. Either one or more orifices in the disc allow the neutron beam to pass through for a defined period of time.

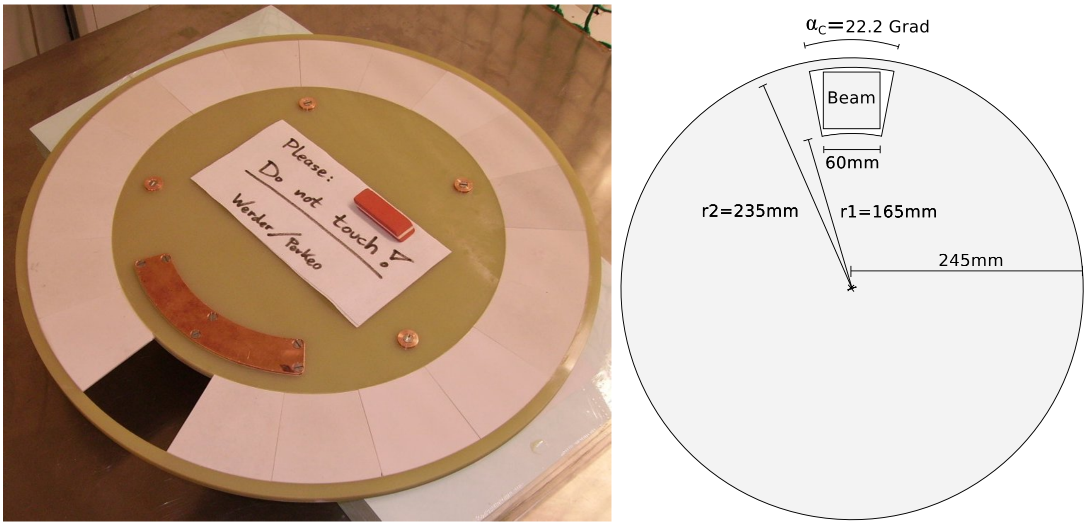

Figure 3.10: Picture (left) and schematic (right) of the disc chopper [Wer09]. The 18 white ^{6}LiF plates are about 4.5 mm thick and glued onto the base material of the disc (GFRP glass fiber reinforced plastic), which is additionally coated with Gadolinium at the back side. The visible copper parts were added during the rotation–balance test.

The disc chopper principle was chosen for the 2008/09 beamtime [Wer09, Mär06]. Figure 3.10 shows a picture and a schematic of the assembled chopper. The neutron absorbing plates are made of ^{6}LiF, which interacts with neutrons as follows:

$$ {}^6_3\mathrm{Li} + n \longrightarrow {}^4_2\mathrm{He} + {}^3_1\mathrm{H} + 4.785\,\mathrm{MeV}\ . \tag{3.44}$$

In table 3.1 the most common neutron absorber materials with their absorption cross sections are listed. The advantage of ^{6}LiF is the low intensity of γ-radiation from neutron absorption, whereas some fast neutrons can be produced due to secondary processes triggered by the Tritium. This topic is addressed more profoundly in section 3.3.4 and 4.4.3.

The chopper disc was driven by a DC motor, with a rotation control system based on a microcontroller (ATmega128 CPU). To obtain the ToF spectrum in fig. 3.9, the chopper frequency had to be of the order of $f_{\mathrm{ch}} \approx 100\,\mathrm{Hz}$ with an opening ratio of about 6 %. Some characteristics on the disc chopper are:

- Diameter: 49 cm, weight: 4.1 kg
- Opening angle: 22.2°, opening ratio: 6 %
- Nominal rotation frequency for highest eventrate: $f_{\mathrm{opt}} = 95\,\mathrm{Hz}$
- Accuracy of frequency regulation: $\mathcal{O}(1 \cdot 10^{-4})$
- Kinetic energy at nominal frequency: $E_{\mathrm{kin}} \cong 22\,\mathrm{kJ}$[10]
- Acceleration[11] with $f = f_{\mathrm{opt}}$ at the edge of the disc: $a = \omega^2 r \approx 9000 \cdot g$

The plots in fig. 3.11 show a histogram of the chopper frequency distribution and the measured opening function in the decay volume. This opening function was measured, placing an aluminum plate in the neutron beam at the beginning of the decay volume and counting the resulting radiation with a γ-detector. The FWHM length of the pulse is about $\Delta t_{75\,\mathrm{Hz}} \approx 0.9\,\mathrm{ms}$ and therefore $\Delta t_{94\,\mathrm{Hz}} \approx 0.7\,\mathrm{ms}$ (compare with fig. 5.15 and 5.16).

The expected peak eventrate of decayed neutrons during the dwell time of the neutron pulse inside the decay volume can be estimated using:

- Total number of polarized neutrons: $N \approx 3 \cdot 10^9\,\mathrm{s}^{-1}\mathrm{cm}^{-2}$ (section 3.1.1)
- Transmission coefficient of velocity selector: $TC \approx 20\,\%$ (section 3.1.2)

---

[10] This corresponds to the kinetic energy of a car with $m = 1000\,\mathrm{kg}$, driving with $v \cong 24\,\mathrm{km/h}$.

[11] The high acceleration is the reason for the necessity of a special protection guard around the chopper housing, see also section 4.1.

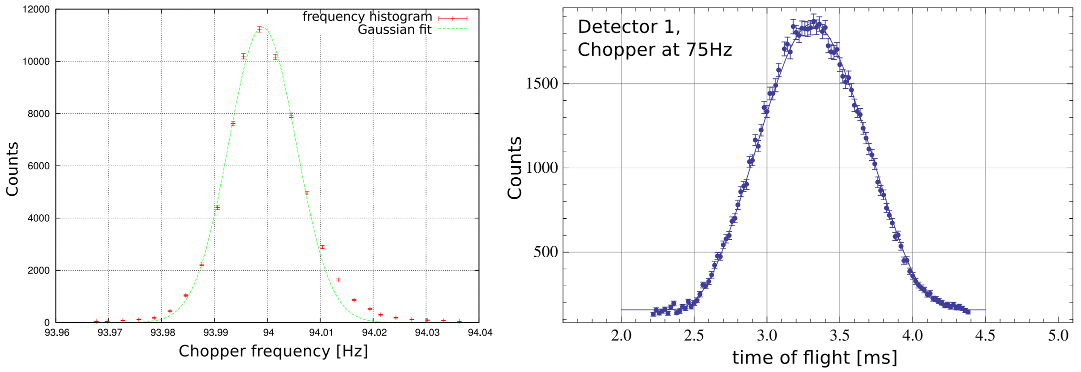

(a) Histogram of chopper frequency distribution in May 2009 together with a Gaussian fit. The stability is of the order $\mathcal{O}(1\cdot 10^{-4})$.

(b) Opening function of the chopper, measured with an aluminum plate at the beginning of the decay volume and a γ-detector close to it (see also section 4.2.2).

Figure 3.11: Frequency distribution and opening function of the chopper, measured during the beamtime [Wer09].

- Illuminated area: $A \approx 6\times 6\,\text{cm}^2$ (section 3.2.2)
- Life time of the neutrons: $\tau_\text{n} \cong 886\,\text{s}$
- Chopper frequency: $f_\text{ch} = 94\,\text{Hz}$
- Dwell time of the neutron pulse in the decay volume: $t_\text{dwell} \cong 2\,\text{ms}$
- FWHM length of neutron pulse[12]: $t_\text{b} = \frac{1}{2}\cdot\frac{22.2^\circ}{360^\circ}\cdot\frac{1}{f_\text{ch}} + \frac{6\,\text{cm}}{2\pi f_\text{ch}\cdot r_\text{ch}} = 0.74\,\text{ms}$

Now the peak rate becomes:

$$R \approx \underbrace{N\cdot TC\cdot A\cdot t_\text{b}}_{\text{neutrons in pulse}} \cdot f_\text{ch}\cdot \underbrace{\frac{t_\text{b}}{\tau_\text{n}}}_{\text{decay ratio}} \approx 1.2\,\text{kHz}\,, \tag{3.45}$$

which is rather close to the measured rate of $R_\text{meas} \approx 1.1\,\text{kHz}$, see eq. (5.67) in section 5.5. The mean eventrate follows:

$$R_\text{mean} = R\cdot f_\text{ch}\cdot t_\text{dwell} \approx 240\,\text{Hz}\,. \tag{3.46}$$

This eventrate is of the same order as the last β-asymmetry measurement with PERKEO II, where a continuous beam was used, see section 6.4.1 and [Mun06].

---

[12] The estimation for the FWHM length is that the beam has 100 % density during t_b, therefore the factor ½ in the equation. The value of 6 cm describes the horizontal width of the neutron beam, which the chopper has to cross.

3.5 Calibration Scanner with Radioactive Sources

The energy of the decay electrons varies from $E = 0\,\mathrm{keV}$ to the endpoint energy of the neutron decay of $E_0 = 782\,\mathrm{keV}$. To calibrate the PERKEO III detection system over this broad energy range, five radioactive sources (decay mode: electron capture decay ε) with different energy peaks were used.

Isotope	Energy peak [keV]	Half-life	Decay mode	Rate [kHz]
^{109}Cd	75	461.4 d	ε	n.a.
^{139}Ce	132	137.6 d	ε	2.2
^{113}Sn	369	115.1 d	ε	2.2
^{207}Bi	503, 995	32.9 y	ε	1.4
^{137}Cs	630	30.1 y	ε, β^-	33

Table 3.2: Radioactive calibration sources with their energy peak, half-life, decay mode[13] and measured eventrate. The energy peaks are calculated without the contributions of Auger electrons (see below).

These calibration sources are listed in table 3.2 together with their respective energy peak. The source ^{109}Cd was not used during the beamtime due to mechanical problems with the calibration apparatus, see below. The rate (dose) of the sources was chosen to be close to the expected neutron decay rate of the pulsed beam (except for ^{137}Cs). For most of the calibration sources, electron capture ε is the only decay mode, while ^{137}Cs has additional β^- decay modes. The resulting energy of this nuclear decay can be released by emitting either a γ-quant or a so-called conversion electron. Due to direct interaction of the excited nucleus with an electron of the atomic orbitals, this electron can be emitted instead of a γ-quant. Therefore the conversion electrons have discrete energy values, in contrast to electrons from β-decay (three body decay).

Due to the electron capture of the nucleus and the possible subsequent emission of a conversion electron, either one or two states in the atomic orbitals are vacant. During the occupation of these states, either characteristic X-ray or so-called Auger electrons are emitted, which leaves another vacancy in the atomic orbital. This process could result in an Auger electron cascade, see theoretical description of ^{207}Bi in table B.1. There are several different probabilities existing for the processes of conversion and Auger decay [Roi10, Rav95, Arn87].

---

[13] From: http://www.nndc.bnl.gov/.

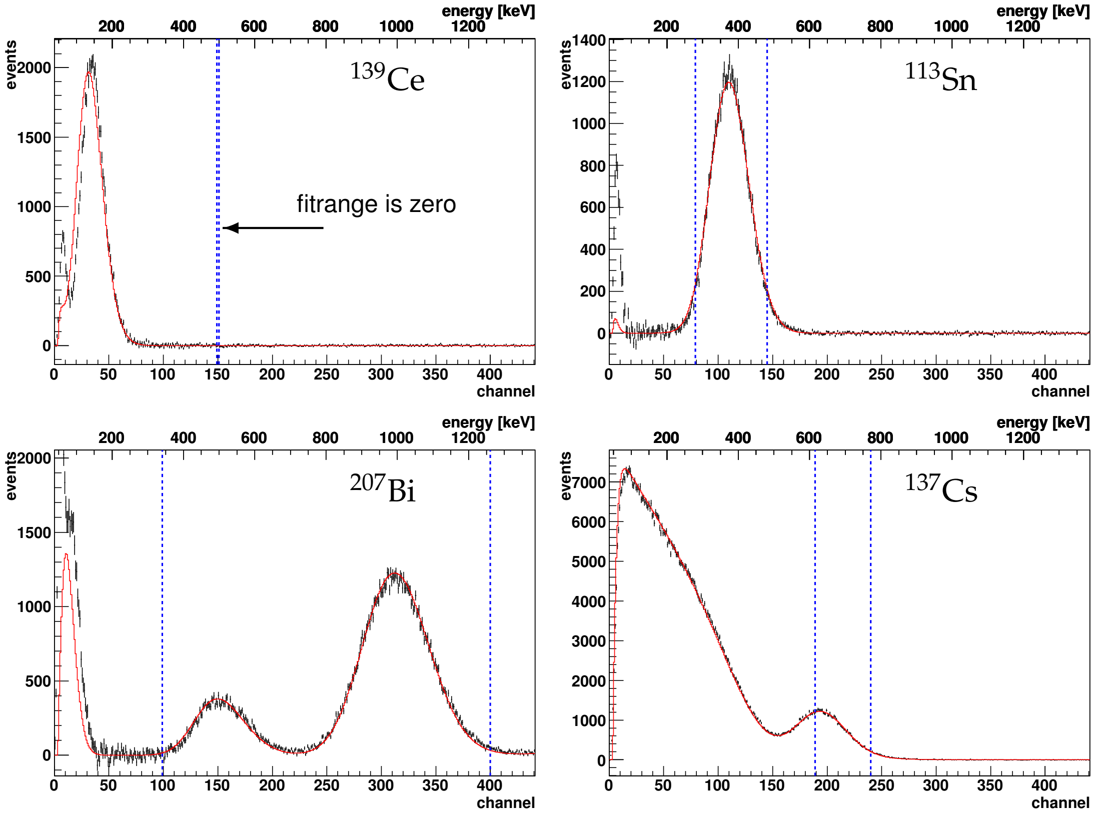

Figure 3.12: Measured spectra of used calibration sources (black) together with a simultaneous fit (red) with two free parameters offset O and gain g. The respective fitranges are between the two blue vertical lines. Due to the non-linearity of the detector for low energies, the cerium peak (upper left) is omitted in the fit, more details regarding non-linearity in section 5.1.1.

The software tool *p3fit*,[14] which is used to fit the measured spectra, utilizes a database of energy lines and the respective intensities for each calibration source. An internal routine applies Poisson and Gaussian broadenings[15] to the discrete energy lines, which form broad peaks that are used to fit the measured spectra, see appendix B.7 and fig. B.5. Figure 3.12 shows an example of a calibration measurement with the existing sources together with a simultaneous fit to all available spectra. The used fitrange of each source is emphasized with two vertical dashed blue lines. Because of the non-linearity of the detectors for

---

[14] Another in-house development, using C++.

[15] The Poisson broadening describes the discrete conversion processes in the scintillator and at the first photo-cathode of the photomultipliers and the Gaussian broadening accounts for subsequent processes in the photomultipliers and LinearFanOuts.

low energies, the source ^{139}Ce was omitted in the fit. The details on detector calibration are discussed in section 5.1.1.

Calibration Scanner

The calibration scanner was positioned in the center of the spectrometer. As shown in fig. 3.13, five holders with the radioactive sources are connected to a system of vertical and horizontal stepper motors, which is used to drive the individual sources to the chosen plane positions. While the neutron decay measurement is running, the holders are *parked* in the lower left position between two aluminum plates. During the beamtime one of the vertical motors did not work properly, therefore the source ^{109}Cd was removed.

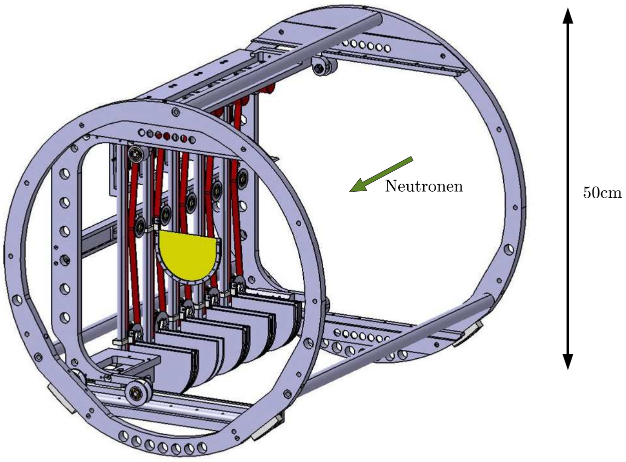

Figure 3.13: Schematic representation of the calibration scanner, positioned inside the decay volume at the center. During the measurement of neutron decay data, the five holders of the radioactive sources (highlighted in yellow) were located at their lower left parking position between two aluminum plates outside the neutron beam. For calibration and drift measurements the neutron beam was interrupted and the selected radioactive source was driven to the chosen plane-position.

3.6 Data Acquisition System

The Data Acquisition System consists of the control software *Dackel*, an ordinary IBM compatible computer and the read–out electronics. Several parts of the *Dackel* software as well as the electronics were adapted after the 2007 beamtime. For instance, the timing of the chopper had to be measured and synchronized with the data acquisition. Parts of the digital electronics, which previously caused reflected and *ghost* pulses (double pulses), were improved and finally the old ADC modules were replaced by new parts, which were developed especially for this measurement.

3.6.1 Software *Dackel* and Computer System

The acronym *Dackel*[16] is an abbreviation for "Data Acquisition and Control of Electronics". It is an in-house development, based on the object oriented programming language C++. Due to the considerable increase in countrate for the continuous beam measurement with PERKEO III in 2007 compared with previous PERKEO II measurements (50 kHz vs. 300 Hz), new DMA (Direct Memory Access) features as well as other improvements had to be implemented [Kap07].

During the 2009 beamtime an ordinary Personal Computer with the Linux operating system CentOS 5.3 was used. The communication between the PC and the read–out electronics (see section 3.6.2) was provided by a pair of interface cards from company Struck:

- SIS1100: PCI-card with optical interface
- SIS3100: VME-interface with read–out performance of 25 MB/s

The measured data were saved in a file format using the ROOT[17] data analysis framework from CERN (Conseil Européen pour la Recherche Nucléaire). For each measured event, the following information was stored:

- Energy of the event: 12×2 bytes $+ 2 \times 4$ bytes $=$ 32 bytes
- Event time, delta time: 2×4 bytes $=$ 8 bytes
- TDC time detsum: $2 \times 4 \times 4$ bytes $=$ 32 bytes
- TDC time single ADCs: $12 \times 3 \times 4$ bytes $=$ 144 bytes
- Chopper time, delta chopper time: 2×4 bytes $=$ 8 bytes
- Cycle, Latch, DetFirst: 3×4 bytes $=$ 12 bytes

---

[16] *Dackel* is the successor of the in-house software system **MOPS**, which was the "**M**easuring and **OP**erating **S**ystems" of the predecessor experiment PERKEO II. The "k" in *Dackel* is added to get a German word, which describes, as the old *MOPS*, a type of dog.

[17] See: http://root.cern.ch/.

This is in total 236 bytes per event. For each measurement cycle of $t = 10\,\mathrm{s}$ another 20 bytes were stored. With an average measured eventrate of about 2 kHz, a total number of 32 cycles per file and enabled file compression, the size of each data file became about 25 MB. During the beamtime some 10000 datasets were created. Together with drift-, scan- and calibration-measurements the size of the full dataset totaled 700 GB.

To control the calibration system, another in-house software system was used with the same PC. The chopper, the monitoring system and the main neutron shutter[18] inside the neutron guide were controlled by separate computer systems.

3.6.2 Electronics – Setup and Circuitry

The electronic setup, mounted in a water–cooled cabinet (VARISTAR + LHX3 from company Schroff) can roughly be separated in two parts:

- Analog part: energy information of an event, measured with ADCs (Analog to Digital Converter),
- Digital part: trigger and decision logic, time information of an event and the chopper, monitoring logic.

Additionally, the chopper control and supply as well as the high-voltage system of the photomultipliers were located in this cabinet. Using a water-cooling system, the temperature was stabilized to about 30 °C and monitored with two temperature sensors: one close to the preamplifier of the photomultiplier signal (LinearFanOut), the other one close to the ADCs.

In the following sections the two major parts of the electronic setup are briefly described. The development of the new ADC modules is addressed in sec. 3.6.3.

Analog Part

Figure 3.14 shows the block diagram of the analog part of the electronics. The six signals from each detector are connected to the LinearFanOuts. The information from the subsequent *constant fraction discriminators* (V812 / C808 from CAEN) is processed in the digital part of the electronics. At the beginning of the 2009

---

[18] The main shutter of the neutron guide H113 was controlled by a system called *Nomad*. This was used as a master control system, which was able to trigger the *dackel* system.

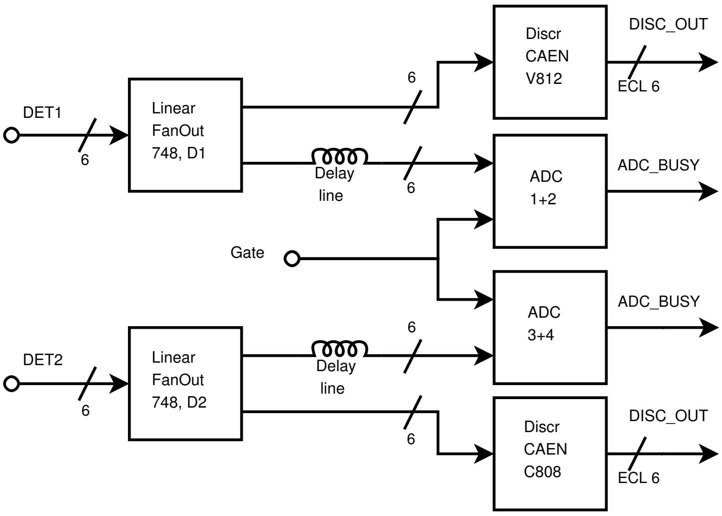

Figure 3.14: Analog part of electronics. The six photomultiplier signals from each detector are amplified and distributed to the ADC modules via 300 ns delay lines and in parallel to the discriminators.

beamtime, a cross talk between the discriminator signals of detector 1 and 2 was observed. Because of that, the signals from detector 2 were connected to separate discriminators and coincidence units, see section 4.4.5.

The analog signals coming from the LinearFanOuts are delayed by about $t_\mathrm{d} \approx 300\,\mathrm{ns}$ with a simple delay line and measured with the ADCs. This delay is necessary due to signal propagation times in the decision and signal processing parts of the electronics (see below). Finally, the *gate* signal is used to signalize an incoming event, which should be measured by the ADCs.

The discriminators and the ADCs are located in a VME crate, which is connected to the PC system via an optical link. The buffers of the ADC modules have a finite size. To avoid buffer overflows, the so-called polling technique with an appropriate polling time was applied. During the readout of the ADCs, the signal *ADC_busy* is set to TRUE, which inhibits the digital part from creating a new *gate* signal – see below.

Digital Part

The main tasks of the digital electronics are: measurement of the time information of an event, provision of the global *gate* signal and prevention of further signal processing (*veto*), when any module is *busy*. Figure 3.15 shows the block diagram of the digital electronics. This part has been largely modified and simplified to avoid several digital effects.

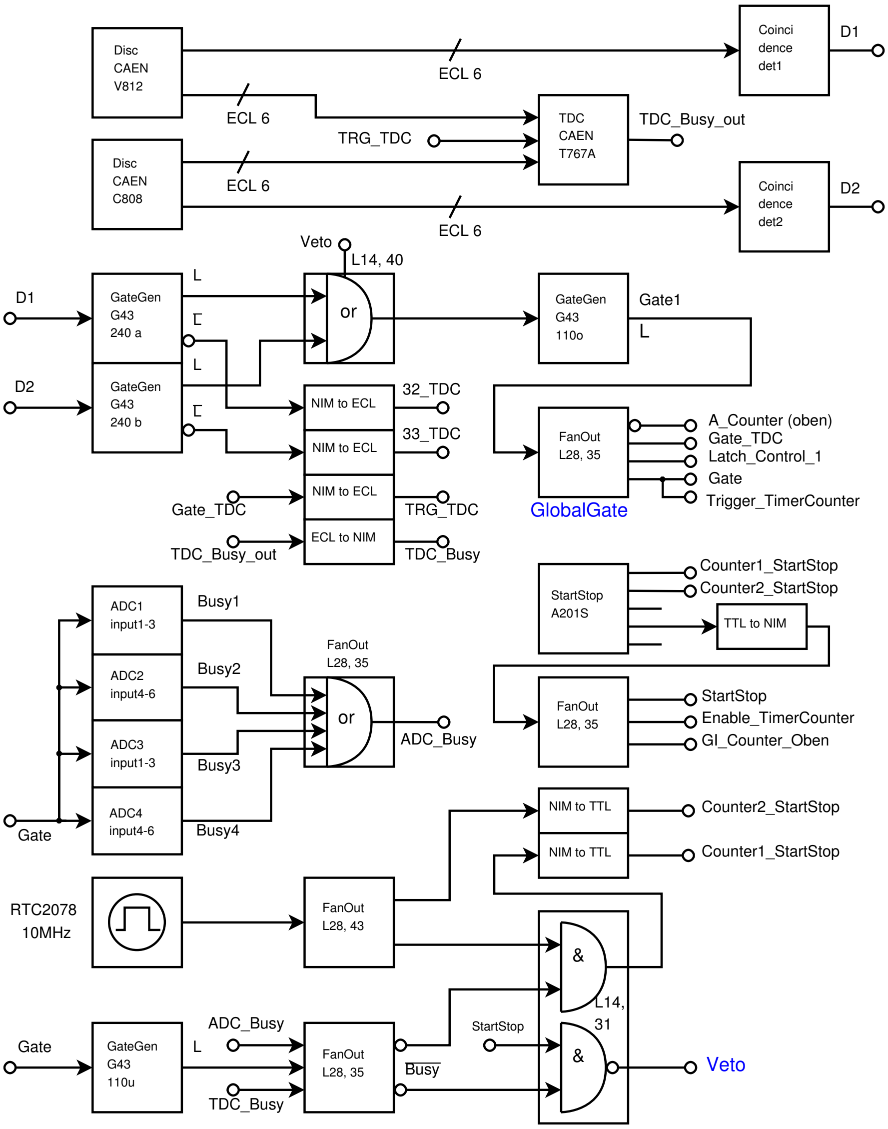

Figure 3.15: Digital part of the electronics. The upper section describes the generation and procession of the *gate* signal, whereas the *veto* logic is shown in the lower part. The *gate* is triggered by incidences on the detectors, *veto* inhibits this, when the system is *busy*, e.g. due to read–out of the data.

The system provides several time information. The first one is realized by using a 10 MHz clock (⇒ 100 ns resolution) for precise determination of the deadtime (see section 5.5). During each 10 s measurement cycle the clock signals of this time base are counted twice: raw and during the time, when the system is not *busy*, see lower part in schematic 3.15. The second time base, a 1 MHz clock, is located inside the *TimerCounter* modules and provides the incident time of an event with a resolution of 1 µs. A third time information with a resolution of 0.8 ns is given by the *TDC* (Time to Digital converter), that is mainly used to determine, which of the two detectors has triggered first.

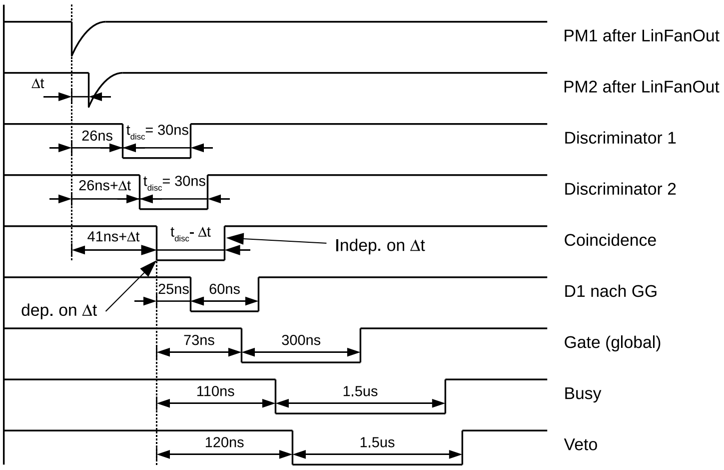

Figure 3.16: Timing diagram of the electronics for an exemplary event (not drawn to scale). When two of the six photomultiplier trigger their discriminators, the *coincidence* becomes TRUE. This opens the *gate*, energy and event time are measured and the system is *busy* for about 1.5 µs.

The two discriminators and the attached coincidence units select the incoming events according to their energy and the coincidence criterion. This criterion is that the signals of *two–of–six* photomultipliers are above the discriminator threshold – this *triggers* the system. The resulting *gate* signal has a fixed length of $t_{\text{gate}} = 300\,\text{ns}$, which means that it cannot be *re-triggered* by new events during the gate time. While *gate* is TRUE, all ADC modules measure the energy by integrating the incoming signal (details in section 3.6.3), whereas the corresponding time information is provided by the TimerCounters and the TDC. After an event is measured, the system has to recover. This is realized by adding an artificial deadtime, which is set to about $t_{\text{dead}} \approx 1.5\,\mu\text{s}$. Now the system is *busy* and stopped with the *veto* signal. After the deadtime the system is ready for detecting the next event.

Figure 3.16 shows the timing diagram in case an event triggers at least two discriminators of one detector. The reason for the necessity of using the 300 ns delay lines is visible: the *gate* signal, which initiates the ADC-internal integration of the photomultiplier signals, appears more than 110 ns later than the pulses on the LinearFanOuts due to several signal processing and propagation times.

3.6.3 Development of new ADC Modules

The eventrate of the Perkeo III continuous beam measurement in 2007 was about 50 kHz, which is two orders of magnitude above the rate of the last Perkeo II measurement. This high eventrate revealed a problem of the used ADCs: the measured energy of an event noticeably depended on the average eventrate but even stronger on the delta-time, which describes the time interval between the measured event and the predecessor.

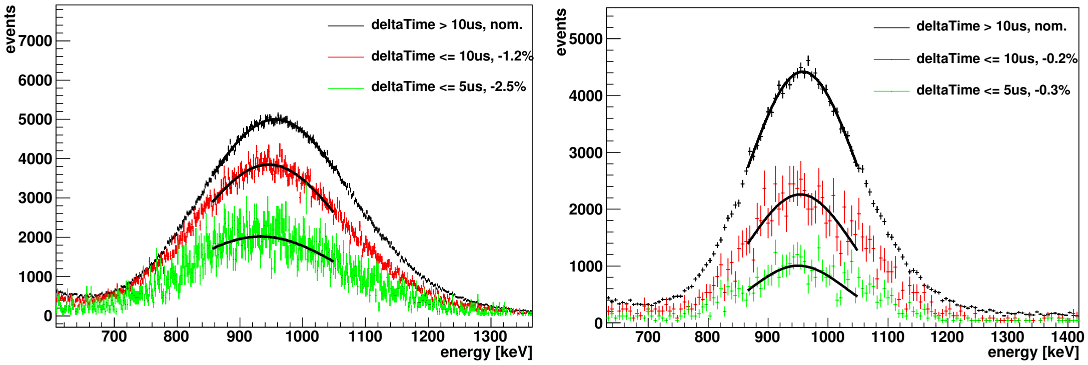

(a) ^{207}Bi measurement with previous ADCs. The peak shifts up to $-2.5\,\%$, depending on the delta-time.

(b) The same measurement with the new ADCs. Now the peak shifts only up to $-0.3\,\%$ of the nominal value.

Figure 3.17: Comparison of the rate dependence between the previous and the new ADCs. Both measurements were performed using the ^{207}Bi source. The green and red curves are scaled due to low statistics.

Delta-Time	Fraction of Events	Deviation of Energy	
		Previous ADCs	New ADCs
full	100 %		
$\Delta t > 10\,\mu s$	97 %	reference	reference
$\Delta t \leq 10\,\mu s$	3 %	-1.2 %	-0.2 %
$\Delta t \leq 5\,\mu s$	2 %	-2.5 %	-0.3 %

Table 3.3: Deviation of the measured energy vs. the chosen delta-time for previous and new ADCs.

Figure 3.17a shows this rate-dependence. In black, all events with a delta-time larger than 10 µs are taken as a reference. The spectra of events with a delta-time below 10 µs (green) and below 5 µs (red) show a shift to lower energies of $-1.2\,\%$ and $-2.5\,\%$. Table 3.3 presents the relative fractions of data in each of the three spectra together with the energy shifts.

Those event-time dependent energy shifts broaden the spectra to a certain degree, while this effect additionally depends on the average eventrate. That means the broadening effect is different for each calibration source or the neutron decay data. Therefore, during the preparation phase of the beamtime a new ADC was developed together with the electronic workshop of the Physical Institute in Heidelberg. Besides some general improvements in signal processing and buffering, the major focus was on:

- Decreased energy dependence on average eventrate and delta-time
- Improved energy resolution
- Enhanced suppression of ground-loops

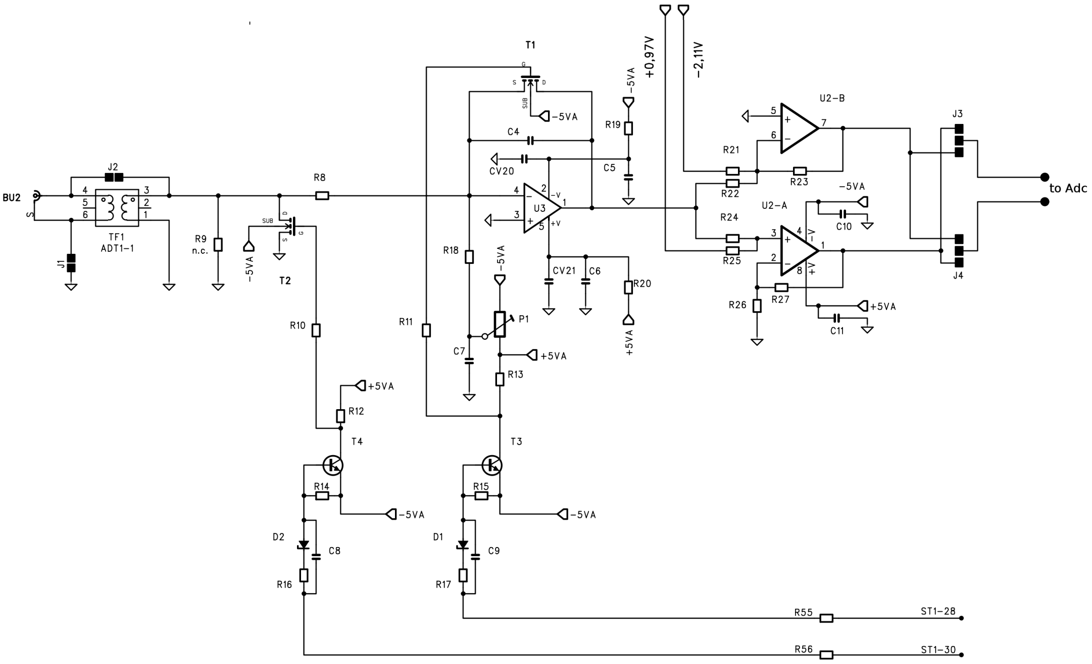

Figure 3.18: Schematic of the analog part of the new ADCs. On the left the incoming signal is coupled, the center part shows the signal processing and on the right the pedestal is added (see below). The lower switches are used to enable the integration on the capacitor C4 or to clear its charge after the analog–to–digital conversion [Rus08].

Figure 3.18 shows the analog part of the ADC schematic. One difference compared with the previous ADCs is the use of two separate switches to enable the integration of the energy and to clear the integrated charge (lower part). This allows an exactly matched and flexible switching of the respective

MOSFETs.[19] The improved ground-loop behavior was realized by using a transformer to couple the incoming signal. This component was only grounded at the secondary side, which results in a total suppression of the so-called common mode ripples.

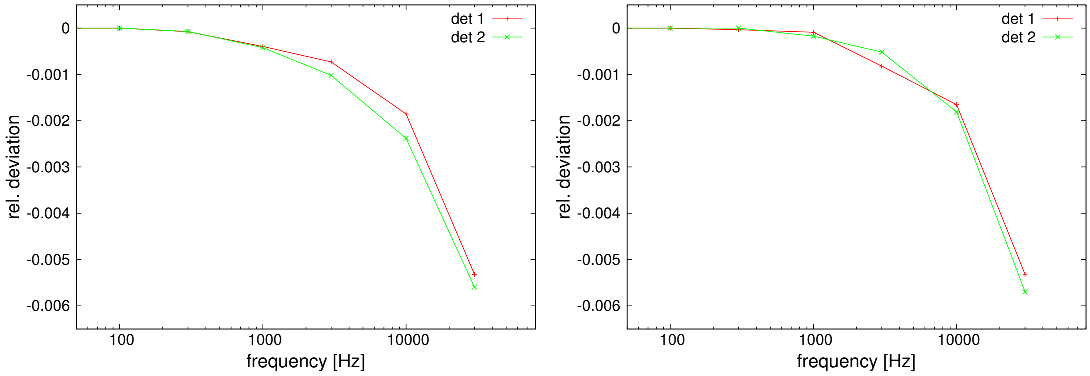

Figure 3.19: Relative deviation of the measured signal as function of the frequency of generated test pulses. The measurement was done with pulses equivalent to electron energies of 400 keV (left) and 1 MeV (right).

A number of test and analysis were performed with the new ADCs before and during the beamtime (differential and integral linearity tests, temperature behavior, ...). Three of them are described in this thesis. The dependence of measured energy on average rate is shown in fig. 3.19. This analysis was done using a test pulse generator and measuring the energy peaks as function of the average rate for different pulse heights to simulate different energies. The pulse heights in the two plots correspond to the energies of ^{113}Sn ($\approx 400\,\text{keV}$) and the upper ^{207}Bi peak ($\approx 1\,\text{MeV}$). The dependence of measured energy is about $1 \cdot 10^{-3}$ for the expected eventrate of the neutron decay ($R \approx 2\,\text{kHz}$) and rises to $5 \cdot 10^{-3}$ for rates of 30 kHz. The dependence on the delta-time is shown in fig. 3.17b and table 3.3. Now the delta-time dependent energy shifts are about one order of magnitude smaller compared with the previous ADCs.

The pedestal analysis is described in more detail, since the previous ADCs revealed some severe problems on this issue.

Pedestal

Each measured signal has a certain width of energy distribution, even a signal of $E = 0\,\text{keV}$, at least due to thermal noise. An ADC measures the applied energy or voltage and converts it to a digital number in units of channels *ch*.

---

[19] MOSFET: Metal Oxide Semiconductor Field Effect Transistor.

The resulting spectrum runs from channel 0 to $2^d - 1$, where d denotes the resolution of the ADC. When an ADC would project an energy of 0 keV to channel 0, half of the distribution with $E < 0$ would be cut out. To avoid this, an ADC adds an offset to the measured signal, the so-called *pedestal*: energy in channels which corresponds to 0 keV.

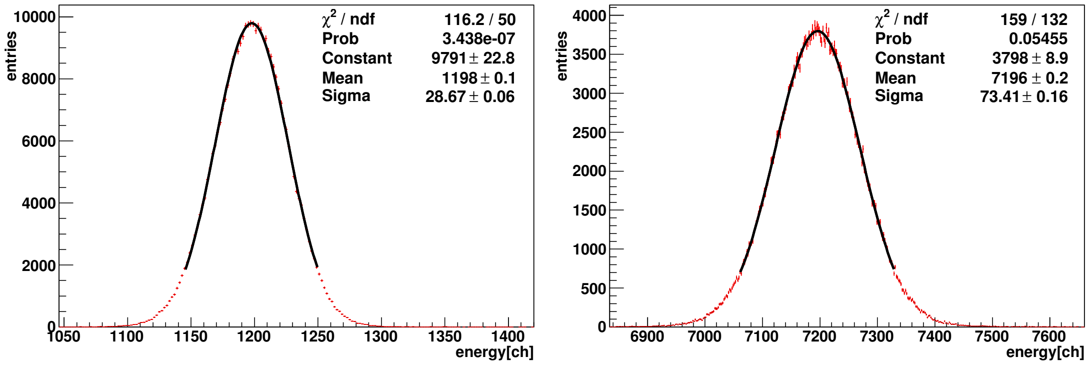

(a) Pedestal of a single ADC. The shape follows nicely the Gaussian fit. The width $\sigma_s \approx 29$ ch corresponds to about 0.9 keV.

(b) Pedestal of the detector (sum of six ADCs). The width $\sigma_{\mathrm{det}} \approx 73$ ch matches the expected value of $\sqrt{6} \cdot \sigma_s \approx 71$ ch $\widehat{=}$ 2.3 keV.

Figure 3.20: Pedestal of a single ADC (left) and the detector sum (right) in red. Both shapes follow decently the black Gaussian fits.

The width of a measured zero-signal is mainly influenced by electronic noise (from photomultiplier, preamplifier and ADC), thus a Gaussian distribution is expected. Figure 3.20 shows the measured pedestals of the new ADCs. Both curves, single ADC (left) and detector sum (right), nicely follow an expected Gaussian distribution.

Detailed pedestal analysis of the 2009 data showed that the peak position as well as the width of the pedestal remained perfectly stable.[20] Figure 3.21 shows the pedestal peak position for both detector sums during a period of about 12 days. Two times per day a dip of the order of 1 keV is visible in both curves, which corresponds to measurements with the radioactive source ^{137}Cs. This source had a much higher event rate compared to the other radioactive sources or the electrons from neutron decay: $r_{\mathrm{Cs}} \approx 33$ kHz vs. $r_{\mathrm{el}} \approx 2$ kHz, see table 3.2.

---

[20] This was one of the major problems with the previous ADCs during the 2007 beamtime [Kap07, Fri08].

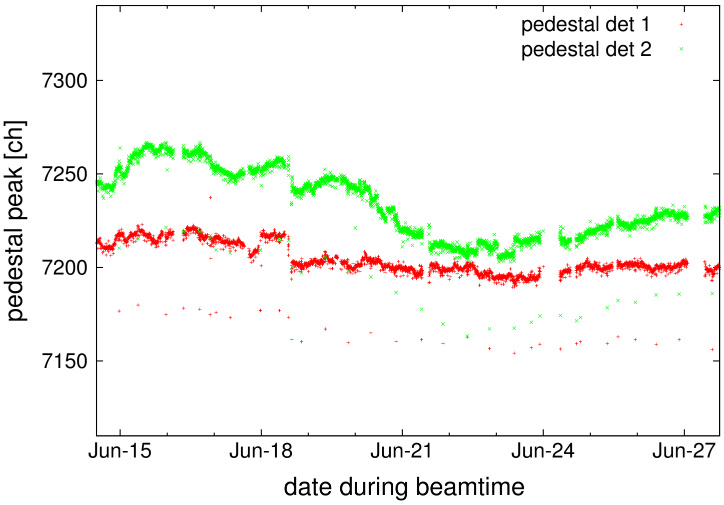

Figure 3.21: Pedestal peak for both detectors as function of time. The single dips (about 2–3 times per day) correspond to the pedestal measurements of the source ^{137}Cs, which had a much higher event rate than the other radioactive sources or the electrons from neutron decay: $r_{\mathrm{Cs}} \approx 33\,\mathrm{kHz}$ vs. $r_{\mathrm{el}} \approx 2\,\mathrm{kHz}$. The resulting change of the pedestal peak corresponds to an energy of about 1 keV.

Chapter 4

Beamtime 2008/09 – Assembly of PERKEO III and Measurements

The measurement campaign was from November 2008 to August 2009. The reactor cycles at the ILL last about 50 days due to the burn-up of the fuel-rods, which are exchanged during a subsequent 14 day beam break. Neutrons were available for about 140 days of the beamtime. In this time e.g. the spatial and time dependent properties of the pulsed neutron beam were analyzed, polarization $\mathcal{P}$ was measured and neutron decay data were taken. During the beam breaks the experiment was assembled and further optimized.

4.1 Assembly of the Experimental Setup

First, the beamline including spinflipper, collimation system with five apertures and magnetic holding field system were assembled (see section 3.2). The entrance window was placed close to the exit of the polarizer. The horizontal and vertical alignment of the beamline was done using a laser system and a theodolite.[1] It was adjusted after the assembly of each aperture, followed by an analysis of the beam profile, utilizing the activation of copper-foils, see section 4.2.1.

Next, the chopper was installed to the beamline. Since the rotating disc has to withstand very high forces and accelerations (see section 3.4), a special guard was constructed and implemented to protect the exterior parts in case of a breakage.

---

[1] A theodolite is useful in precision measurements of angles in the horizontal and vertical planes. The achievable precision of a theodolite is in the order of seconds of arc, see e.g. http://www.deutsches-museum.de/.../praezisions-theodolit/.

The spectrometer PERKEO III with an already assembled detector system was lifted into the pit of PF1B and connected to the beamline and the chopper. Since the light guides of detector 2 were slightly scratched, they were reworked. This resulted in a higher light yield on this detector compared with detector 1, see section 5.1.1. The calibration scanner and the beamstop were installed inside the spectrometer together with some additional internal lead shielding. External lead and boron shielding was added to all reasonable locations, see e.g. section 4.4.2.

Then, the electrical power supply of the solenoids and correction coils, the vacuum pumps, the cooling system, the data acquisition system and the monitoring system were installed. The latter observed the water reflux of all closed cooling circuits and was able to switch off the electrical power supply in case of an incident.

Finally, the detectors were put into operation. Since the internal current amplification of the photomultipliers increases exponentially with the applied high-voltage, the adjustment was performed very carefully. In this way, the position dependent detector response was significantly improved compared to the 2007 beamtime (see section 5.1.2).

4.2 Characterization of the Pulsed Neutron Beam

The neutron beam coming from the polarizer has a certain spatial profile, which is modified by the collimation system. In addition, the flux is time dependent when the neutron beam is pulsed. These properties were carefully characterized during the beamtime.

4.2.1 Spatial Beam Profile

The neutron beam profile was measured using copper foil activations. A foil ($d \approx 0.2\,\mathrm{mm}$) of natural copper (69.2 % of ^{63}Cu and 30.8 % of ^{65}Cu) was placed inside the spectrometer at different longitudinal positions (e.g. close to the beamstop) and activated with the neutron beam. After the activation time of about 30 min and a subsequent decay time of another 25 min (activated ^{66}Cu has a half-life of $t_{1/2} = 5.1\,\mathrm{min}$, see appendix B.6), the beam profile was read out by a 2-dimensional intensity scan after the transfer to an image plate, see [Kre04].

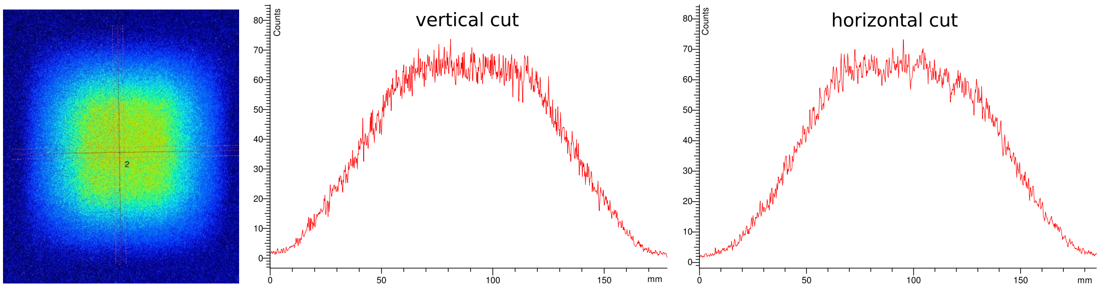

Figure 4.1: 2-dimensional intensity scan of the activated copper foil (left) together with vertical and horizontal cuts through the 2D beam profile.

The plots in fig. 4.1 show a 2D scan of the neutron beam profile together with vertical and horizontal cuts. The FWHM width and height of the profile close to the beamstop are:

$$w \cong 90\,\text{mm} \quad \text{and} \quad h \cong 90\,\text{mm}\,. \tag{4.1}$$

This rather symmetric beam profile serves as input for correction calculations of the magnetic mirror effect, see eq. (3.33).

4.2.2 Time Dependent Structure of the Neutron Pulse

To analyze the time dependence of the neutron pulse, two aluminum plates were mounted inside the decay volume at the symmetric points:

$$z_1 = z_0 - 1.0\,\text{m} \quad \text{and} \quad z_2 = z_0 + 1.0\,\text{m}\,,$$

where z_0 denotes the center of the decay volume. Close to these plates two NaI-detectors were placed outside the spectrometer. They were used to detect the γ-radiation, which was created when neutrons of the pulse hit the aluminum plates. Figure 4.2 presents the two resulting time of flight spectra, which show the shape and dispersion of the neutron pulse. Several properties can be derived:

$$v_\text{m} = \frac{z_2 - z_1}{t_2 - t_1} \approx \frac{2.0(1)\,\text{m}}{(6.2(1) - 3.3(1))\,\text{ms}} \approx 690(40)\,\text{m/s}\,, \tag{4.2}$$

$$\lambda_\text{m} = \frac{h}{m_\text{n} \cdot v_\text{m}} \approx 5.7(4)\,\text{Å}\,, \tag{4.3}$$

$$
\begin{aligned}
re &= \frac{\text{expansion of pulse}}{\text{time of flight}} = \frac{\Delta t_2 - \Delta t_1}{t_2 - t_1} \\
&= \frac{0.25(10)}{2.9(1)} = 8.6(3.4) \cdot 10^{-2} \,, \qquad (4.4)
\end{aligned}
$$

with $t_{1,2}$ denoting the peak positions in the respective spectra and $\Delta t_{1,2}$ the width of the peaks at about 10 % of the height. The value of λ_m confirms the selected wavelength of $\lambda \cong 5.5\,\text{Å}$, since the velocity selector was running at 23155 rpm. The relative expansion *re* is a measure for the velocity or wavelength distribution in the neutron pulse. This is expected to be 10 % of the nominal value, according to the specification of the velocity selector, see section 3.1.2.

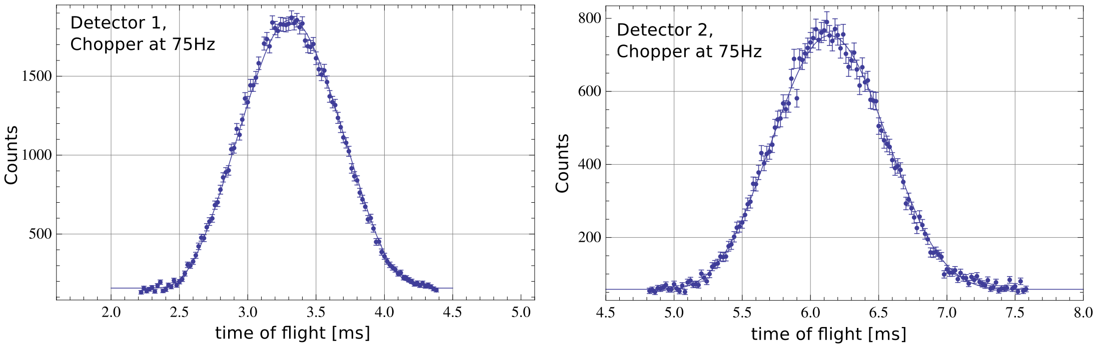

Figure 4.2: Time of flight spectra, measured with the two aluminum foils in the decay volume at symmetric positions: $z_1 = z_0 - 1.0\,\mathrm{m}$ and $z_2 = z_0 + 1.0\,\mathrm{m}$, with z_0 as center point of the decay volume [Wer09]. With a chopper frequency of 75 Hz, the pulse widths at about 10 % of the height are: $\Delta t_1 \approx 0.85(5)\,\mathrm{ms}$ and $\Delta t_2 \approx 1.10(5)\,\mathrm{ms}$.

The determination of the pulse shape within the decay volume is essential for the magnetic mirror correction, see eq. (3.33).

4.3 Timing of the Asymmetry Measurement

The measurement of the neutron decay data followed this procedure:

- Twice per day a full detector calibration using the sources ^{139}Ce, ^{113}Sn, ^{207}Bi and ^{137}Cs was performed. For this, the neutron beam was switched off manually.

- Once per hour the instrument shutter of the neutron beam was closed to measure the drift of the detection system, using one of the calibration sources, usually ^{113}Sn. This ran fully automated, controlled by the ILL control system *Nomad*, see section 3.6.1.
- Between two of these consecutive calibrations, neutron decay data were taken: 12 runs, each with 5 min of data.
- The polarization $\mathcal{P}$ was measured three times during the beamtime: at the beginning, at halftime and at the end.
- The magnetic field profile inside the decay volume was measured two times: once at 20 % of the nominal field and once at full field.
- Several systematic searches for time dependent background have been performed. For instance, the neutron decay measurement was interrupted for about four days. A ^{6}LiF plate was installed directly behind the chopper to prevent neutrons from entering the spectrometer, see analysis in section 5.3.2.

4.4 Characterization Measurements and Analysis

In addition to the neutron decay measurement, other properties were analyzed and measured. Some of them are briefly described in this section.

4.4.1 Magnetic Field Measurements

During the preparation phase for the beamtime, the magnetic field profile was measured, red curve in fig. 4.3. Two local minima in the decay volume are visible.

Because of the magnetic mirror effect (section 3.3.1), these minima must strictly be avoided, since local minima create small magnetic bottles and therefore destroy the asymmetry information of stored electrons. This was achieved by adding a number of correction coils on top of the solenoids of the decay volume, see green curve in fig. 4.3. Another benefit of this measure is the increase of the usable length in the decay volume by about +10 %.

At the end of the beamtime the measurement of the magnetic field profile was repeated with a high resolution in x-, y- and z-direction. On a $3\times3\times25$ grid a total volume of $20\times20\times250\,\mathrm{cm}^3$ was scanned. The obtained data are necessary

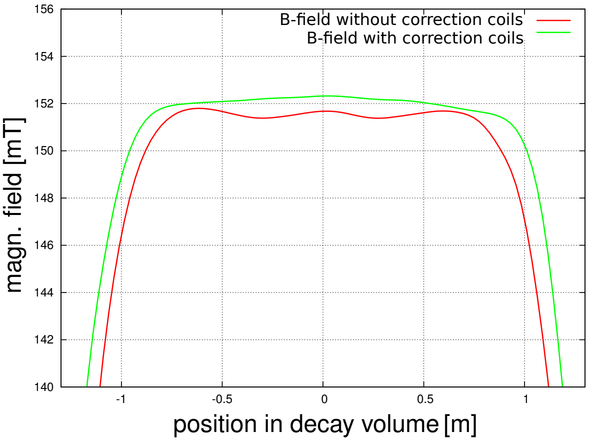

Figure 4.3: Profile of the magnetic field inside the decay volume with the center point at $z = 0$. The measured curve (red) shows two local minima, which were corrected with six correction coils (green). An additional benefit of this measure is the increased length of the homogeneous region in the decay volume [Wer09].

to calculate the systematic correction on the asymmetry A, coming from the magnetic mirror effect. The value of this correction is one of the three blinding quantities, see section 6.1.

4.4.2 Time Dependent Background from the Chopper

To determine the time dependent background from the chopper, the first analysis were performed without any shielding. A γ-detector was placed above the chopper housing and the radiation was measured, synchronized with the chopper period. Figure 4.4 shows the result of this measurement for different chopper frequencies. It is clearly seen that the time dependent structure is directly correlated to the phase angle of the chopper disc. Possible reasons are impurities in some of the ^{6}LiF tiles or adhesive residue from the gluing process. To eliminate this beam related time dependent structure, two shielding layers were placed directly above the chopper housing:

- 20 cm of boron plastic to moderate occurring fast neutrons coming from the chopper disc,
- 20 cm of lead to attenuate γ-radiation.

The result of this measure is an absence of any time dependent structure in the time of flight spectra, measured with the PERKEO III detectors, see right plot in fig. 4.4. The detailed analysis follows in section 5.3.

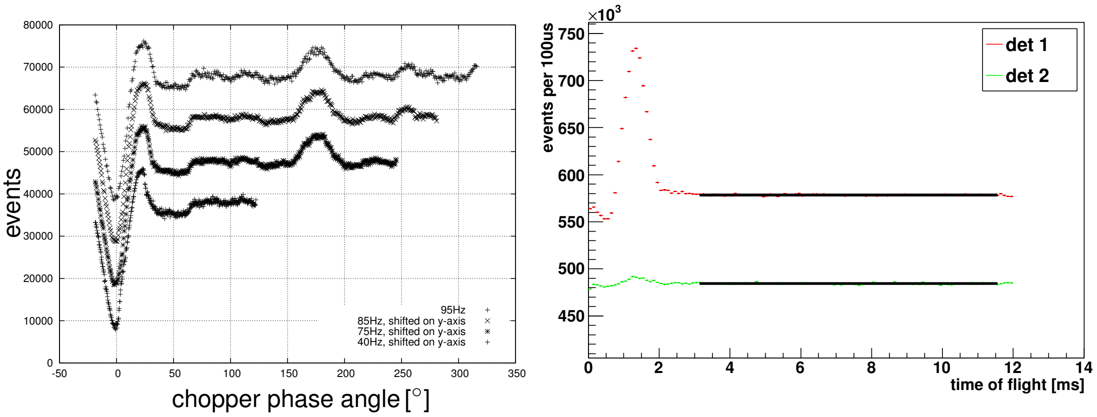

Figure 4.4: Left: Time structure of background events, produced by the chopper for different chopper frequencies, measured with a γ-detector on top of the chopper. The upper curve is measured directly, while the others are scaled on the time axis to fit the respective chopper angle of the first curve. The visible structure is clearly correlated with the angle, which means that either some of the ^{6}LiF tiles have impurities, or that the gluing process of these tiles did not work properly [Wer09]. **Right:** Time of flight spectra, measured with the PERKEO III detectors. In this measurement the ^{6}LiF beamstop was placed directly behind the chopper, see section 5.3.2.

4.4.3 Beamstop Optimization

The first beamstop test were performed with an already existing ^{6}LiF beamstop, which is optimal with respect to the absolute background level in continuous

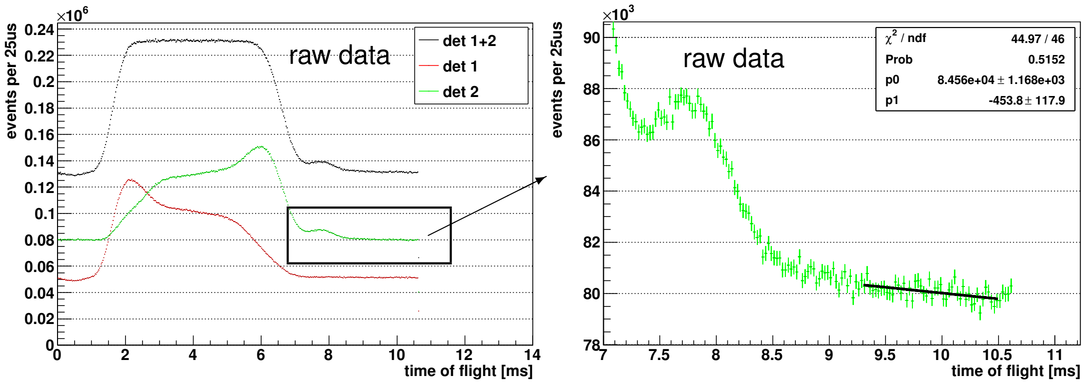

Figure 4.5: Time of flight spectra, measured with the ^{6}LiF beamstop. The data show a considerable negative slope in the background time window on detector 2, while the signal on detector 1 is flat. The slope is of the order $\mathcal{O}(5 \cdot 10^{-3})$, which is about one order of magnitude larger than what is obtained with the ^{10}B$_4$C beamstop (see section 5.3.1 and table 5.5).

beam measurements. This beamstop is made of the same type of ^{6}LiF tiles as used for the chopper disc. The first time of flight measurements showed an unexpected behavior: the ToF spectrum during the chosen background time window was not flat on detector 2, which was close to the beamstop. Instead of this, a relative negative slope of about $5 \cdot 10^{-3}$ per millisecond was observed. A background uncertainty would propagate to the uncertainty of the asymmetry coefficient A, scaled by the inverse of the signal to background ratio. Therefore the resulting error would be of the order $\mathcal{O}(1 \cdot 10^{-3})$, which is already close to the expected total uncertainty of A. Figure 4.5 shows the time of flight spectra on both detectors and the sum, as well as a zoom into the background window.

The effect is clearly related to the beamstop, since it was only visible in the time of flight spectrum of detector 2, while the spectrum of detector 1 was flat. As can be seen in table 3.1, the absorption of the neutrons in the ^{6}Li nuclei triggers secondary fast neutrons. To absorb these neutrons, several measures were taken, e.g. the inner face of the beam-stop tube was lined with boron. The achieved improvements were not sufficient, since the plots in fig. 4.5 show already the optimized setup.

Consequently the ^{6}LiF beamstop was replaced with an alternative. The new beamstop was made of enriched $^{10}B_4C$, which produces about 200 times less fast neutrons compared with ^{6}LiF, whereas the γ-rate is strongly increased. However, γ-radiation appears instantaneously and therefore a delayed and subsiding signal is not expected. The first ToF measurements with the new beamstop showed exactly the expected behavior: the delayed sloping structure was gone, while the counted number of events during the absorption of the neutron pulse noticeably increased, see section 5.2 and fig. 5.15.

4.4.4 Drift Measurement

The experimental hall *ILL 7* with the beam facility PF1B is not air-conditioned. Besides the temperature of the air, the water temperature of river *Drac*, used for cooling the reactor and the experiments, is not constant as well. Temperature variations up to 5 °C per day were measured at the heat-exchanger of the cooling system. Hence, temperature variations during one measurement day and during the whole beamtime have a non-negligible influence on the measured spectra.

The influence of the temperature changes as well as a possible degradation of the detection efficiency over time were quantified once per hour. For that, the asymmetry measurement was interrupted for about 5 min to measure the spectrum of a calibration source, e.g. ^{113}Sn with the energy peak at about 370 keV. This information was then used to re-calibrate the neutron decay data, see section 5.4.

Figure 4.6 shows an example of the drift on detector 1 and 2. To derive this curve, a simple Gaussian fit within the FWHM-range was done to the Sn-peak. The plot reveals that the effect is about twice as large on detector 1 compared to detector 2. To understand this and to reduce the effect on detector 1, an external water cooling system using copper tubes was assembled to the housing of detector 1. The temperature of the cooling water was stabilized, but nevertheless the effect did neither disappear nor change noticeably.

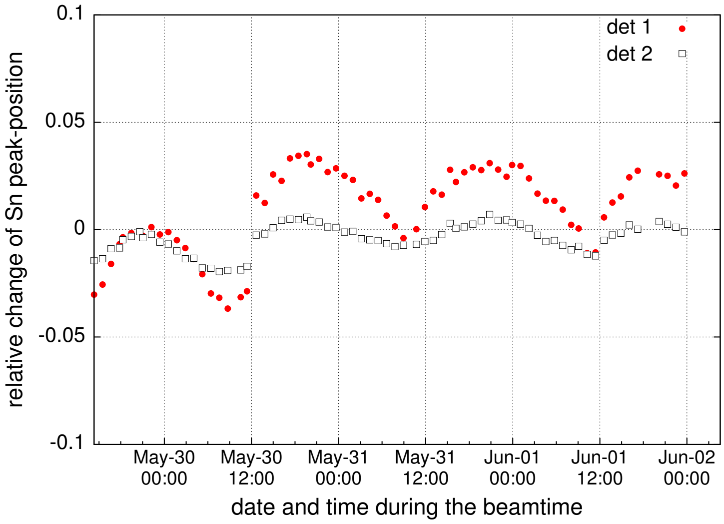

Figure 4.6: Normalized measured drift during a period of three days. The drift on detector 1 is twice as large as on detector 2 (det 1: ±3 %).

By excluding data of a single ADC from the detector-sum it was also tested, whether one of the six photomultipliers, LinearFanOuts or ADCs has a distinctive temperature problem – no peculiarities were found. Finally, the reason for having different drifts between detector 1 and detector 2 is still not understood, presumably the thermal coupling of the photomultipliers to the environment varies between the detectors. Despite of this, the consequence of the drift on the energy spectra is under control and can be corrected, see section 5.4.

4.4.5 Cross Talk on the Discriminator

At first it was planned to use the new discriminator V812 from CAEN for both detectors (2×6 input signals). At the beginning of the beamtime, a cross talk between the trigger signals of detector 1 and detector 2 was observed. This can be visualized using the backscatter curve, which represents the probability of a backscattered event as function of the flight time to the other detector. Positive flight times represent the flight of an electron from detector 1 to detector 2, while negative flight times correspond to the opposite flight direction, see fig. 4.7.

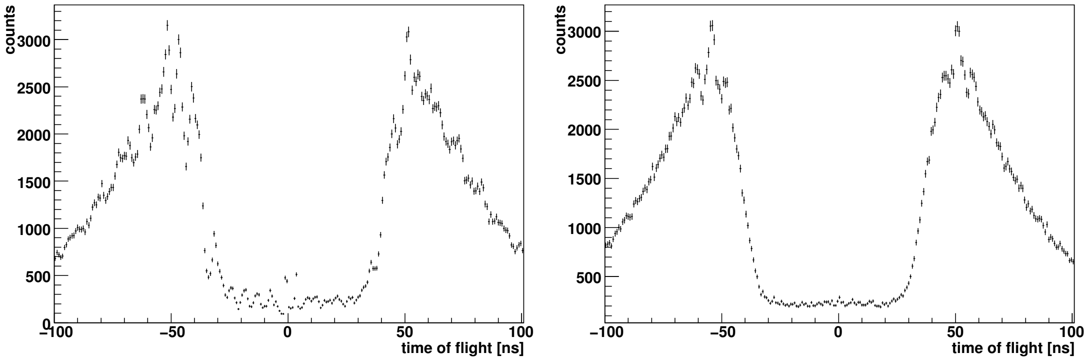

(a) Backscatter curve with only one discriminator for all 12 photomultipliers. A time structure is visible throughout the whole function. The ripples follow a $t \lesssim 10\,\mathrm{ns}$ periodicity.

(b) When using separate discriminators and coincidence units for the two detectors, the ripple structure (nearly) disappears. This shape now is comparable with previous PERKEO measurements.

Figure 4.7: Backscatter curve: flight time of backscattered events related to their initial events, before and after the improvement. Positive flight times represent the flight of from detector 1 to detector 2, negative the opposite flight direction.

This cross talk resulted in a ripple structure, which modulated the backscatter curve. A possible explanation for this structure was found during the analysis of the event timings with an oscilloscope. Figure 4.8 shows the analog signal of an event (measured at the LinearFanOut) together with its discriminator signal. About 6 ns before the specified discriminator signal, a short pulse (width $\leq 2\,\mathrm{ns}$) appeared sporadically, sometimes even without the specified signal. The frequency of its occurrence was correlated with the energy of the respective event and the general eventrate. This conspicuous behavior of the discriminator could only be minimized by using separate discriminators and coincidence units for the two detectors. Nevertheless, it does not influence the

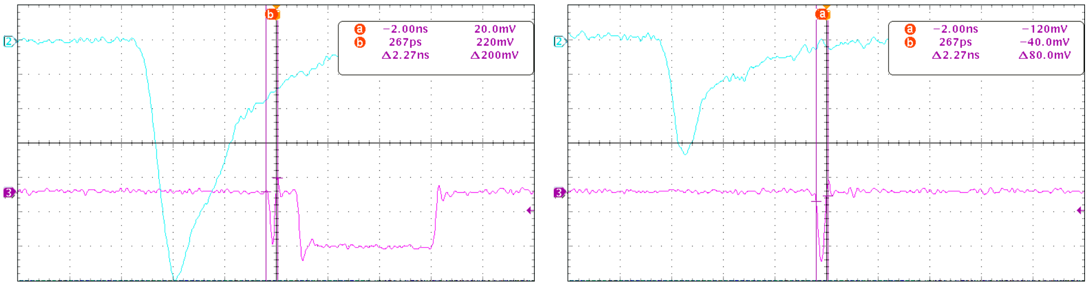

(a) Besides the specified discriminator signal (width: 25 ns), a second undefined short pulse appeared in about 5 % of the events.

(b) This undefined short pulse also appeared without the specified discriminator signal. The probability for this effect was of the order of 1 %.

Figure 4.8: Measured event in blue (left: 200 mV/div, right: 20 mV/div) with corresponding discriminator signal in purple (500 mV/div). The occurrence frequency of the short undefined pulse is correlated with the system eventrate and the energy of the respective event. Pictures taken with the oscilloscope DPO3054 from Tektronix. Time resolution: 10 ns/div.

β-asymmetry at all, since the assignment of the events to the detectors is not influenced.

Another observation was a sporadic occurrence of a jitter of the discriminator signal with respect to the input signal ($t_{\text{jitter}} \lesssim 10\,\text{ns}$). This effect is probably related to the short undefined pulse. The expected influence on the asymmetry data is negligible, since a jitter of 10 ns is too short to cause a faulty assignment of an event to the hemispheres:

$$t_{\text{min}} \geq \frac{\text{length of PERKEO III}}{\text{speed of light}} = \frac{8\,\text{m}}{3 \cdot 10^8\,\text{m/s}} \cong 27\,\text{ns}\,. \tag{4.5}$$

4.5 Total Number of Measured Decay Events

In table 4.1 an overview of the number of measured events during the beamtime is given. The total number of events is about seven times that of the last PERKEO II measurement [Mun06, Mär11a].

Chopper Freq.	Event Type	Detector 1	Detector 2	Sum
83 Hz	total number	$1.17 \cdot 10^9$	$1.57 \cdot 10^9$	$2.73 \cdot 10^9$
	signal	$2.62 \cdot 10^8$	$2.53 \cdot 10^8$	$5.15 \cdot 10^8$
	background	$1.37 \cdot 10^8$	$1.29 \cdot 10^8$	$2.66 \cdot 10^8$
	⇒ sig - bg	$1.25 \cdot 10^8$	$1.24 \cdot 10^8$	$2.49 \cdot 10^8$
94 Hz	total number	$1.26 \cdot 10^9$	$1.64 \cdot 10^9$	$2.90 \cdot 10^9$
	signal	$3.03 \cdot 10^8$	$2.87 \cdot 10^8$	$5.91 \cdot 10^8$
	background	$1.24 \cdot 10^8$	$1.11 \cdot 10^8$	$2.35 \cdot 10^8$
	⇒ sig - bg	$1.79 \cdot 10^8$	$1.76 \cdot 10^8$	$3.55 \cdot 10^8$
sum	total number	$2.42 \cdot 10^9$	$3.20 \cdot 10^9$	$5.63 \cdot 10^9$
	signal	$5.65 \cdot 10^8$	$5.40 \cdot 10^8$	$1.11 \cdot 10^9$
	background	$2.61 \cdot 10^8$	$2.40 \cdot 10^8$	$5.01 \cdot 10^8$
	⇒ sig - bg	$3.04 \cdot 10^8$	$3.00 \cdot 10^8$	$6.04 \cdot 10^8$

Table 4.1: Overview of the number of measured events during the beamtime. These are raw numbers without an energy cut. Signal and background (see definitions in eq. (5.1)) specify the number of events with respect to their time of flight, see section 5.2. The 83 Hz and 94 Hz datasets have approximately the same size. The final number of events used in the evaluation of the asymmetry A is $6 \cdot 10^8$.

A total fraction of 96 % of all measured neutron decay data was finally used to derive the asymmetry A. About 4 % of the data had to be omitted due to problems with the calibration scanner or spinflipper.

Chapter 5

Data analysis
Derivation of the β-Asymmetry

In this chapter the derivation of the various measurement results is described. The first part explains the measured characteristic properties of the electron detection system. Another major part addresses the effect of background events on the spectra. Later the influence of detector drift as well as the effect of the deadtime are discussed. Finally the derivation of the correlation coefficient A is presented by fitting the experimental asymmetry.

For all of the presented systematic and statistical effects uncertainty estimations on the final value of asymmetry A is given.

If not stated otherwise, the following definitions are used, where the vertical arrows refer to the neutron spin:

$$\begin{aligned} S^{\uparrow,\downarrow} &= \text{spectra during the signal time window} \\ B^{\uparrow,\downarrow} &= \text{spectra during the background time window, } B = B^{\uparrow} + B^{\downarrow} \\ r &= \text{ratio of signal time window to background time window} \\ N^{\uparrow,\downarrow} &= S^{\uparrow,\downarrow} - r \cdot B^{\uparrow,\downarrow} = \text{background subtracted signal spectra} \\ A_{\text{exp}} &\equiv \frac{N^{\uparrow} - N^{\downarrow}}{N^{\uparrow} + N^{\downarrow}} \overset{B^{\uparrow}=B^{\downarrow}}{\equiv} \frac{S^{\uparrow} - S^{\downarrow}}{S^{\uparrow} + S^{\downarrow} - r \cdot B} \equiv \frac{\text{diff}(E)}{\text{sum}(E)} \end{aligned} \tag{5.1}$$

5.1 Properties of the Electron Detector

The electron detection system consists of two plastic scintillators with six photomultipliers each (section 3.3.2), the discriminators with attached coincidence units (section 3.6.2) and finally the ADC modules. The energy deposition in the detector is triggered, if *two–of–six* (coincidence criterion) photomultipliers measure an energy above the chosen discriminator threshold (section 5.1.3).

There is a certain probability that the energy of an electron is not fully deposited in a detector but the particle is backscattered and finally arrives at either the same or the opposite detector (section 5.1.4). Another part of this chapter addresses the position dependence of the detector response, which is further optimized (section 5.1.2). This section starts with the determination of the detector linearity.

5.1.1 Detector Calibration – Linearity of the Detector Response

The linearity of a detection system is very important, since the asymmetry A finally is derived by fitting the experimental data measured in channels to a theoretical function initially given in units of keV. The simple linear approach to describe the energy to channel relation is:

$$CH(E) = g \cdot E + O\,, \tag{5.2}$$

with O and g denoting offset and a constant gain. To analyze and quantify the expected non-linearity of the detectors at low energies, the following test was applied.

Derivation of Non-Linearity of the Detectors

Using eq. (5.2) and assuming an energy dependent gain $g = g(E)$, two energetically adjacent peaks of the different calibration sources were fitted simultaneously using the tool *p3fit* (see section 3.5) with two free parameters offset O and gain g. In addition to the peaks coming from the electron capture decay of the different sources, the pure Auger peaks of ^{113}Sn and ^{207}Bi were also used in this analysis, since they are below 100 keV.

Table 5.1 shows the results of the 2-peak fits. As a reference, the peaks of ^{113}Sn, ^{137}Cs and ^{207}Bi (two peaks) were fitted simultaneously (4-peak fit, last line in the table). In fig. 5.1 the values for gain including the errors are plotted together with two fitfunctions, using an exponential and a sinusoidal non-linear approach:

$$gain_{\mathrm{exp}}(E) = g_0 + (g - g_0) \cdot (1 - \mathrm{e}^{-E/E_{\mathrm{th}}}) \quad \text{and} \tag{5.3}$$

$$gain_{\mathrm{sin}}(E) = \begin{cases} g_0 + (g - g_0) \cdot \sin\left(\frac{\pi}{2}\frac{E}{E_{\mathrm{th}}}\right) & \text{for} \quad E < E_{\mathrm{th}} \\ g & \text{for} \quad E \geq E_{\mathrm{th}} \end{cases}, \tag{5.4}$$

Fit from	Fit to	Gain [ch/keV]	Error on Gain [ch/keV]	Offset [ch]	Error on Offset [ch]
Aug Sn	Aug Bi	0.281	0.022	-4.33	1.35
Aug Bi	Ce	0.281	0.013	-3.70	0.49
Ce	Sn	0.310	0.003	-8.06	0.19
Sn	Bi Low	0.321	0.005	-10.04	0.62
Bi Low	Cs	0.322	0.005	-8.73	0.95
Cs	Bi High	0.326	0.005	-13.94	0.48
Full Calibration		0.326	0.002	-12.55	0.17

Table 5.1: Derived values for offset O and gain g from the fits to two energetically adjacent calibration peaks.

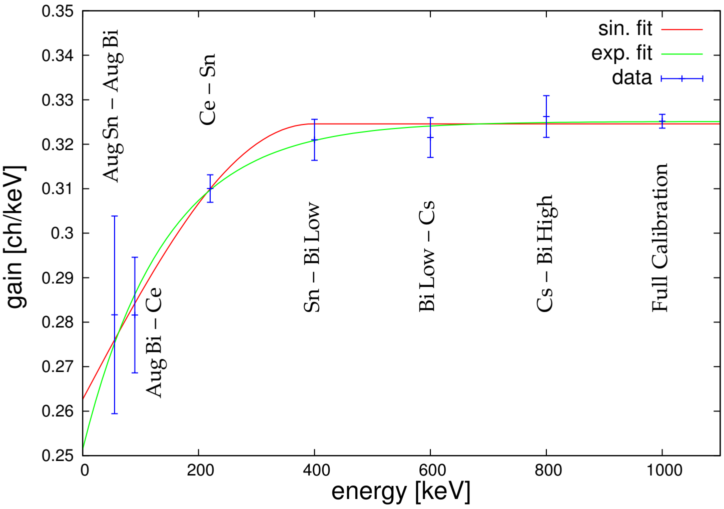

Figure 5.1: Energy dependent gain of the detector, derived using the 2-peak fits. Two energetically adjacent peaks are used to derive a local energy dependent gain $g(E)$, see eq. (5.2). The derived parameters of the exponential and the sinusoidal fits are listed in table 5.2, see also eq. (5.3) and (5.4).

with g_0 denoting the gain at $E = 0$ and E_{th} an energy threshold. Both approaches are continuous and continuously differentiable. The fit results are listed in table 5.2.

These two non-linear approaches were also used to perform a simultaneous fit to all available calibration peaks with three free parameters: gain g, offset O

Approach	Gain g [ch/keV]	Start Gain g_0 [ch/keV]	Energy Threshold E_{th} [keV]
exp	0.325	0.252	141
sin	0.325	0.263	397

Table 5.2: Derived values for gain g, start gain g_0 and energy threshold E_{th} from the exponential and the sinusoidal fit to the 2-peak data in fig. 5.1.

and energy threshold E_{th}, see e.g. fig. 3.12. The resulting reduced χ^2 values are:

$$\chi^2_{\text{exp}} = 1.4 \quad \text{and} \quad \chi^2_{\text{sin}} = 2.0\,. \tag{5.5}$$

The exponential approach describes the calibration data more accurate according to the derived χ^2 values. The detector function of the exponential approach is obtained by integrating eq. (5.3), using the boundary conditions $CH(E{=}0) = 0$ and $CH(E \gg E_{\text{th}}) = g \cdot E + O$:

$$CH(E) = g \cdot E + O \cdot \left(1 - \mathrm{e}^{-E/E_{\text{th}}}\right) \quad \text{with} \tag{5.6}$$

$$O = E_{\text{th}} \cdot (g_0 - g) < 0\,. \tag{5.7}$$

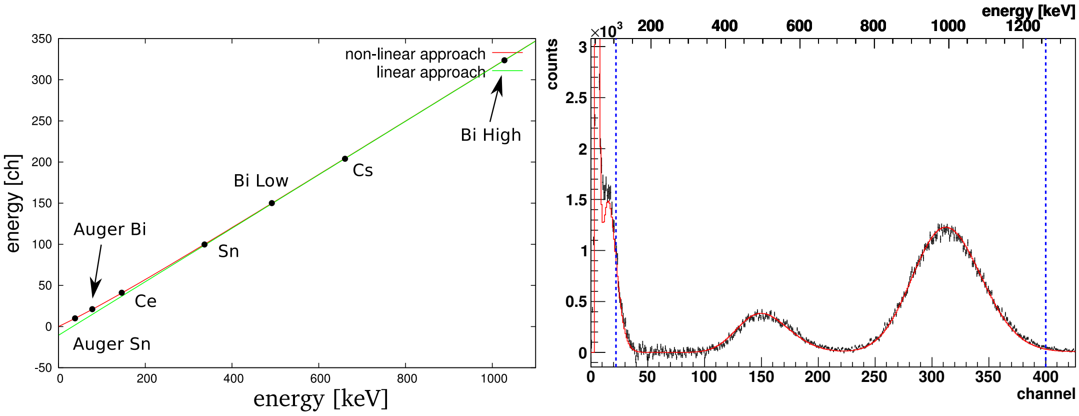

(a) Energy to channel relation for linear and exponential approach together with the approximate peak positions of the used calibration sources.

(b) With enabled exponential approach of eq. (5.6), the theoretical description of the ^{207}Bi source (red) fits over a broad energy range with reduced χ^2 of 1.5.

Figure 5.2: Energy to channel relation and fit to ^{207}Bi with enabled exponential non-linear approach.

This non-linear energy to channel relation and the linear approach from eq. (5.2) are displayed in fig. 5.2a together with position marks of the calibration peaks. A deviation from linearity is only visible for energies below about 200 keV. Figure 5.2b shows a broad fit to the ^{207}Bi spectrum with exponential non-linearity enabled. The data can be described to energies noticeably below 200 keV. The underlying physical explanation of the detector non-linearity is discussed now.

Monte Carlo Simulation

Several properties of the electron transport in an organic scintillator and the backscatter probability can be simulated with the Monte Carlo tool CASINO.[1]

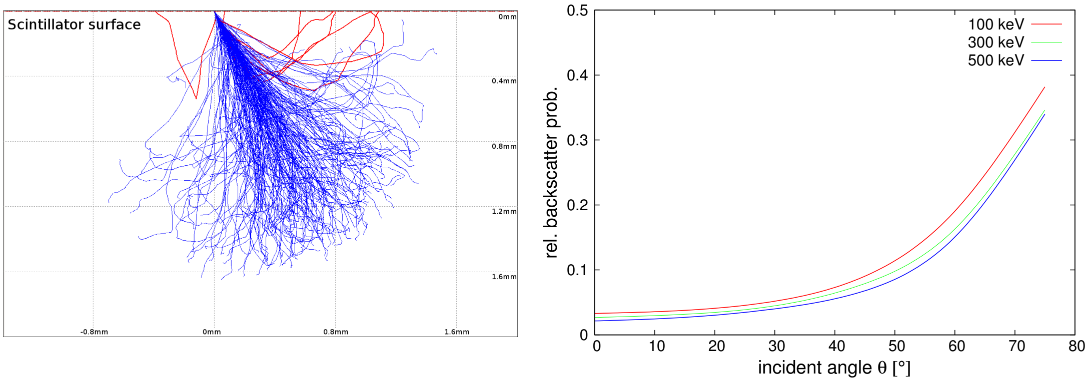

Figure 5.3: Results from analysis with the Monte Carlo tool CASINO. **Left:** electron trajectory inside the scintillator, with the upper edge as incident surface. In blue, electrons which deposit all energy inside the material, whereas the red trajectories symbolize particles, which are backscattered. The chosen energy and incident angle are: $E = 500$ keV, $\theta = 30°$. The electron track length is about 1.6 mm. **Right:** derived backscatter probability as function of energy and incident angle. The energy dependence is weak, while at about $\theta \approx 50°$ the backscatter probability is already 10 %. The derived probabilities are in absolute agreement with [Wie05].

The left plot in fig. 5.3 shows the simulated trajectories of incident electrons inside the scintillator. The red trajectories represent those particles, which do not deposit their energy completely, but are reflected. The backscatter coefficient as function of energy and incident angle θ is shown in the right plot. The results are in good agreement with those shown in [Mar03] or [Wie05], derived with other Monte Carlo tools.

---

[1] The Monte Carlo tool CASINO has been invented by the research team at Université de Sherbrooke, Québec, Canada.

The tool CASINO is used to derive the functional dependence of the electron track length on the energy. The result is:

$$x(E) = k \cdot E^{y} \, , \tag{5.8}$$

with k denoting an ionization property of an electron in the scintillator and energy E given in keV. The two parameters were found by fitting the results of the simulations for an energy range of 50–1000 keV:

$$y \cong 1.58 \quad \text{and} \quad k \cong 80\,\mathrm{nm} \, . \tag{5.9}$$

These results were used as input parameters in a semi-empirical non-linear model, which is described now.

Birks Model

The response of a scintillator is a function of the type of the incident particle, the respective energy and the specific ionization properties. As described above, the organic scintillator BC400 shows a non-linear response below about 200 keV. This behavior is known for electrons in organic materials. The first semi-empirical explanation by [Bir52, Bir64] defines the following differential response functions:

$$\frac{\mathrm{d}L}{\mathrm{d}x} = L_0 \cdot \frac{\frac{\mathrm{d}E}{\mathrm{d}x}}{1 + k_B \frac{\mathrm{d}E}{\mathrm{d}x}} \quad \Rightarrow \tag{5.10}$$

$$\frac{\mathrm{d}L}{\mathrm{d}E} = L_0 \cdot \frac{1}{1 + k_B \frac{\mathrm{d}E}{\mathrm{d}x}} \, , \tag{5.11}$$

with k_B denoting the *Birks* constant, L_0 a luminosity scaling constant and $\mathrm{d}E/\,\mathrm{d}x$ the energy loss:

$$\frac{\mathrm{d}E}{\mathrm{d}x} = \frac{\mathrm{d}E}{\mathrm{d}t} \cdot \frac{\mathrm{d}t}{\mathrm{d}x} = \frac{\mathrm{d}E}{\mathrm{d}t} \cdot \frac{1}{v(E)} \, . \tag{5.12}$$

The underlying assumption in the Birks Model is that a large energy loss (small velocity v, see eq. (5.12)) produces high local densities of excited molecule states. This increase of local ionization power leads to the so-called quenching interaction and a suppression of excitation, see denominator in eq. (5.11).

From eq. (5.8) the differential energy loss $\mathrm{d}E/\mathrm{d}x$ can be derived:

$$x(E) = k \cdot E^{y} \quad \Rightarrow \quad \frac{\mathrm{d}E}{\mathrm{d}x} = \frac{1}{k \cdot y \cdot E^{y-1}} \quad \text{with } y > 1\,, \tag{5.13}$$

where k describes the ionization property. Now the response function $L(E)$, which corresponds to the measured function $CH(E)$, follows by integration:

$$\begin{aligned} L(E) &= \int \frac{\mathrm{d}L}{\mathrm{d}E}\,\mathrm{d}E = \int L_0 \cdot \frac{1}{1 + \frac{k_B}{k} \cdot \frac{1}{y\,E^{y-1}}}\,\mathrm{d}E \\ &= E \cdot L_0 \left(1 - {}_2F_1 \left[1, \frac{1}{y-1}, \frac{y}{y-1}, -\frac{k\,y\,E^{y-1}}{k_B} \right] \right) . \end{aligned} \tag{5.14}$$

The hypergeometric function ${}_2F_1(a, b(y), c(y), f(E,y))$ is only solvable in closed form for some selected values of y. Two possible solutions for values of y close to the empirically derived value $y = 1.58$ (see eq. (5.9)) are:

$$L_1(E) = L_0 \left(E - \frac{9k_B}{8k} E^{\frac{2}{3}} + \frac{27k_B^2}{16k^2} E^{\frac{1}{3}} - \frac{81\,k_B^3}{64\,k^3} \ln\left[4k\,E^{\frac{1}{3}} + 3\,k_B \right] \right), \quad y = \frac{4}{3} \tag{5.15}$$

$$L_2(E) = L_0 \left(E - \frac{9k_B}{5k} E^{\frac{1}{3}} + \sqrt{\frac{243}{125} \frac{k_B^3}{k^3}} \cdot \arctan\left[\frac{5}{3} \frac{k}{k_B} E^{\frac{1}{3}} \right] \right), \qquad y = \frac{5}{3}\,. \tag{5.16}$$

Both solutions were implemented in the fitprogram *p3fit*, tested and compared with the sinusoidal and exponential approaches by fitting all available calibration peaks simultaneously. The results are listed in the following table.

Non-linear Model	χ^2 **/ ndf**
sinusoidal	2.0
exponential	1.4
Birks L_1	2.0
Birks L_2	1.7

The derived values for the Birks constant k_B are close to the expected value of the plastic scintillator BC400 [NI10]:

$$k_B \approx 100\,\frac{\text{nm}}{\text{keV}}\,, \tag{5.17}$$

while the ionization constant k deviates from the empirically derived value in eq. (5.9) by about a factor of two. The plot in fig. 5.4 presents the energy dependent gain $\mathrm{d}L(E)/\,\mathrm{d}E$ of the four analyzed non-linear approaches.

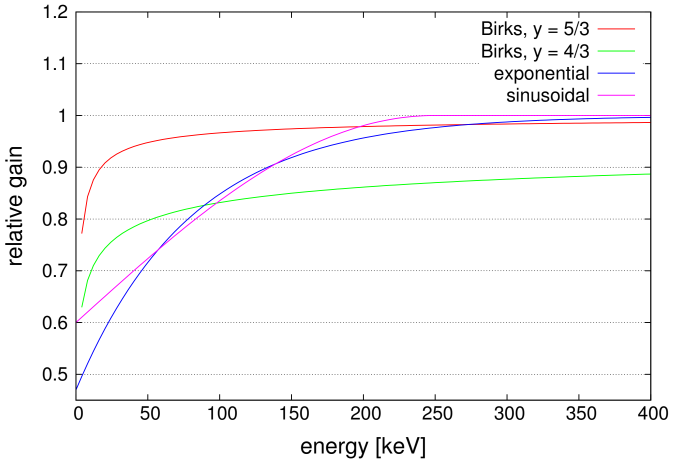

Figure 5.4: Gain $\mathrm{d}L(E)/\,\mathrm{d}E$ of the four analyzed non-linear approaches. The green curve is shifted for display reasons by -0.1 on the y-axis.

In [Leo94, Cho52, FKK53] several extensions to the first Birks model are described. Two of them are:

$$\frac{\mathrm{d}L}{\mathrm{d}x} = L_0 \cdot \frac{A\,\frac{\mathrm{d}E}{\mathrm{d}x}}{1 + B\,\frac{\mathrm{d}E}{\mathrm{d}x} + C\left(\frac{\mathrm{d}E}{\mathrm{d}x}\right)^2} \quad \text{and} \tag{5.18}$$

$$\frac{\mathrm{d}L}{\mathrm{d}x} = \frac{A}{2\,B}\,\ln\left(1 + 2\,B\,\frac{\mathrm{d}E}{\mathrm{d}x}\right) . \tag{5.19}$$

All these extensions have been shown experimentally to be still incomplete, particularly for large differential energy losses (low energies). Therefore, further analysis is necessary to determine the appropriate non-linear description of a scintillator detector at low energies. Especially more information is required in the energy range 100–300 keV.

Detector Efficiency – Number of Photo-Electrons

From the detector calibration the detector efficiency is derived as well. This property is expressed by PE, the number of photo-electrons at the first dynode of the photo-multipliers per MeV incident energy. The derived quantity can be compared with a theoretical estimation.

Using the refractive index of the scintillator to calculate the limiting angle of total reflection $\sin\theta_g = \frac{1}{n_{\text{scint}}}$, the spherical ratio of the detected photons can be derived:

$$
\begin{aligned}
R_\Omega &= \frac{1}{4\pi} \cdot \int_0^\Omega \mathrm{d}\Omega' = \frac{1}{4\pi} \cdot 2\int_{-\theta_g}^{\theta_g} \mathrm{d}\phi \cdot 2\int_0^{\pi/2-\theta_g} \sin\theta\,\mathrm{d}\theta \\
R_\Omega &\cong 16\,\% \,.
\end{aligned} \tag{5.20}
$$

The light attenuation of the scintillator can be estimated using the derived attenuation length (see section 5.1.2) and the approximate path length of the photons:

$$
R_{\text{att}} = \mathrm{e}^{-\frac{x}{x_{\text{att}}}} \approx \mathrm{e}^{-\frac{25\,\text{cm}}{70\,\text{cm}}} \approx 70\,\% \,. \tag{5.21}
$$

The light yield of the scintillator BC400 is specified as 65 % of that of Anthracene, which is [BS53]:

$$
N_{\text{photons}} = 0.65 \cdot 1.4 \cdot 10^4 \, \frac{\text{photons}}{\text{MeV}} = 9.1 \cdot 10^3 \, \frac{\text{photons}}{\text{MeV}} \,. \tag{5.22}
$$

With the quantum efficiency p of the photo-multipliers and an estimated additional attenuation due to the optical interfaces between scintillator, light guides and photomultipliers $D_{\text{int}} \approx 70\,\%$ [Plo00], the number of photo-electrons per MeV follows:

$$
PE_{\text{theo}} = p \cdot N_{\text{photons}} \cdot R_\Omega \cdot R_{\text{att}} \cdot D_{\text{int}} \approx 185 \, \frac{\text{photo-el.}}{\text{MeV}} \,, \tag{5.23}
$$

which is of similar order as the measured detector efficiencies:

$$
\begin{aligned}
PE_{\text{det}\,1} &\cong 135 \, \frac{\text{photo-el.}}{\text{MeV}} \quad \text{and} \\
PE_{\text{det}\,2} &\cong 165 \, \frac{\text{photo-el.}}{\text{MeV}} \,.
\end{aligned} \tag{5.24}
$$

The remaining deviations are mainly due to the uncertainties in D_{int} and the ratio R_{att}. The efficiency of detector 2 is higher, since the light guides of this detector were reworked before the beamtime, see section 4.1.

Uncertainty of Detector Calibration

The theoretical descriptions of the calibration spectra or the neutron decay spectra have to be rescaled and mapped using the energy to channel relation of eq. (5.6), before they are used to fit the measured experimental spectra. The parameters of the mapping function, offset O and gain g, can be derived in two different ways. Method 1: just like the energy threshold E_{th} and the number of photo-electrons PE, offset and gain can be derived from a fit to a calibration set. In the second method offset and gain are obtained by a fit to the neutron decay spectrum $\mathrm{sum}(E)$ with only these two free parameters.

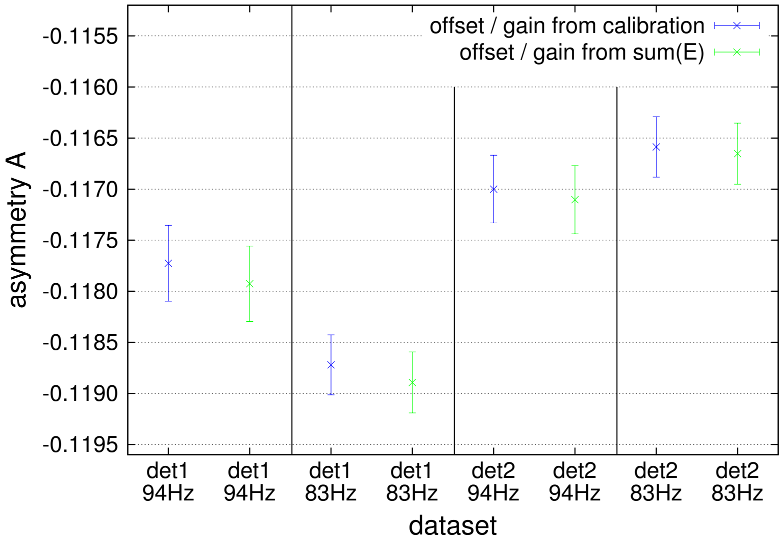

Figure 5.5: Results of the comparison analysis on the detector calibration. The parameter E_{th} and the number of photo-electrons PE are derived from the respective calibration sets. The data in blue show the asymmetries, when offset O and gain g are also obtained from the same calibration sets. In green, offset and gain are derived from a fit to the spectrum $\mathrm{sum}(E)$. The difference is about $1 \cdot 10^{-3}$. Note that the scatter of the individual pairs of asymmetry values is expected, since the necessary systematic corrections due to magnetic mirror effect and background, which are different for each dataset, are not applied.

Both methods were used to derive the β-asymmetry spectra from the whole dataset. The final difference of these two methods describes the uncertainty of the detector calibration. Figure 5.5 shows a comparison for each of the four available datasets. The resulting uncertainty of the detector calibration on the asymmetry A is:

$$\frac{\Delta A}{A}_{\mathrm{cal}} = 5 \cdot 10^{-4} \,. \tag{5.25}$$

The absolute values of A were finally derived according to method 2: the parameters offset O and gain g were derived from fits to $\mathrm{sum}(E)$, while PE and E_{th} were obtained from simultaneous fits to the calibration spectra. This method takes the non-uniformity of the detector response (see next section) into account.

5.1.2 Position Dependence of the Detector Response

The detector response depends on the plane position of an electron incidence on the detector. The analysis of this effect is necessary, since the measured electron beam is not point-like. Even if the electrons are emitted by one of the point-like calibration sources, the resulting electron beam hitting the scintillator is broadened in the plane, because of the gyration of the charged particles around the magnetic field lines. Close to the detectors, the radius is limited to (see eq. (3.15) and (3.21)):

$$r_{\mathrm{max}}^{\mathrm{det}} = r_{\mathrm{max}} \sqrt{\frac{B_{\mathrm{max}}}{B_{\mathrm{det}}}} \cong 3.6\,\mathrm{cm}\ . \tag{5.26}$$

The FWHM of the electron distribution is at $r' \approx 0.18 \cdot r_{\mathrm{max}}^{\mathrm{det}}$ [Fri08, Dub08b], which covers an area of about $A \approx 5\,\mathrm{cm}^2$. Furthermore the spatial profile of the electron beam, coming from decayed neutrons, follows certainly the profile of the neutron beam with additional gyration-broadening.

There are several possible reasons for a non-uniformity of a scintillation detector:

- Due to the so-called self-absorption process of the scintillation light, each scintillator has an intrinsic attenuation length. This decreases the number of photons on their way to the photomultipliers. The used scintillator (Bicron BC400) has an intrinsic attenuation length of $x_{\mathrm{att}} = 160\,\mathrm{cm}$, which results in a 0.2 % effect, see eq. (3.38).
- Solvent vapor can cause cracks on the surface of the scintillator, which decreases the specified attenuation length. A possible reason for the very short attenuation length of the PERKEO III detectors during the 2007 beamtime ($x_{\mathrm{att}} \approx 15\,\mathrm{cm} \Rightarrow 40\,\%$ effect) is assumed to be a detector exposure to Acetone vapor.
- Mechanical stress of the scintillator would further reduce the reflectivity of the surface.

- The six photomultipliers give a position dependent contribution to the total energy value of an incidence. Hence, the adjustment of the high-voltage power supply as well as the optical coupling of the photomultipliers to the scintillators are very important.

Before and during the 2009 beamtime several actions were taken, to improve the position dependence, see section 3.3.2. To quantify the remaining non-uniformity, the surfaces of both detectors were scanned several times during the beamtime with the available calibration sources. Most of the 2-dimensional scans were performed on a grid of 7×7 points in the plane, covering an area of about $20 \times 20\,\mathrm{cm}^2$.

Re-Calibration of the Detectors

Instead of a simple summation of the measured energies of the six photomultipliers, the sum D on each detector can be derived by re-calibrating the contribution of each photomultiplier:

$$D = \sum_{i=1}^{6} c_i \cdot P_i \, , \tag{5.27}$$

where P_i denote the contributions of each photomultiplier and c_i the respective scaling factors. By chosing an appropriate set of scaling factors c_i, the plane uniformity can be optimized. As a starting point for the re-calibration, the method from [Kre99] is used. Therefore the variance σ^2 of the 2-dimensional detector scans is calculated and minimized with regard to the used set of scaling factors c_i. The mean sum $\overline{D}$ is the average value of the complete 2D-scan:

$$\sigma^2 = \frac{1}{N} \sum_{j=1}^{N} \left(\sum_{i=1}^{6} c_i \cdot P_i^j - \overline{D} \right)^2 \, , \quad \overline{D} = \frac{1}{N} \sum_{j=1}^{N} \sum_{i=1}^{6} c_i \cdot P_i^j \tag{5.28}$$

$$\frac{\partial(\sigma^2)}{\partial c_k} = \frac{2}{N} \sum_{j=1}^{N} \left(\sum_{i=1}^{6} c_i \cdot P_i^j - \overline{D} \right) P_k^j \overset{!}{=} 0 \qquad \Rightarrow \tag{5.29}$$

$$\begin{aligned} \overline{D} \cdot \sum_{j=1}^{N} P_k^j &= \sum_{j=1}^{N} \sum_{i=1}^{6} c_i \cdot P_i^j \, P_k^j \\ &= c_k \cdot \sum_{j=1}^{N} \left(P_k^j \right)^2 + \sum_{j=1}^{N} \sum_{i \neq k}^{6} c_i \cdot P_i^j \, P_k^j \, , \end{aligned} \tag{5.30}$$

where P_i^j denotes the fitted peak position of the chosen radioactive source for each photomultiplier i and each measurement j of the total number of N measurements on the grid.

Equation (5.30) can be rewritten using the following matrices:

$$\mathbf{D} = \overline{D} \cdot \begin{pmatrix} \sum_j^N P_1^j \\ \vdots \\ \sum_j^N P_6^j \end{pmatrix}, \; \mathbf{M} = \begin{pmatrix} \sum_j^N P_1^j P_1^j & \cdots & \sum_j^N P_1^j P_6^j \\ \vdots & \ddots & \vdots \\ \sum_j^N P_6^j P_1^j & \cdots & \sum_j^N P_6^j P_6^j \end{pmatrix}, \; \mathbf{c} = \begin{pmatrix} c_1 \\ \vdots \\ c_6 \end{pmatrix} \tag{5.31}$$

$$\mathbf{D} = \mathbf{M} \cdot \mathbf{c} \quad \Rightarrow \quad \mathbf{c} = \mathbf{M}^{-1} \cdot \mathbf{D} \,. \tag{5.32}$$

To solve this system of equations and to derive the scaling factors c_i, just the values P_i^j have to be fitted and matrix $\mathbf{M}$ has to be inverted.

Due to the geometry of the detector and the arrangement of the photomultipliers, there is a strong position dependence of the measured spectrum on each photomultiplier. Figure 5.6 shows this dependence for a chosen plane position of $(160, 250)$ mm. With the upper right photomultiplier PM1/3 the measured ^{113}Sn peak is at a 10 times higher energy position compared to e.g. PM1/5, which is located on the lower right position of the scintillator. Due to

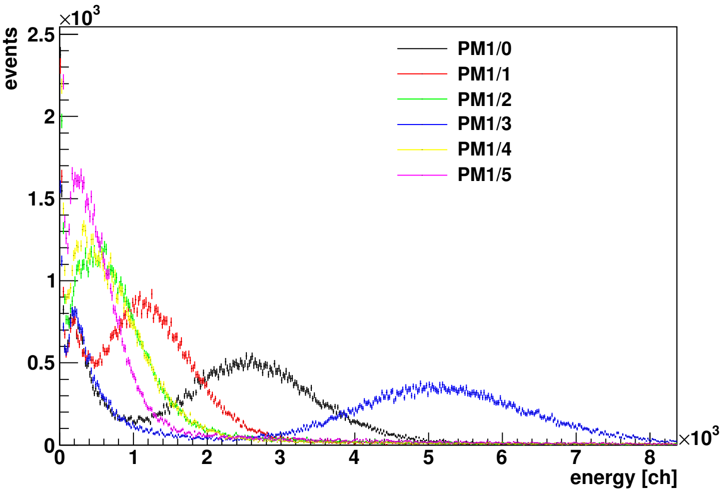

Figure 5.6: Measured spectra of the six photomultipliers on detector 1. The ^{113}Sn source was positioned at the plane position $(160, 250)$ mm, close to PM1/3. The energy of the ^{113}Sn peak, measured with this photomultiplier, was about 10 times higher compared with the two lower photomultipliers, PM1/2 and PM1/5.

the resulting large uncertainties on the derived values of P_i^j, the output of the previously described re-calibration method improves the uniformity, but does not result in an optimum.

The variance σ^2 in eq. (5.28) was further decreased using a new Monte Carlo tool *mc2D*. The resulting vectors $\mathbf{c}$ from the matrix inversion were taken as a starting point for the 6-dimensional minimization process. The final optimized values for the scaling factors c_i of the six photomultipliers on each detector are:

$$\mathbf{c}_{\text{det}\,1} = \{0.862, 0.786, 0.860, 0.926, 1.072, 0.981\} \quad \text{and} \tag{5.33}$$

$$\mathbf{c}_{\text{det}\,2} = \{0.913, 0.971, 0.803, 0.887, 1.039, 0.955\} \,. \tag{5.34}$$

Figure 5.7 shows the resulting uniformity on both detectors before and after the full re-calibration. The uniformity could be improved to about ±1 % within the corresponding surface area of the detectors. To test the results of the re-calibration according to the assumed $\cosh x$ behavior, two fitfunctions were defined and fitted to the data before and after the re-calibration:

$$f_1(x,y) = C1 \qquad \text{and} \tag{5.35}$$

$$f_2(x,y) = C2 \cdot \cosh \frac{x - x_0}{x_{\text{att}}} \,, \tag{5.36}$$

with x_{att} as fitted attenuation length. The results are:

Detector	**raw / re-cal**	σ^2 **of** $\mathbf{f_1(x,y)}$	σ^2 **of** $\mathbf{f_2(x,y)}$	$\mathbf{x_{att}}$ **[mm]**
1	raw	77/49	68/49	670
1	re-cal	35/49	26/49	680
2	raw	267/49	249/49	620
2	re-cal	92/49	68/49	610

As expected, on both re-calibrated detectors the function $f_2(x,y)$ describes the uniformity more accurately. The derived values for the attenuation length x_{att} are at least four times higher compared with the previous PERKEO III measurement in 2007, which results in a ±1 % instead of a ±20 % uniformity.

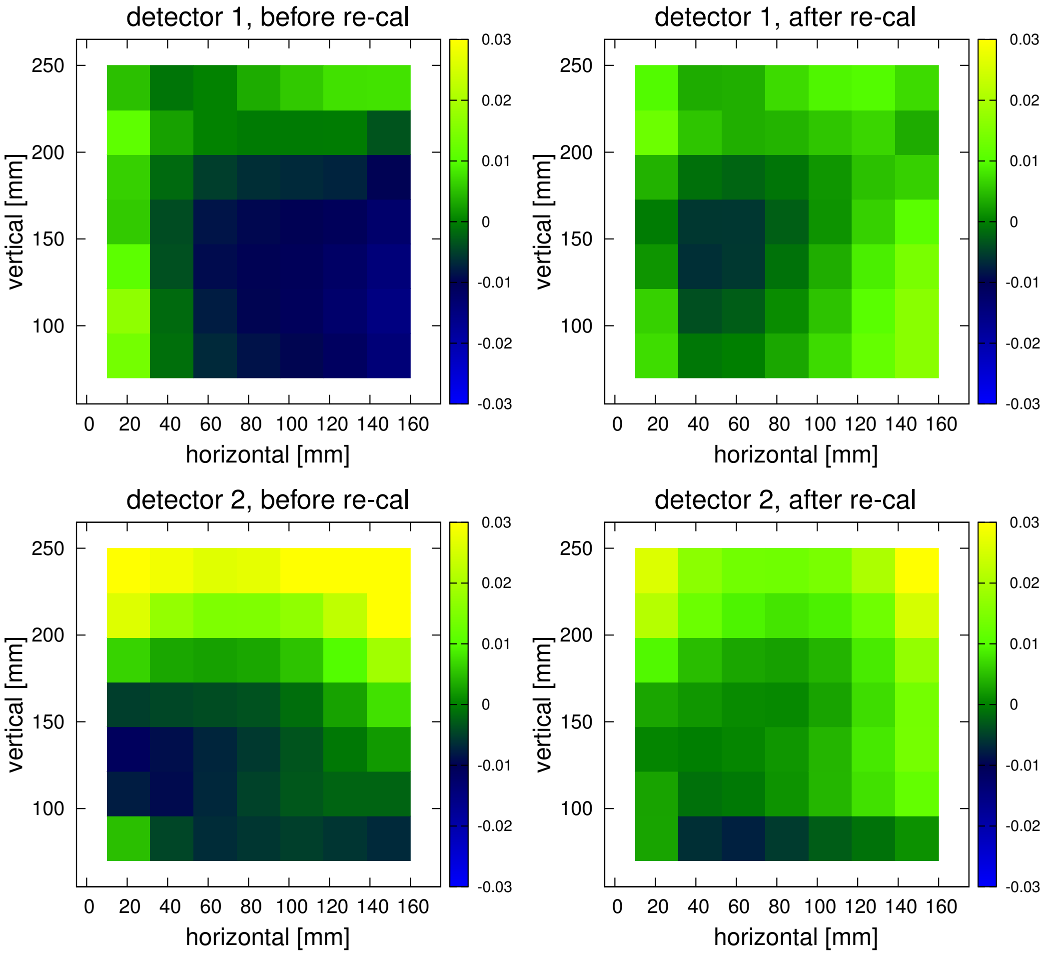

Figure 5.7: These four plots present the effect of the detector re-calibration. The left plots show the raw 2D-uniformity on detector 1 and 2, which is already noticeably more homogeneous, ±2 %, compared to previous PERKEO measurements [Fri08, Mun06, Rei99]. After applying the re-calibration methods, the uniformity could be improved to less than ±1 % (right plots).

5.1.3 Trigger Function

The probability that an event (e.g. electron or γ-quant) of energy E generates a trigger-event in the data acquisition system, is described by the trigger function $T(E)$, which tends to unity for higher energies. In the experimental setup of PERKEO III there are three detection cases to measure a spectrum with e.g. detector 1:

1. Event triggers only detector 1 $\Rightarrow$ event-spectrum on det 1: $P_1(E)$

2. Event triggers only detector 2 ⇒ unrecognized backscatter spectrum on det 1: $P_2(E)$
3. Event triggers detector 1, is reflected and triggers the opposite detector as well ⇒ event-spectrum on det 1: $P_3(E)$

Due to the symmetric detector design of Perkeo III, the backscattered events are measured as well. Hence, the trigger function $T(E)$ can be described using this property. The trigger function on detector 1 becomes:

$$T(E) = \frac{P_3(E)}{P_2(E) + P_3(E)} \,. \tag{5.37}$$

For low energies, the energy to channel relation of the detector is not linear (see section 5.1.1). Therefore the trigger function is given as function of ADC-channels *ch*.

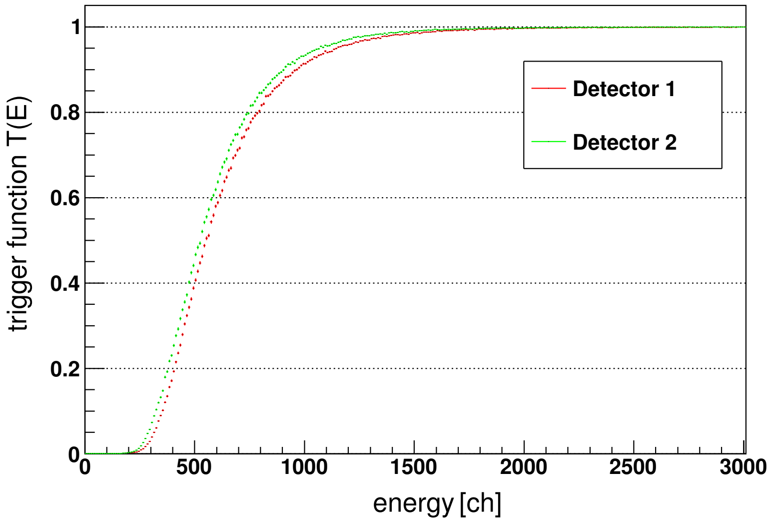

Figure 5.8: Trigger probabilities of detector 1 and 2 as function of energy in channels. The shown data are measured with discriminator threshold at value 4. The probability is close to unity above energies of 2000 ch (90 keV), which is significantly below the lower fit limit of the experimental asymmetry (300 keV, see section 5.7). The 50 % probabilities are at $T_1 \approx 30$ keV and $T_2 \approx 28$ keV (see table 5.3).

Figure 5.8 shows this probability function $T(E)$ for the dataset, measured with the discriminator threshold at value 4 (4 mV @ 50 Ω). The 50 % and 90 % values of the trigger functions are listed in table 5.3.

Detector	T_{50} [ch]	T_{50} [keV]	T_{90} [ch]	T_{90} [keV]
Det 1	550	41	960	57
Det 2	525	40	910	56

Table 5.3: Energy values of the 50 % and 90 % trigger probabilities from fig. 5.8. The numbers given in keV are derived according to section 5.1.1, using the exponential non-linear approach.

These values are within the expected range, assuming a photomultiplier pulse length of about 20 ns:

$$E = \frac{U^2}{R} \cdot \Delta t = \frac{(4\,\mathrm{mV})^2}{50\,\Omega} \cdot 20\,\mathrm{ns} \cong 40\,\mathrm{keV}\ . \tag{5.38}$$

Even these rather low trigger thresholds (compared with previous PERKEO measurements) create some minor systematic effects. There is a certain probability that an electron hits one of the detectors, does not trigger the electronics, is reflected to the opposite detector and creates an event there. The consequences are twofold: the value of the measured energy is wrong and – even more important – the assignment of this event to the detectors is wrong. The symmetric setup of PERKEO III helps to minimize this systematic effect. To estimate this, an analytic description of the trigger function is given below.

Theoretical Description of the Trigger Function

In [Fri08] the trigger function $T(E)$ was derived using binomial distributions for the quantum efficiency p of the photomultipliers and for the coincidence criterion *two–of–six*. Two descriptions were derived: $T_1(ch)$, when one photo-electron is sufficient to trigger the data acquisition system, and $T_2(ch)$, when two photo-electrons are necessary:

$$T_1(ch) = 1 - (1-p)^{6\cdot ch\cdot a} \cdot \left[\frac{6}{(1-p)^{ch\cdot a}} - 5\right] \qquad \text{and} \tag{5.39}$$

$$T_2(ch) = 1 - \left[(1-p)^{ch\cdot a} \cdot \left(1 + \frac{ch\cdot a\cdot p}{1-p}\right)\right]^6 \cdot \left[\frac{6}{(1-p)^{ch\cdot a} \cdot \left(1+\frac{ch\cdot a\cdot p}{1-p}\right)} - 5\right]\ , \tag{5.40}$$

with energy scaling parameter a and quantum efficiency p. Since it is expected that one photo-electron is sufficient to trigger the discriminator (see eq. (3.41)), $T_1(ch)$ is assumed to fit the data more accurately.

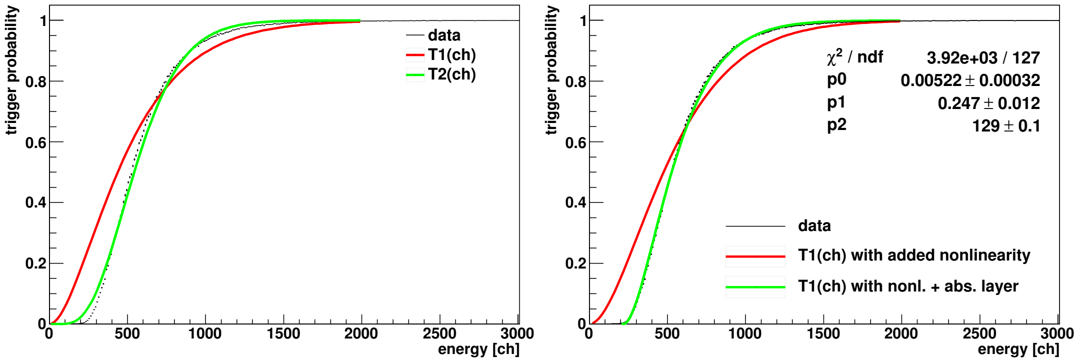

(a) Measured trigger function (black) together with the original fitfunctions $T_1(ch)$ and $T_2(ch)$, see eq. (5.39), (5.40). The function $T_1(ch)$ fits worse compared with $T_2(ch)$. Both give non-physical results for the parameters a and p.

(b) Two modified fitfunctions, based on $T_1(ch)$. In red, $T_1^\star(ch)$, the exponential non-linearity of the detector is implemented. In green, $T_1^\dagger(E)$, an absorption layer is added. $T_1^\dagger(E)$ fits more decently and gives physical values for a and p.

Figure 5.9: Measured trigger function together with the original fitfunctions $T_1(ch)$, $T_2(ch)$ on the left side and with modified fitfunctions $T_1^\star(ch)$ (red) and $T_1^\dagger(ch)$ (green) on the right side.

Figure 5.9a shows the fits of both function to the data. $T_1(ch)$ (red curve) does not fit decently and the derived values of the parameters in the fit of $T_2(ch)$ are non-physical.

Since the scintillation detectors have a non-linear energy response for energies below about 200 keV (see section 5.1.1), these two fitfunctions are adapted accordingly, using the exponential approach:

$$ch \cdot a \rightarrow ch \cdot a + O \cdot \left(1 - \mathrm{e}^{-ch/ch_{\mathrm{th}}(E_{\mathrm{th}})}\right) \qquad \Rightarrow \tag{5.41}$$

$$\begin{aligned} T_1^\star(ch) &= 1 - (1-p)^{6 \cdot \left(ch \cdot a + O \cdot \left(1 - \mathrm{e}^{-ch/ch_{\mathrm{th}}}\right)\right)} \\ &\times \left[\frac{6}{(1-p)^{ch \cdot a + O \cdot \left(1 - \mathrm{e}^{-ch/ch_{\mathrm{th}}}\right)}} - 5 \right] , \end{aligned} \tag{5.42}$$

and $T_2^\star(ch)$ follows similarly. The new function $T_2^\star(ch)$ still gives non-physical values, while the fit result of $T_1^\star(ch)$ is only slightly improved, see red curve in fig. 5.9b. In these fits, the non-linear parameter $ch_{\mathrm{th}}(E_{\mathrm{th}})$ and the offset O

were fixed to the derived values of section 5.1.1, only the scaling factor a and quantum efficiency p were free parameters. As next step a new parameter was added, which would physically describe a thin absorption layer at the surface of the scintillator.

$$
\begin{aligned}
ch \cdot a \rightarrow ch \cdot a + O_0 + O \cdot \left(1 - \mathrm{e}^{-ch/ch_{\mathrm{th}}(E_{\mathrm{th}})}\right) \qquad & \Rightarrow \qquad \qquad (5.43) \\
T_1^{\dagger}(ch) = 1 - (1-p)^{6 \cdot \left(ch \cdot a + O_0 + O \cdot \left(1 - \mathrm{e}^{-ch/ch_{\mathrm{th}}}\right)\right)} & \\
\times \left[\frac{6}{(1-p)^{ch \cdot a + O_0 + O \cdot \left(1 - \mathrm{e}^{-ch/ch_{\mathrm{th}}}\right)}} - 5 \right] , & \qquad \qquad (5.44)
\end{aligned}
$$

The fit with the function $T_1^{\dagger}(ch)$ to the data was performed with fixed values for $ch_{\mathrm{th}}(E_{\mathrm{th}})$ and O. This new function fits much more decently to the data and the derived values are (see green curve in fig. 5.9b):

$$
\begin{aligned}
p &= 0.25 \, , && (5.45) \\
a &= 5.2 \cdot 10^{-3} \, \frac{\text{photons}}{\text{ch}} \quad \text{and} && (5.46) \\
O_0 &= 129 \, \text{ch} \, . && (5.47)
\end{aligned}
$$

Besides the acceptable shape, the quantum efficience p is close to the specified value of 0.26, see section 3.3.2. The value of a describes the number of photons per photomultiplier per channel. It can be used to derive the detector relevant number of photo-electrons per 1 MeV, which gives:

$$
\begin{aligned}
PE &\approx a \cdot gain \cdot \langle \#\,\text{of PMTs} \rangle \cdot p \\
&\approx 250 \, \frac{\text{photo-electrons}}{\text{MeV}} \, , \qquad (5.48)
\end{aligned}
$$

which is about 50 % above the derived number, when fitting the calibration sources with *p3fit*, see eq. (5.24). An offset of $O_0 = 129\,\text{ch}$ corresponds to an energy of about 4 keV.

As a conclusion, the modified theoretical trigger function $T_1^{\dagger}(ch)$ fits decently to the data and delivers three physically relevant parameters.

5.1.4 Electron Backscattering

There is a certain probability that an electron leaves the scintillator before it has deposited its energy completely. This effect depends strongly on the kinetic energy E and the incident angle θ. Backscattering can produce some significant effects:

- When the electron has created a trigger event, backscattering will reduce and therefore distort the measured energy.
- Assuming that the energy of the electron is not sufficient to trigger the system, backscattering to the opposite detector can produce a wrong assignment of this electron to the detection system.

Since backscattering is an intrinsic property of low energy electron detectors, it can not be avoided. Hence, it is very important to understand and quantify this energy and angle dependent effect, so that the necessary systematic correction and uncertainty on the asymmetry A can be derived. Figure 5.10 shows the measured spectrum $\text{sum}(E) = N^{\uparrow}(E) + N^{\downarrow}(E)$. When the backscattered events are not accounted for (green curve), the spectrum shifts towards lower energies and changes its shape.

The magnetic field strength in PERKEO III decreases towards the two symmetric detectors. This has two consequences: first, the angular distribution is limited

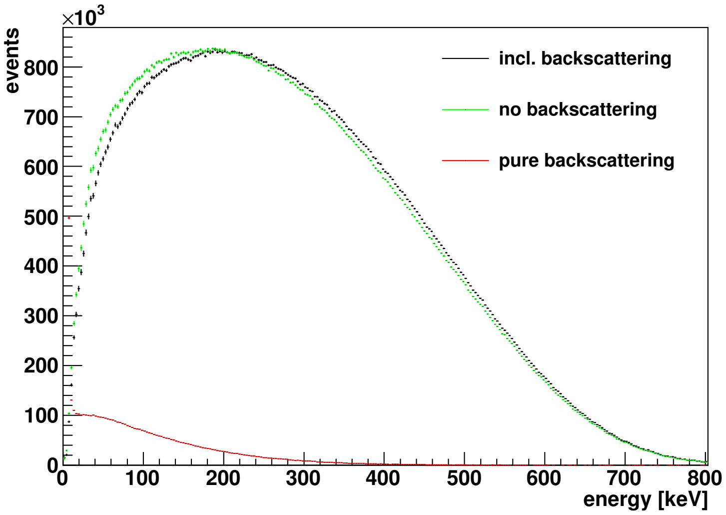

Figure 5.10: The β-spectrum $\text{sum}(E)$ is shown with (black) and without (green) energy contribution of backscattered electrons. The backscattered electrons (red), measured with the opposite detector, have predominantly low energies.

to angles below $\theta \approx 47^\circ$, see eq. (3.25). Particles with a small incident angle θ have a larger penetration depth. The second effect is that backscattered electrons move towards an increasing magnetic field strength, with a possible reflection at the magnetic mirror and another incident to the same detector. The remaining particles, which are able to overcome the maximum of the magnetic field at the center of the decay volume, hit the opposite detector. Because of the resulting flight time to the opposite detector, the measurement time of the energy (integration process in the ADCs) is set to $t_{\text{gate}} = 300\,\text{ns}$ (see backscatter function in fig. 4.7). This is necessary to measure electrons for all possible backscatter-scenarios. To reconstruct the final backscatter-corrected spectra (black curve in fig. 5.10), the energy measured with the opposite detector has just to be added to the energy on the incident detector.

In conclusion, the effect of missing energy due to backscattering is prevented by the experimental design. The issue of a possible wrong assignment of an electron with respect to the incident detector will be discussed later.

Short Gate Time of the ADCs, *mcBackscatter*

The new ADCs did not behave as expected for one property: the ADC-internal integration time deviated from the programmed gate time. This has the consequence that the energy of backscattered events is lost, when they are slower than $t_{\text{gate}} \cong 220\,\text{ns}$.

To estimate the systematic impact of this ADC behavior, a new Monte Carlo tool *mcBackscatter* was created. In [Wie05] electron backscatter calculations were made using the electron transport code *ETRAN*.[2] Electrons with kinetic energies from 100 to 700 keV in intervals of 100 keV and with incident angles from 0° to 90° in steps of 15° were directed to a plastic scintillator, similar to those in the PERKEO III detectors. The derived distributions of backscatter probability, backscattered energy and exit angle, which are functions of incident energy and angle, are described by phenomenological functions.

In the new Monte Carlo tool *mcBackscatter* the parameters of these calculations on the 7×7 grid were interpolated and the resulting continuous functions were used to calculate the necessary PDF-, CDF- and inverse CDF-functions.[3]

---

[2] ETRAN computes the transport of electrons and photons through e.g. a plastic scintillator, see http://www.oecd-nea.org/tools/abstract/detail/ccc-0107/.

[3] PDF: normalized probability density function, CDF: cumulative distribution function. $CDF(y) = \int_{-\infty}^{y} PDF(x)\,\mathrm{d}x$.

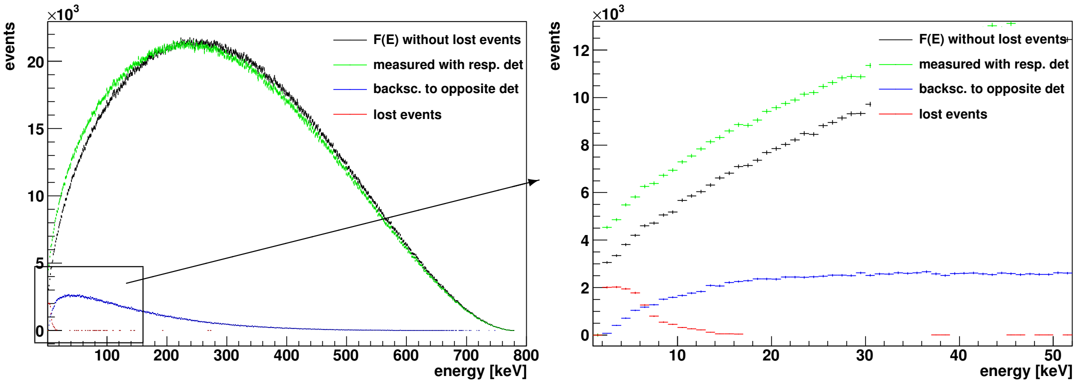

Figure 5.11: Several spectra derived with the new Monte Carlo tool *mcBackscatter*. The lost events (red) appear only below about 10 keV, see zoomed figure on the right. The green spectrum has not included any backscattered events (compare with green curve in fig. 5.10), the blue curve shows the spectrum of the events, which are backscattered and measured with the opposite detector, and the black spectrum includes all directly measured and backscattered events. This latter spectrum is compared with the theoretical spectrum $F(E)$, see below. The number of events in this Monte Carlo analysis is $1 \cdot 10^7$.

The model, used to describe the incident electrons, is based on the angular distribution at the PERKEO III detectors (see fig. 3.7) and the phase space factor $F(E)$, see eq. (2.13). For each modeled electron, the following parameters were derived:

- Incident energy E according to the CDF of $F(E)$
- Polar decay angle θ in the decay volume, see eq. (3.24), and at the detector, see eq. (3.30)
- Backscatter probability η as function of the incident angle θ and energy E
- If applicable, the energy of the backscattered electron E_{back}
- Angle of backscattered electron θ_{back}

The flight time of an electron from one to the opposite detector depends on the energy, the backscatter angle and the magnetic field profile. An already existing Monte Carlo tool *Magfield3*[4] is able to calculate the flight time, using these input parameters. Now the flight time $t(E, \theta)$ is used as a criterion, whether a backscattered electron is fast enough to be measured or not. An exemplary run with the Monte Carlo tool *mcBackscatter* gives the following results:

---

[4] Magfield3, developed and supported by Ferenc Glück, calculates magnetic field profiles and electron trajectories using specific data of a solenoid system [Glü11a, Glü11b].

- Total number of electrons in the Monte Carlo simulation: $1 \cdot 10^{7}$
- Relative number of all backscattered electrons: $9.2 \cdot 10^{-2}$
- Backscattered electrons, measured with the same detector: $4.3 \cdot 10^{-2}$
- Backscattered electrons, measured with the opposite detector: $4.9 \cdot 10^{-2}$
- Relative number of lost backscattered electrons: $1.2 \cdot 10^{-3}$

The resulting spectra are shown in fig. 5.11. The energies of the missing events are mainly below 10 keV. The effect of missing events on the spectrum $\mathrm{sum}(E)$ is analyzed and shown in the left plot of fig. 5.12. The fit in this plot is made with the normalization as only free parameter. Then two Monte Carlo generated spectra, with and without the lost events, are used to fit the measured spectrum $\mathrm{sum}(E)$ with two free parameters offset O and gain g. The deviation between the two derived parameters g_{with} and g_{without} is about $\Delta g/g \cong 0.3(5.7) \cdot 10^{-4}$, which would propagate to an uncertainty on the correlation coefficient A:

$$\frac{\Delta A}{A} \approx 0.08(1.43) \cdot 10^{-4} \; . \tag{5.49}$$

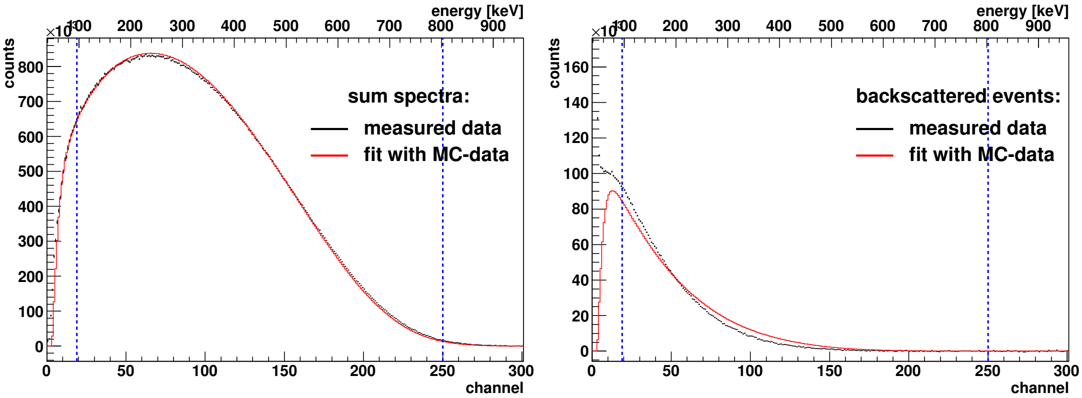

Figure 5.12: Fit with derived Monte Carlo spectra (red) to the measured data (black), with the normalization as the only free parameter, while offset O, gain g and non-linear threshold E_{th} are derived from a fit to a calibration set, see section 5.1.1. On the left side the measured spectrum $\mathrm{sum}(E)$ including the backscattered events is fitted, on the right side only events, which are backscattered to the opposite detector.

As part of a Master Thesis the backscattering effect is currently analyzed using *Geant4*,[5] another Monte Carlo tool, developed and supported by CERN.

---

[5] GEANT is an acronym for GEometry ANd Tracking. Since *Geant4* is optimized for high particle energies, the PENELOPE code was implemented and used to simulate the transport of the electrons.

It can be used to simulate the transport properties of particles during their motion through matter. The input parameters of this simulation are the angular distribution of the electrons at the detector according to eq. (3.30), the phase space factor $F(E)$ of eq. (2.13) and some material parameters of the plastic scintillator.

Since the future project *PERC* does not provide a symmetric $2\times 2\pi$ detector design, these two simulation tools are able to support pre-studies regarding the backscattering effect. And finally, the tool *mcBackscatter* showed that the effect of the short gate time of the ADCs results in a very small effect on the asymmetry correlation coefficient A, see eq. (5.49).

Unrecognized Backscattering and Wrongly Assigned Events

Figure 5.13 shows all trigger possibilities in case of an electron hitting detector 1. For cases a and b there is no measurable backscattering at all.[6] When the electron is backscattered, there is a certain probability that it triggers detector 2 as well (case c). If not, backscattering is unrecognized (case d, emphasized in green). However, this case is covered, since the ADCs measure the energy of all photomultipliers, when any of the detectors is triggered. The only critical case is, when the electron does not trigger the primary detector, is reflected and does trigger the opposite detector (case e, emphasized in red). This would result in a wrong detector assignment.

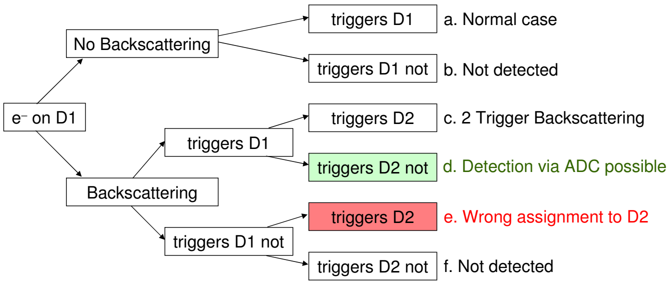

Figure 5.13: Possibility tree for incident electrons. Case e is critical, since the electron is assigned to the wrong detector [SA08].

To estimate the number and spectral distribution of the wrongly assigned electrons, several backscatter spectra are generated, using the same notation as in [SA08]:

- $H_1(E)$: backscattered events, which trigger both detectors, case c.

---

[6] Note: case a does also include, when the electron is backscattered at one detector, reflected at the magnetic mirror and finally measured with the same detector.

- $H_2(E)$: backscattered events, which must not trigger the second detector, according to case c + case d.
- $H_3(E)$: spectrum $H_1(E)$ divided by the trigger function $T(E)$. The resulting spectrum is equivalent to a backscatter spectrum, measured with a trigger efficiency of $T(E) = 1$.
- Therefore, the difference $H_2(E) - H_3(E)$ represents the fraction of the wrongly assigned events according to case e.

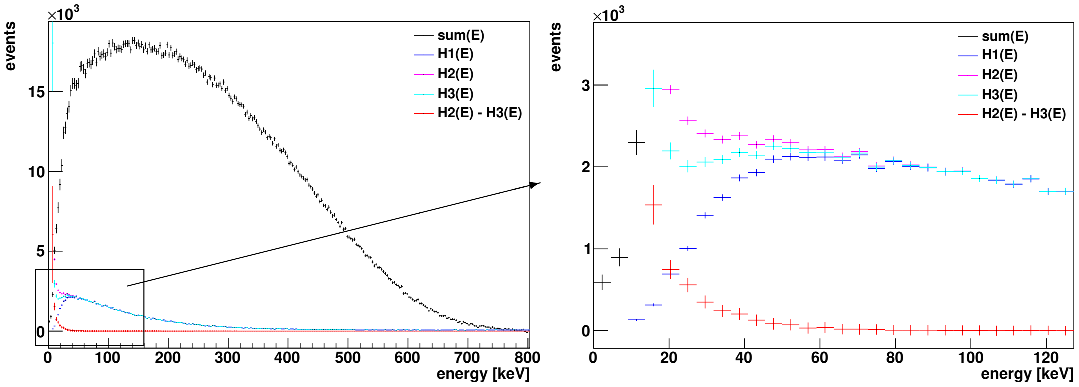

Figure 5.14: Backscatter spectra $H_1(E)$, $H_2(E)$, $H_3(E)$ and the difference $H_2(E) - H_3(E)$. The overall fraction of wrongly assigned events (red) vs. the spectrum $\text{sum}(E)$ is about $2 \cdot 10^{-3}$ at energies below 40 keV.

Figure 5.14 shows these spectra together with the spectrum $\text{sum}(E)$ as a reference.[7] The spectrum of the wrongly assigned events is marked in red. The overall $2 \cdot 10^{-3}$ wrongly assigned events yield an uncertainty on the asymmetry correlation coefficient A of [SA08]:

$$\frac{\Delta A}{A} < 1 \cdot 10^{-4} \,. \tag{5.50}$$

5.2 Time of Flight Spectra

By using a pulsed neutron beam, the signals from the decay products and the beam related background are functions of the time of flight of the neutrons. As previously shown in section 3.4 and fig. 3.9, there is the *signal* time window in the ToF spectrum, in which the neutron pulse is completely located inside the decay volume, and the *background* time window, with no neutrons inside the entire spectrometer.

---

[7] Here, the spectrum $\text{sum}(E)$ does not include the backscattered events, according to case a.

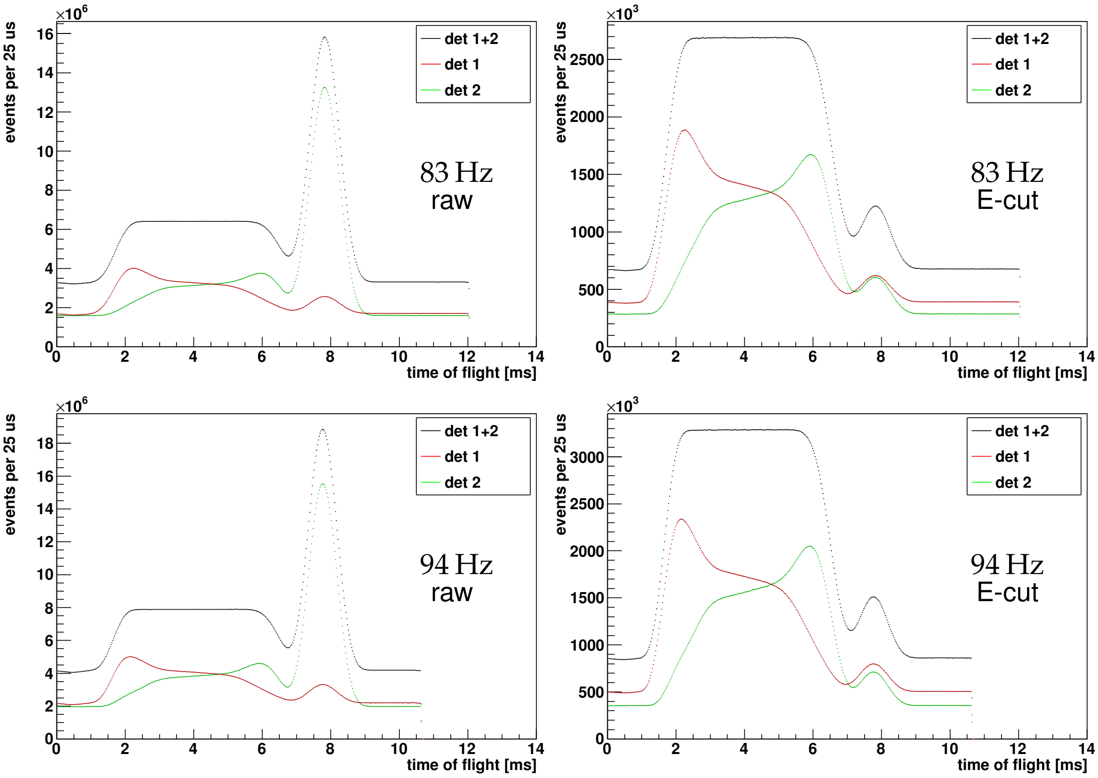

Figure 5.15: Several time of flight spectra with (300 keV $< E <$ 700 keV) and without energy cuts. The effect of the magnetic mirror on the decay electrons (section 3.3.1) is clearly visible. The eventrates on the two detectors (red and green) show positive and negative slopes at flight times of about 3–5 ms, while the sum of these spectra is flat (black curves). The downstream detector, det 2 close to the beamstop, measured much more γ-radiation from the absorption process of the neutron pulse, while the influence on the upstream detector (det 1) is weak. This strong peak nearly disappears in the plots with the energy cut (right), hence these events are not within the asymmetry fit range.

In fig. 5.15 the ToF spectra are shown for both detectors separately and for the sum. The magnetic mirror effect as well as the absorption process of the neutrons at the beam stop are visible. The latter results in a strong shower of γ-radiation on detector 2. In the following the signal time window is discussed. The background time window is covered in section 5.3.1 and 5.3.2. To determine the appropriate time window for the signal measurements, two possible methods were analyzed.

ToF Spectra During the Signal Time Window

As a starting point in this analysis the energy cutted ToF spectra from fig. 5.15 are background corrected. The left plot in fig. 5.16 shows the two spectra from detector 1 and 2 of the 94 Hz measurements. The crossing point of the spectra defines the center point of the signal time window. Now the window width is determined using the region of approximately constant slopes in the ToF spectra. The derived signal windows are:

$$t_{sig}^{83} \in [3.2, 5.2]\,\mathrm{ms} \quad \text{and} \quad t_{sig}^{94} \in [3.1, 5.1]\,\mathrm{ms}\,. \tag{5.51}$$

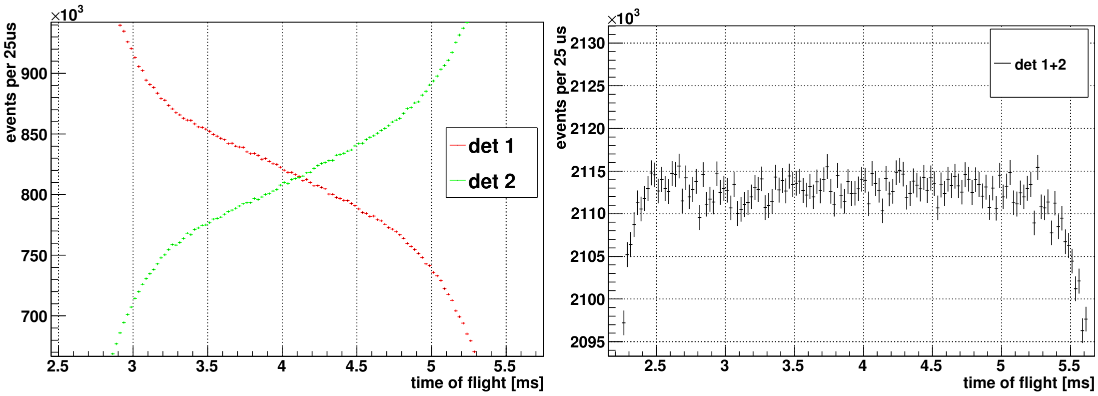

Figure 5.16: Left: the crossing point of the two background corrected signal spectra is at 4.1 ms. **Right:** the sum of these two spectra is flat over a period of 3 ms (94 Hz data).

The right plot in fig. 5.16 shows the sum of the ToF spectra from detector 1 and 2. It reveals a constant eventrate over the whole signal time window.

Asymmetry as Function of the Time of Flight

The asymmetry on both detectors was derived for subsequent time intervals of $\Delta t = 100\,\mu\mathrm{s}$, starting at $t_1 = 1\,\mathrm{ms}$ up to $t_2 = 6\,\mathrm{ms}$. Figure 5.17 shows the result of this analysis. The asymmetry A is a function of the ToF of the neutrons due to the clearly visible effect of the magnetic mirror. The results of a constant fit to the averaged data are listed in table 5.4.

The visible crossing point of the asymmetries on detector 1 and 2 is taken as a center of the signal time window and the available signal window width follows from the region with a small slope on A. The derived signal windows of the 83 Hz and 94 Hz data were exactly the same as previously derived in eq. (5.51).

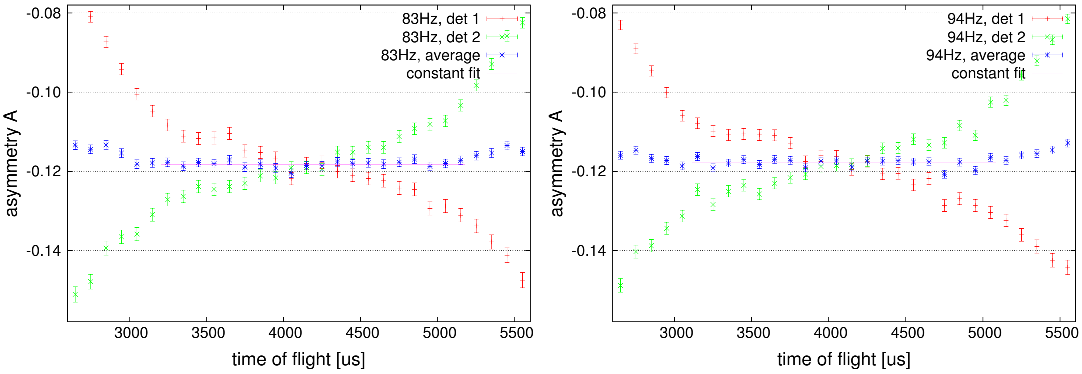

Figure 5.17: Asymmetry A as function of the time of flight of the neutron pulse. **Left:** chopper at 83 Hz, **right:** 94 Hz. For flight times below about 4 ms, detector 1 measures a smaller (absolute) asymmetry (red), while it is increased on detector 2 (green), due to the magnetic mirror effect. The average of the two detectors (blue) is fitted over the signal windows in eq. (5.51) and the respective results are given in table 5.4

Chopper freq.	Uncertainty on A	Reduced χ^2	Probability
83 Hz	$2.0 \cdot 10^{-3}$	11/19	0.92
94 Hz	$2.0 \cdot 10^{-3}$	24/19	0.20

Table 5.4: Results of the constant fits to the data, shown in fig. 5.17. The used fitrange is given in eq. (5.51).

5.3 Background

Background radiation is constantly present in the environment. It is emitted from a variety of natural and artificial sources. In experimental physics these sources can be dependent (section 5.3.2) or independent (section 5.3.3) on the experimental setup.

By using a pulsed neutron beam at least the beam related background is not constant but a function of the time of flight of the neutrons. This section discusses the implications of time dependent and all other sources of background.

5.3.1 Background in the Time of Flight Spectra

After all neutrons of the pulse are absorbed in the beamstop, there are no charged particles from neutron decay anymore in the spectrometer. The events, which can be measured until the next neutron pulse enters the experiment, are pure background. To ascertain the appropriate time window for the background measurement, the data are selected according to their energy and only events within the range of 300 keV $< E <$ 700 keV are used. These spectra together with linear fits are shown in fig. 5.18, while table 5.5 presents an overview of the fit results.

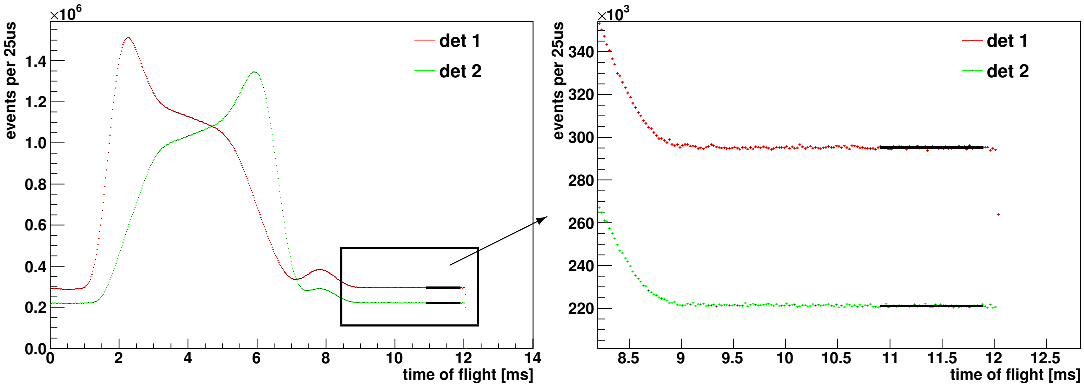

Figure 5.18: Time of flight spectra of the 83 Hz dataset with an energy cut of 300 keV $< E <$ 700 keV. The values for the slope of a linear fit to the spectra as well as the respective χ^2 are shown in table 5.5.

Dataset	Fitrange [ms]	Rel. Slope per ms	χ^2 / ndf	Prob.	Correction & Uncertainty
det 1 83 Hz	10.90–11.90	$-0.2(1.0) \cdot 10^{-3}$	37.4 / 38	0.50	$-0.1(0.7) \cdot 10^{-3}$
det 2 83 Hz	10.90–11.90	$-0.3(1.1) \cdot 10^{-3}$	37.0 / 38	0.52	$-0.2(0.8) \cdot 10^{-3}$
det 1 94 Hz	9.55–10.55	$-1.4(1.0) \cdot 10^{-3}$	29.8 / 38	0.83	$-1.0(0.7) \cdot 10^{-3}$
det 2 94 Hz	9.55–10.55	$-2.6(1.1) \cdot 10^{-3}$	40.4 / 38	0.36	$-1.8(0.8) \cdot 10^{-3}$

Table 5.5: Relative slopes and χ^2 values of the linear fits to the ToF spectra for the chosen background time windows, see fig. 5.18. The reduced χ^2 for the 83 Hz data are close to unity, while the background slopes are of the order $\mathcal{O}(3 \cdot 10^{-4})$ per millisecond. The chopper period and therefore the available background time windows are shorter in the 94 Hz dataset. This results in larger slopes, which are about $2 \cdot 10^{-3}$ per ms.

Since background should not be time dependent, the slopes of the linear fits should be zero. The derived values for the slopes are zero-compatible in the 83 Hz datasets with reduced χ^2 values close to unity. The slopes of the 94 Hz datasets are about $2 \cdot 10^{-3}$ per ms, since the available time window for the background measurement is shorter.

Before the background spectra are subtracted from the signal spectra, they are scaled by the factor $r = \frac{\text{signal time}}{\text{bg time}} = 2$. Therefore, the final corrections and uncertainties due to the background slope follow accordingly, see last column in table 5.5.

A resulting systematic correction and uncertainty on the asymmetry correlation coefficient A can be derived, using the definitions in eq. (5.1):

$$A = \frac{S^{\uparrow} - S^{\downarrow}}{S^{\uparrow} + S^{\downarrow} - r \cdot B} \,. \tag{5.52}$$

After a derivation with respect to the background B, the relative uncertainty on A becomes:

$$\begin{aligned}
\frac{\partial A}{\partial B} &= A \cdot \frac{r}{S^{\uparrow} + S^{\downarrow} - r \cdot B} \qquad \text{and therefore} \\
\frac{\Delta A}{A} &= \frac{\partial A}{\partial B} \cdot \frac{\Delta B}{A} = \frac{\Delta B}{B} \cdot \frac{r \cdot B}{S^{\uparrow} + S^{\downarrow} - r \cdot B} \\
&= \frac{\Delta B}{B} \cdot \frac{1}{\frac{S^{\uparrow}+S^{\downarrow}}{r \cdot B} - 1} \equiv \frac{\Delta B}{B} \cdot SF(E) \,.
\end{aligned} \tag{5.53}$$

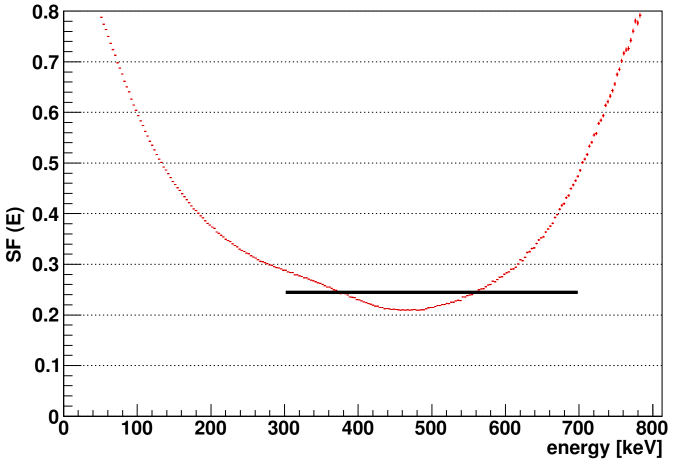

Figure 5.19: The energy dependent suppression function $SF(E)$ in eq. (5.53) gives the relative influence on the uncertainty of the experimental asymmetry, resulting from the systematic uncertainty of the background, see table 5.5. Therefore the uncertainty $\Delta A/A$ is about 25 % of $\Delta B/B$.

Figure 5.19 shows the influence of a background uncertainty $\Delta B/B$ on the uncertainty of the asymmetry $\Delta A/A$. The suppression is close to the signal–to–background ratio $\frac{S^{\uparrow}+S^{\downarrow}}{r \cdot B}$ in the relevant energy range. The resulting relative uncertainties on A due to the background uncertainties are collected in table 5.6.

Dataset	Correction on A	Uncertainty on A
det 1 83 Hz	$-0.4 \cdot 10^{-4}$	$1.8 \cdot 10^{-4}$
det 2 83 Hz	$-0.5 \cdot 10^{-4}$	$1.9 \cdot 10^{-4}$
det 1 94 Hz	$-2.5 \cdot 10^{-4}$	$1.8 \cdot 10^{-4}$
det 2 94 Hz	$-4.5 \cdot 10^{-4}$	$1.9 \cdot 10^{-4}$
average	$-2.0 \cdot 10^{-4}$	$0.9 \cdot 10^{-4}$

Table 5.6: Corrections and uncertainties of the asymmetry coefficient A, resulting from background uncertainties in the time of flight spectra during the background time windows.

5.3.2 Beam Related Background

Beam related background is intrinsically linked with the neutron beam. For that reason it is impossible to measure either the electron signal or this background signal separately. The origin of beam related background is mainly due to several scattering and absorption processes of neutrons from the beam, e.g. at the velocity selector, polarizer, collimation system, chopper or beamstop. In a pulsed beam measurement it is very important that there is no time dependent structure in the measured time of flight spectra.

Analysis of the LiF Tile Measurement

Two possibilities to estimate the approximate time dependent background contribution to the ToF spectra are:

1. Measurement without magnetic field. With completely disabled B-field the charged decay products are no longer projected to the detectors and the signal vanishes. Only uncharged background remains, which is therefore directly accessible.
2. Measurement with blocked neutron beam. To be still sensitive to γ-radiation created by the chopper, the beamline and the collimation system, a beamstop can be placed directly behind the chopper, to measure the beam related background of these components.

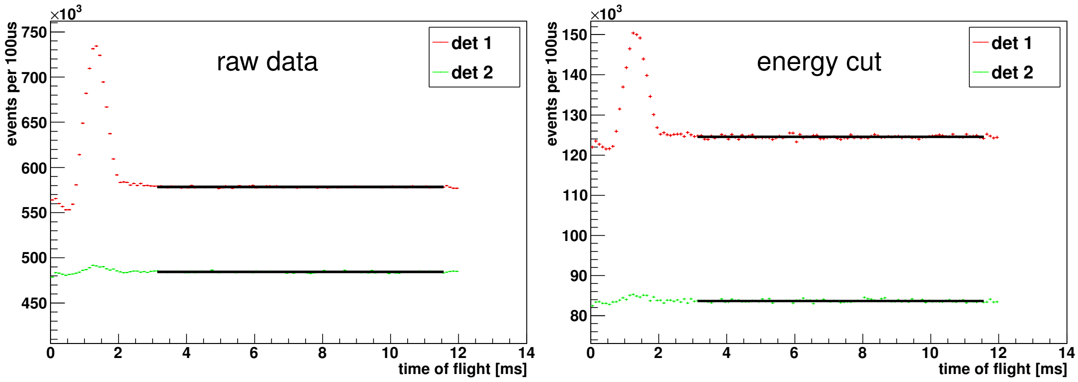

Figure 5.20: Time of flight spectra of the ^{6}LiF measurement with chopper frequency at 83 Hz. The left plot shows the spectra of the raw measured events, on the right only events within an energy range of about 200 keV $< E <$ 700 keV are plotted. The beamstop peak is now at $t \approx 1.5$ ms. The χ^2-values of a constant fit are shown in table 5.7.

Data	χ^2 /ndf		Probability	
	Det 1	Det 2	Det 1	Det 2
raw	89.2 / 84	108.7 / 84	0.67	0.96
E-cut	100.8 / 84	90.8 / 84	0.9	0.71

Table 5.7: χ^2 values and probabilities of constant fits to the ToF spectra in fig. 5.20. The 94 Hz dataset gives similar numbers.

The second method was applied during the beamtime, see section 4.3. To collect sufficient statistics, the measurement ran for about four days in this setup, both chopper frequencies were applied (94 Hz and 83 Hz). The ToF spectra of this measurement are shown in fig. 5.20 together with a constant fit over a large period of time. The results of the fits (shown in table 5.7) as well as the shape of the signals do not show any time dependent structure during the signal time. This gives a further strong confidence that the beam related background, which is measured during the background time window, is equivalent to that during the signal time window.

5.3.3 Beam Independent Background – Dependence on Neighbor Experiments

Beam independent background appears even when the respective neutron beam is switched off. It describes all sources of external influence coming from:

- Natural cosmic γ-radiation, muons, ...
- Calibration sources inside the spectrometer
- Radiation from the environment, e.g. from neighboring instruments

The beam facility PF1B inside the experimental hall *ILL 7* is surrounded by a number of experiments. The three closest to PERKEO III were:

- D1A: High-resolution two-axis diffractometer, close to detector 2
- D1B: Another two-axis diffractometer, close to detector 2
- IN11: Spin-echo spectrometer, close to detector 1

As expected, these experiments produce a noticeable number of background events (mostly γ-radiation), which were measured by the PERKEO III detectors. The signal to background ratio of the raw measured events was approximately 2:1. Besides the pure existence of this background, it is of course not constant over time, depending on the utilization of these experiments. Each beam facility has its own main-shutter to switch off the beam by blocking the neutrons before entering the corresponding experiment.

The states of the main-shutters are logged, so that a subsequent correlation analysis is possible. Figure 5.21 shows the influence of the status of the respective neighbor experiments on the number of measured background events for a period of about 36 hours. Whenever any experiment changes its shutter status, the background countrate responds noticeably. Table 5.8 correlates the closing of the main-shutters with the particular drop in background countrate. It also shows the total number of status changes for each experiment during the whole PERKEO III beamtime.

The maximum drop in countrate is about 50 % and dominated by experiment IN11, which has changed the status about 400 times during the PERKEO III beamtime. Here the benefit of having a pulsed beam comes fully into play. Since the chopper period is about 10 ms, the background is measured 100 times per second. The timing of the shutter movement of the neighbors is uncorrelated with the chopper period. Therefore, beam independent background is exactly

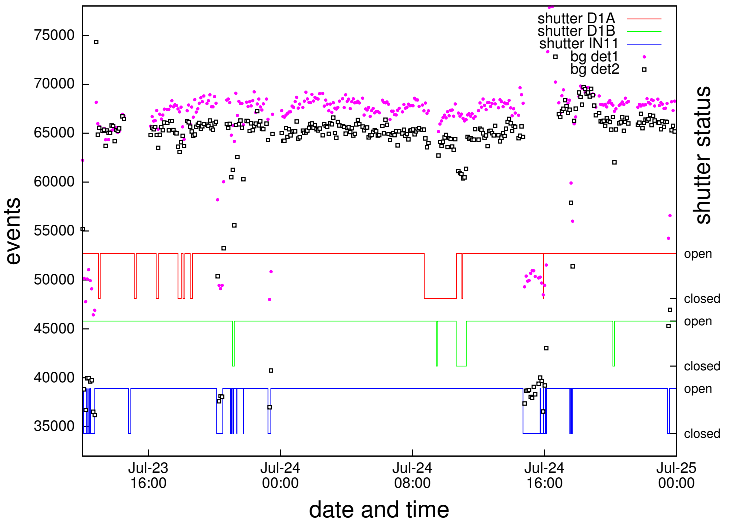

Figure 5.21: Number of background events measured with the PERKEO III detectors, together with the states of the main-shutters of the three neighbor experiments as function of time. Upper curve (red): D1A, middle (green): D1B, lower (blue): IN11. The strongest influence on the PERKEO III detectors is due to IN11.

Exp.	Background Drop Detector 1	 Detector 2	No. of Switches
D1A	2 %	8 %	450
D1B	2 %	4 %	1800
IN11	30 %	45 %	400

Table 5.8: Influence of the neighbor experiments on background, measured with the PERKEO III detectors.

accessible. To emphasize and confirm this, two disjoint datasets were prepared and analyzed:

- Dataset 1: Only data, when IN11 shutter has changed its status during the measurement, marked as *changed*
- Dataset 2: Only data, without any shutter-change at all (use same statistics), marked as *stable*

The statistics in these datasets are quite small compared to the whole measurement (about 4 %). For these two datasets the normalized asymmetry was derived and compared. The deviation is within the statistical range. Figure 5.22 shows this comparison for both detectors.

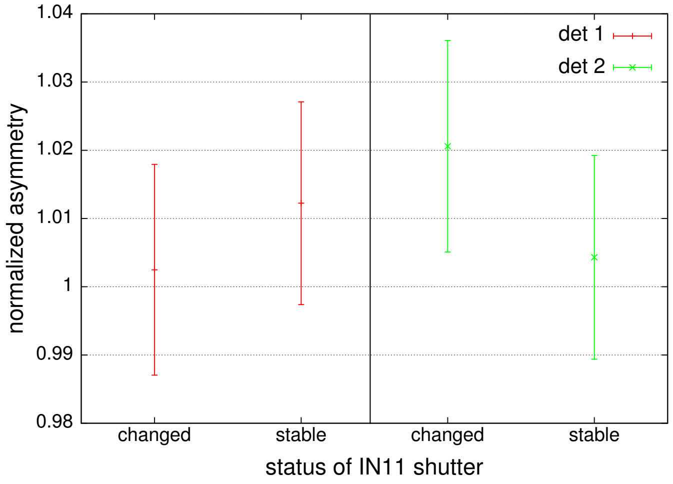

Figure 5.22: Normalized asymmetry on both detectors (left: det 1, right: det 2). The *changed* data contain measurements, when IN11 has switched the shutter, the *stable* data are free of any shutter change of the three neighbor experiments.

Finally, this result constitutes one of the major advantages of a pulsed neutron beam measurement, which strongly simplifies the determination of the beam independent background. In previous continuous beam measurements, data had to be discarded, if background conditions changed within a measurement period. This led to a considerable decrease of available statistics.

5.3.4 Spin Independence of Background

Using the measured spectra $S^{\uparrow,\downarrow}$ and $B^{\uparrow,\downarrow}$, there are two possible methods to derive the experimental asymmetry:

$$\begin{aligned} A_N &= \frac{N^{\uparrow} - N^{\downarrow}}{N^{\uparrow} + N^{\downarrow}} \qquad (5.54) \\ &\overset{(5.1)}{=} \frac{(S^{\uparrow} - r \cdot B^{\uparrow}) - (S^{\downarrow} - r \cdot B^{\downarrow})}{(S^{\uparrow} - r \cdot B^{\uparrow}) + (S^{\downarrow} - r \cdot B^{\downarrow})} \qquad \Rightarrow \\ A_S &\overset{B^{\uparrow}=B^{\downarrow}}{=} \frac{S^{\uparrow} - S^{\downarrow}}{S^{\uparrow} + S^{\downarrow} - r \cdot B} \,. \qquad (5.55) \end{aligned}$$

The assumption to get eq. (5.55) from (5.54) is that the background spectra are spin independent: $B^{\uparrow} = B^{\downarrow}$.

To test this, the deviation between these two experimental asymmetries is derived:

$$
\begin{aligned}
1 - \frac{\Delta A}{A}_{N,S} \equiv \frac{A_N}{A_S} &= \frac{N^{\uparrow} - N^{\downarrow}}{\cancel{N^{\uparrow} + N^{\downarrow}}} \cdot \frac{\cancel{S^{\uparrow} + S^{\downarrow} - r \cdot B}}{S^{\uparrow} - S^{\downarrow}} \\
&\overset{(5.1)}{=} \frac{(S^{\uparrow} - S^{\downarrow}) - r \cdot (B^{\uparrow} - B^{\downarrow})}{S^{\uparrow} - S^{\downarrow}} \\
&= 1 - \frac{r \cdot (B^{\uparrow} - B^{\downarrow})}{S^{\uparrow} - S^{\downarrow}} \equiv 1 - \delta A_S^N \,. \qquad (5.56)
\end{aligned}
$$

The plot in fig. 5.23 shows the deviation $\delta A_S^N(E)$ (full 83 Hz dataset) together with a constant fit in the energy range of about 250–700 keV. The effect is of the order $0.1(1.4) \cdot 10^{-3}$ and therefore compatible with zero. The uncertainly of this number is only limited by the total available statistics.

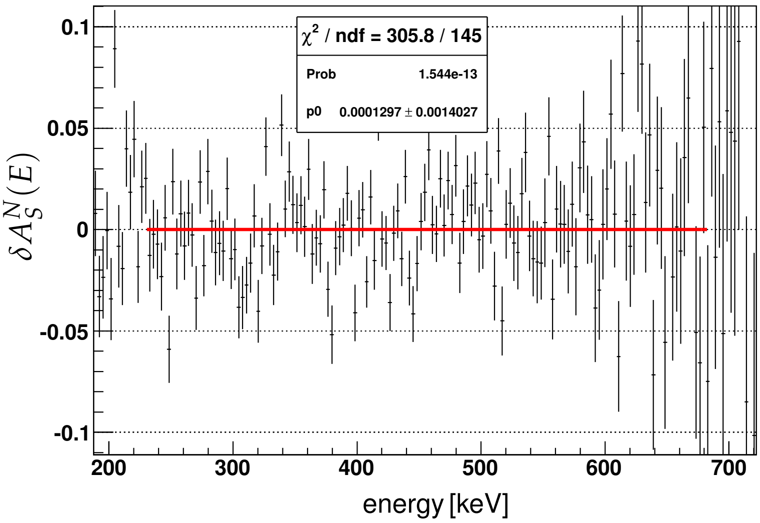

Figure 5.23: Effect of spin dependent background on experimental asymmetry. A constant fit (in red) gives an estimation for the function $\delta A_S^N(E)$ in the relevant energy range of about $0.1(1.4) \cdot 10^{-3}$, which is compatible with zero. Dataset: 83 Hz, detector 1. The effect is of similar order in the other datasets.

5.4 Correction of Detector Drift

To quantify aging effects of the detection system and the impact of measuring in an environment that is not temperature stabilized, the asymmetry measurement was interrupted once per hour to calibrate the detectors. These calibration data are used to rescale the spectra of each datafile separately, before adding to a dataset, see section 4.4.4 and fig. 4.6. The scaling factors are derived by a linear approximation between two consecutive drift measurements. The curves in fig. 5.24a show the relative position of the drift peak as well as the interpolated scaling factors as a function of time.

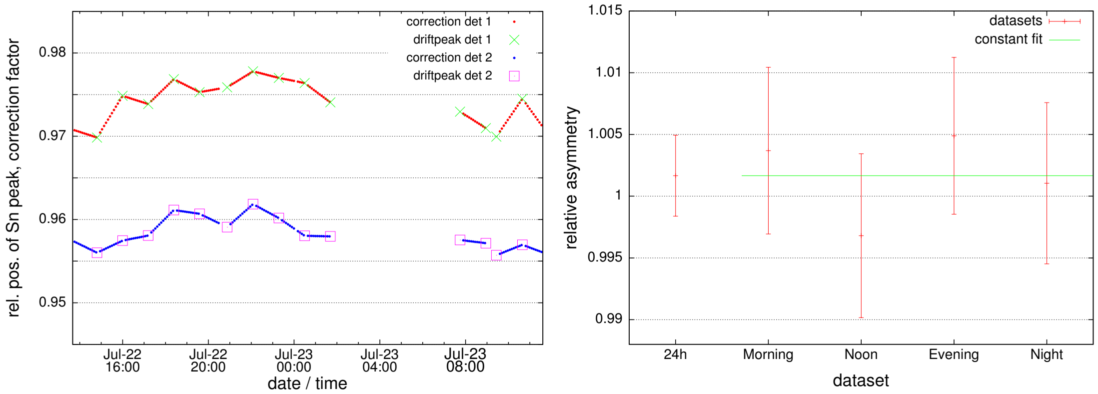

(a) Normalized measured scaling factors (dots) together with the 12 interpolated correction factors (lines), used to rescale the neutron decay data.

(b) Daytime dependence of the asymmetry A. A reduced χ^2 of 0.9/3 confirms that no daytime dependence is seen in the drift-scaled data.

Figure 5.24: Derived drift scaling factors (left) and effect of the drift-correction on the asymmetry of several daytime dependent datasets (right).

To verify the efficiency of this drift correction and to examine the general time dependent behavior of the neutron decay data, the following analysis was performed. The full 83 Hz dataset was split into four pieces:

1. *Morning*: data taken between 6–12 o'clock
2. *Noon*: data taken between 12–18 o'clock (maximum of drift)
3. *Evening*: data taken between 18–24 o'clock
4. *Night*: data taken between 0–6 o'clock (minimum of drift)
5. As a reference: the full 24 h dataset

The asymmetry A was derived for these four datasets as well as for the full dataset. Figure 5.24b shows the result of this analysis together with a constant fit. The results and observations are:

- The constant fit perfectly hits the asymmetry value of the full dataset
- Reduced $\chi^2 = 0.9/3 = 0.3 \quad \Rightarrow \quad$ probability $p = 0.83$

- No time-dependent structure was found

⇒ The correction of the drift works well

Uncertainty of Drift Correction

To estimate the remaining uncertainty of the drift correction, the asymmetry A was derived from two datasets: with and without the drift correction. The 2×4 compared datasets depend on the considered detector and the chosen chopper frequency of either 94 Hz or 83 Hz. Figure 5.25 presents this comparison. Note: the datasets do not show final values of A, since the corrections due to the magnetic mirror effect and the background, which are different for each dataset, are not applied.

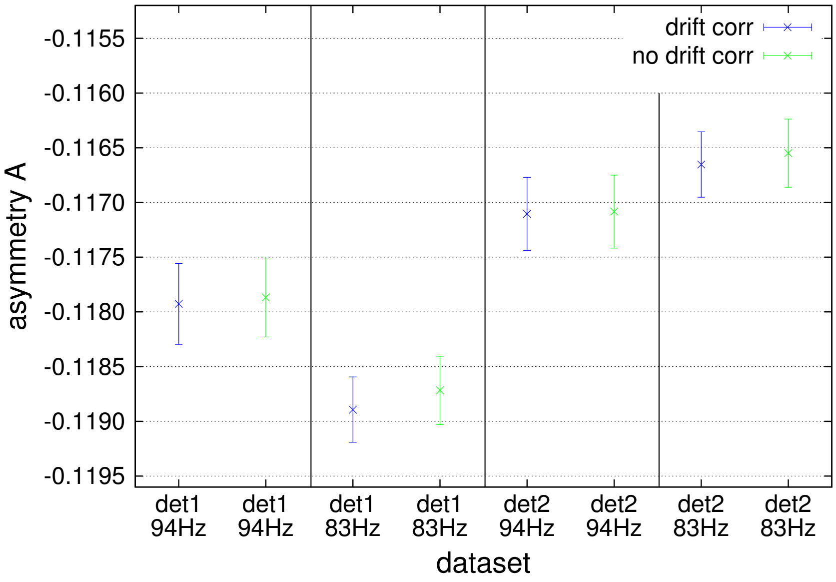

Figure 5.25: Results of the comparison analysis on the drift correction: blue vs. green data points. Note that the scatter of the individual pairs of asymmetry values is expected, since the necessary systematic corrections due to the magnetic mirror effect and the background are not applied.

The resulting uncertainty of the drift correction on the asymmetry A is:

$$\frac{\Delta A}{A}_{\text{drift}} = 4 \cdot 10^{-4} \,. \tag{5.57}$$

5.5 Deadtime Correction – Influence on Experimental Asymmetry *A(E)*

The deadtime of a detection system describes the time after the incidence of an event, during which the system is not able to record another event if it happens. This leads to a rate-dependent reduction of the measured countrate compared to the *real* number of events.

In the PERKEO III setup the deadtime is derived for each measurement cycle ($t_{\text{cycle}} = 10\,\text{s}$) by comparing the total number of periods of a 10 MHz quartz with the number, when system is *not busy*, see section 3.6.2.

The plot in fig. 5.26 shows the measured deadtime during the beamtime. The average deadtime is $\tau = 1.5(1)\ \mu\text{s}$. The slight variations are due to temperature drift and load of the read–out PC.

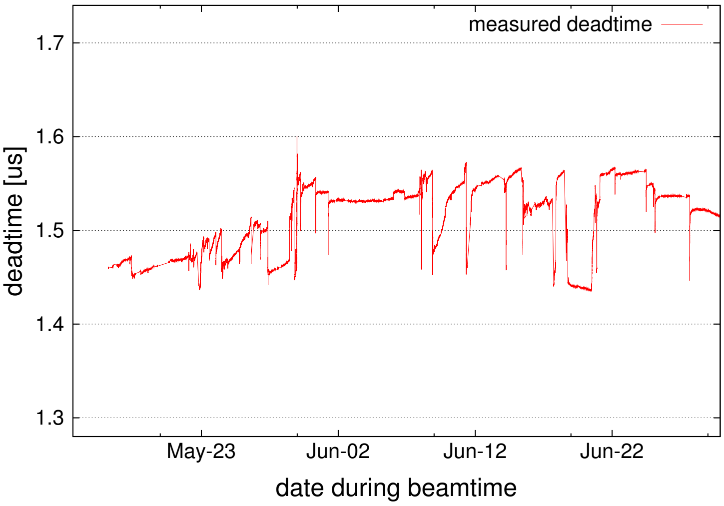

Figure 5.26: Evolution of the measured deadtime during the beamtime. The value used for the deadtime correction is $\tau_{\text{dead}} = 1.5(1)\ \mu\text{s}$.

To derive a pure signal spectrum, the background spectrum has to be subtracted from the measured signal, see definitions in eq. (5.1):

$$N^{\uparrow,\downarrow}(E) = S^{\uparrow,\downarrow}(E) - r \cdot B^{\uparrow,\downarrow}(E)\ . \tag{5.58}$$

Since the signal countrate is significantly different than the background countrate, the deadtime effects on signal and background are different as well.

Therefore, the simple subtraction in eq. (5.58) is not adequate. To describe the necessary corrections, some additional definitions to eq. (5.1) are required:

$$\begin{aligned} S^{\uparrow,\downarrow}, B^{\uparrow,\downarrow} &= \textit{measured}\text{ spectra, } B = B^{\uparrow} + B^{\downarrow} \\ S'^{\uparrow,\downarrow}, B'^{\uparrow,\downarrow} &= \text{deadtime corrected } \textit{real} \text{ spectra} \\ \delta S_k, \delta B_k &= \text{deadtime corrections for signal / background spectra} \\ m &= \textit{real} \text{ eventrate} \\ k &= \text{measured number of events} \\ T &= \text{measurement time } \Rightarrow\ k/T = \text{measured eventrate} \\ \tau &= \text{deadtime} \end{aligned} \tag{5.59}$$

With these definitions and eq. (5.14) from [Leo94], the *real* rate is:

$$m = \frac{k/T}{1 - (k/T)\,\tau}\,, \tag{5.60}$$

and the deadtime correction follows:

$$\begin{aligned} 1 + \delta_k \equiv \frac{m}{k/T} &= \frac{1}{1 - (k/T)\,\tau} \\ &\cong 1 + (k/T)\,\tau\,, \quad \text{with } \ (k/T)\,\tau = \mathcal{O}(10^{-3})\,. \end{aligned} \tag{5.61}$$

The experimental asymmetry $A(E)$ is defined as:

$$A(E) = \frac{N^{\uparrow} - N^{\downarrow}}{N^{\uparrow} + N^{\downarrow}} \overset{B^{\uparrow} = B^{\downarrow}}{=} \frac{S'^{\uparrow} - S'^{\downarrow}}{S'^{\uparrow} + S'^{\downarrow} - r \cdot B'}\,. \tag{5.62}$$

To simplify the calculation, the rates for $S'^{\uparrow,\downarrow}$ are assumed to be spin independent.[8] Therefore, the deadtime corrections can be factorized:

$$\begin{aligned} A(E) &= \frac{(1 + \delta S_k)(S^{\uparrow} - S^{\downarrow})}{(1 + \delta S_k)(S^{\uparrow} + S^{\downarrow}) - r \cdot (1 + \delta B_k) \cdot B} \\ &= \frac{S^{\uparrow} - S^{\downarrow}}{S^{\uparrow} + S^{\downarrow} - r \cdot \frac{1 + \delta B_k}{1 + \delta S_k} \cdot B}\,, \end{aligned} \tag{5.63}$$

---

[8] This assumption is true on a 10^{-2} level.

whereas the uncorrected asymmetry A_{uc} is:

$$A_{\mathrm{uc}}(E) = \frac{S^{\uparrow} - S^{\downarrow}}{S^{\uparrow} + S^{\downarrow} - r \cdot B} \,. \tag{5.64}$$

With corrections δS_k, δB_k of the order $\mathcal{O}(10^{-3})$, eq. (5.63) can be simplified with the following assumption:

$$\frac{1+\delta B_k}{1+\delta S_k} \cong 1 + \delta B_k - \delta S_k - \underbrace{\delta B_k \delta S_k}_{\mathcal{O}(10^{-6})} \cong 1 - (\delta S_k - \delta B_k) \,. \tag{5.65}$$

Now the effect on the asymmetry is:

$$\begin{aligned} 1 + \frac{\Delta A}{A}_{\mathrm{dead}}(E) \equiv \frac{A_{\mathrm{uc}}(E)}{A(E)} &= \frac{S^{\uparrow} + S^{\downarrow} - r \cdot (1 - (\delta S_k - \delta B_k)) \cdot B}{S^{\uparrow} + S^{\downarrow} - r \cdot B} \\ &= 1 + \frac{r \cdot (\delta S_k - \delta B_k) \cdot B}{S^{\uparrow} + S^{\downarrow} - r \cdot B} = 1 + \frac{\delta S_k - \delta B_k}{\frac{S^{\uparrow}+S^{\downarrow}}{r \cdot B} - 1} \,. \end{aligned} \tag{5.66}$$

Using the deadtime $\tau \cong 1.5(1)$ µs and the two average raw countrates for signal and background k^S/T and k^B/T, the corrections become:

$$k^S/T \cong 2.20(30)\ \mathrm{kHz} \quad \Rightarrow \quad \delta S_k = 3.3(5) \cdot 10^{-3} \quad \text{and} \tag{5.67}$$

$$k^B/T \cong 1.14(30)\ \mathrm{kHz} \quad \Rightarrow \quad \delta B_k = 1.7(5) \cdot 10^{-3} \,. \tag{5.68}$$

The plot in fig. 5.27 shows the energy dependent relative shift $\frac{\Delta A}{A}_{\mathrm{dead}}(E)$, when the deadtime effect is not corrected (dataset: 83 Hz, detector 1). With the given countrates, the effect is of the order $5 \cdot 10^{-4}$ in the energy range of about 250–700 keV, see constant fit. This value can also be estimated by using the signal–to–background ratio S/B, which is about 4 : 1 in the relevant energy range (see fig. 5.15). The estimation gives:

$$\frac{\Delta A}{A}^{\mathrm{est}}_{\mathrm{dead}} = \frac{\delta S_k - \delta B_k}{S/B - 1} = \frac{3.3(5) - 1.7(5)}{4.0(5) - 1} \cdot 10^{-3} \approx 5(2) \cdot 10^{-4} \,, \tag{5.69}$$

which is the same number compared with the result from the fit in fig. 5.27. To get the uncertainty of this number, the following has to be considered: the errors for the given signal and background countrates (eq. (5.67) and (5.68)) are strongly correlated, since countrate variations of the signal are mainly

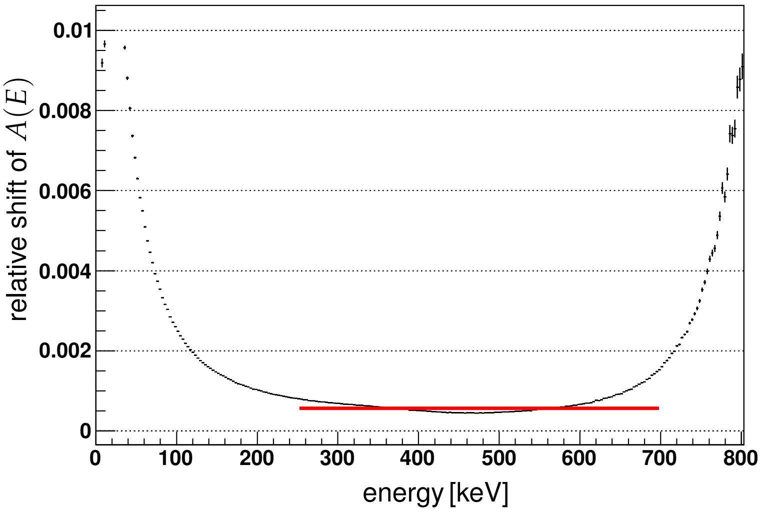

Figure 5.27: Relative shift of asymmetry $A(E)$, when deadtime is not corrected. A constant fit gives an estimation of the effect, which is of the order $5 \cdot 10^{-4}$. Used dataset: 83 Hz, detector 1. On detector 2 the effect is of similar order. The relative shift is a function of energy, since the signal to background ratio is energy dependent.

induced by background fluctuations, and therefore the absolute shift of signal and background countrate is the same in terms of direction and magnitude, see section 5.3.3.

5.6 Delta-Time Effect

The delta-time of an event is defined as the time interval of this event to the predecessor. Since radioactive decay follows:

$$\frac{\mathrm{d}N}{N} = -\frac{\mathrm{d}t}{\tau} \quad \Rightarrow \quad N(t) = N_0 \cdot \mathrm{e}^{-t/\tau} \,, \tag{5.70}$$

an exponential behavior of the number of events vs. delta-time is expected. The left plot in fig. 5.28 shows the measured neutron decay data (red) together with an exponential fit. Analyzing the delta-time revealed that for short delta-times the eventrate increases, depending on the previous event. The right plot in fig. 5.28 shows this dependence: if the previous event was on the same detector, the effect is visible (red), while no increase in eventrate is discovered, when the previous event was on the opposite detector (green). A fraction of 3 % of the events shows this behavior.

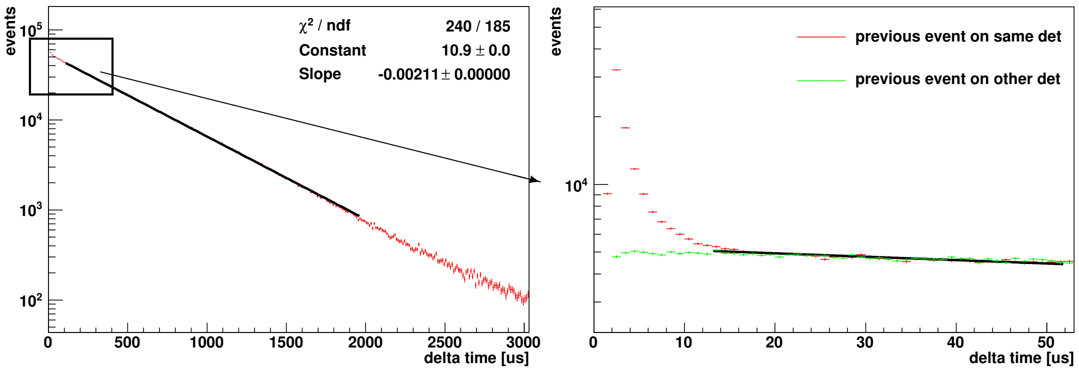

Figure 5.28: The left plot shows the expected exponential behavior on the delay time between successive electrons from neutron decay. A closer look to events with very small delta-times reveals a non-exponential increase of the eventrate, depending on which detector triggered the previous event.

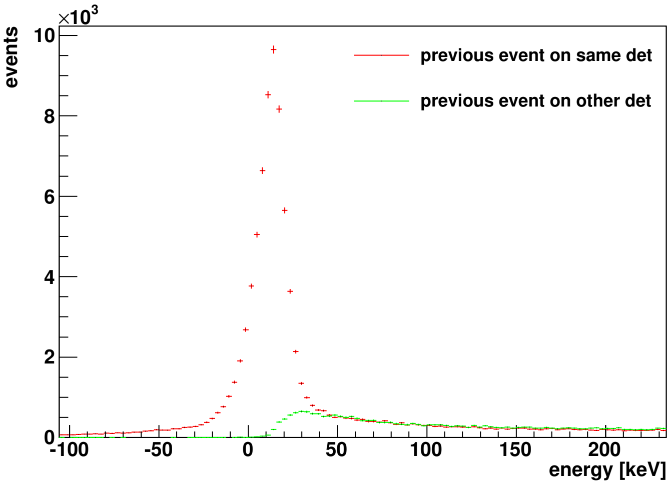

Figure 5.29: Spectra of events with a delta-time shorter than 10 µs. The difference of these two spectra shows that those events, which cause the increase in countrate in fig. 5.28, do not have energies above 30 keV.

To analyze this effect, the spectra of events with a delta-time shorter than 10 µs were inspected, see fig. 5.29. The energy of the additionally measured events is significantly below 50 keV. This suggests that just the data acquisition system was triggered and an energy value close to the pedestal was measured. This is possibly related to the already mentioned cross-talk at the discriminators, see section 4.4.5. A similar effect was also discovered during previous PERKEO measurements. As a consequence, in [Mun06] all events with delta-times < 10 µs were removed from the evaluation. This measure of course would directly influence the correction on asymmetry A due to the deadtime, see section 5.5 and eq. (5.69):

$$\tau_{\text{dead}} = 1.5\,\mu\text{s} \;\Rightarrow\; \frac{\Delta A}{A}_{\text{dead}} \approx 5 \cdot 10^{-4}\,, \tag{5.71}$$

$$\tau_{\text{dead}} = 10.0\,\mu\text{s} \;\Rightarrow\; \frac{\Delta A}{A}_{\text{dead}} \approx 3 \cdot 10^{-3}\,, \tag{5.72}$$

the deadtime correction would increase by a factor close to seven. To analyze the influence of the cross-talk events on the asymmetry, two datasets were prepared: dataset 1 including these events, dataset 2 with an applied deadtime cut of $\tau_{\text{dead}} = 10\,\mu\text{s}$. Both datasets were corrected with respect to the applied deadtime and then the beta-asymmetry was derived. A comparison showed a deviation of $\Delta A/A \approx 0.2(3.2)_{\text{stat}} \cdot 10^{-3}$. The variation of this number is about 15 times smaller than the derived statistical uncertainty on A. In conclusion, the uncertainty on the asymmetry A due to the observed cross-talk is less than

$$\frac{\Delta A}{A}_{\text{delta-time}} = 2 \cdot 10^{-4}\,. \tag{5.73}$$

5.7 Experimental Asymmetry

As defined in eq. (5.1), the experimental asymmetry is the normalized difference of the spectra with the two spin directions:

$$A_{\text{exp}}(E) = \frac{N^{\uparrow}(E) - N^{\downarrow}(E)}{N^{\uparrow}(E) + N^{\downarrow}(E)} \equiv \frac{\text{diff}(E)}{\text{sum}(E)}\,. \tag{5.74}$$

In fig. 5.30 the necessary steps to derive the asymmetry spectrum are presented. The measured spectra for signal and background $S(E)$ and $B(E)$ are shown in the upper left plot. The next plot presents the background subtracted spectra for the two spin states, followed by the spectra for diff(E) and the sum(E). The quotient of these spectra finally represents the experimental asymmetry, which is shown together with the fitfunction (red):

$$fit(E) = \frac{1}{2}\,A\,\beta(E)\,, \quad \text{with} \tag{5.75}$$

$$\beta(E) = \frac{|\mathbf{p}_{\text{e}}|}{E_{\text{e}}} = \frac{v(E)}{c} = \sqrt{1 - \left(\frac{m_{\text{e}}}{E + m_{\text{e}}}\right)^2}\,. \tag{5.76}$$

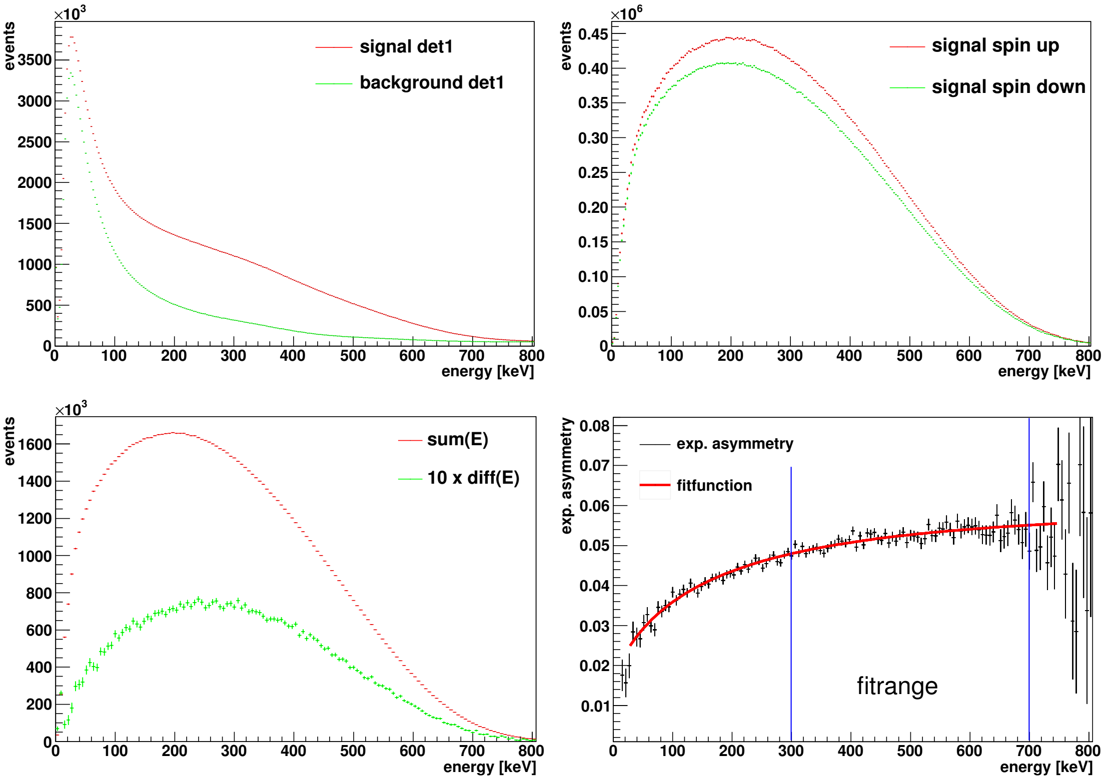

Figure 5.30: Derivation of experimental asymmetry $A(E)$. The two spectra, measured during the signal and background time windows $S(E), B(E)$, are shown in the upper left plot. Using the spin dependent and background corrected spectra $N^{\uparrow,\downarrow}$ (upper right), the resulting $\mathrm{sum}(E)$ and $\mathrm{diff}(E)$ spectra (lower left) are used to calculate the final experimental asymmetry spectrum, lower right.

Since the spectra are measured in units of *ch*, of course the energy to channel relation (section 5.1.1) has to be considered, when the experimental asymmetry is fitted to low energy regions.

Taking advantage of the $2\times2\pi$ symmetric magnetic field and detector design of PERKEO III, the experimental asymmetry could also be determined as follows:

$$A^{\uparrow}_{\mathrm{exp}}(E) = \frac{N^{\uparrow}_1(E) - N^{\uparrow}_2(E)}{N^{\uparrow}_1(E) + N^{\uparrow}_2(E)}\,, \tag{5.77}$$

using both detectors with the same neutron spin direction. The only advantage of this method is that no spinflipper is necessary. On the other hand the different detector functions and calibrations have a stronger influence on the final result, since both detectors are used in this method. As nowadays AFP spinflippers have efficiencies of unity [Sch07b], the method using spectra with different spin directions on the same detector is preferred, see eq. (5.74) .

5.7.1 Sensitivity of Asymmetry *A* on Offset and Gain

In the fit-tool *p3fit* the energy to channel relation maps the respective theoretical description of a function to a spectrum, which can be used to fit the particular data. The sensitivity of asymmetry A on the two strongly correlated parameters offset O and gain g is analyzed using two-dimensional parameter scans on constant confidence levels.

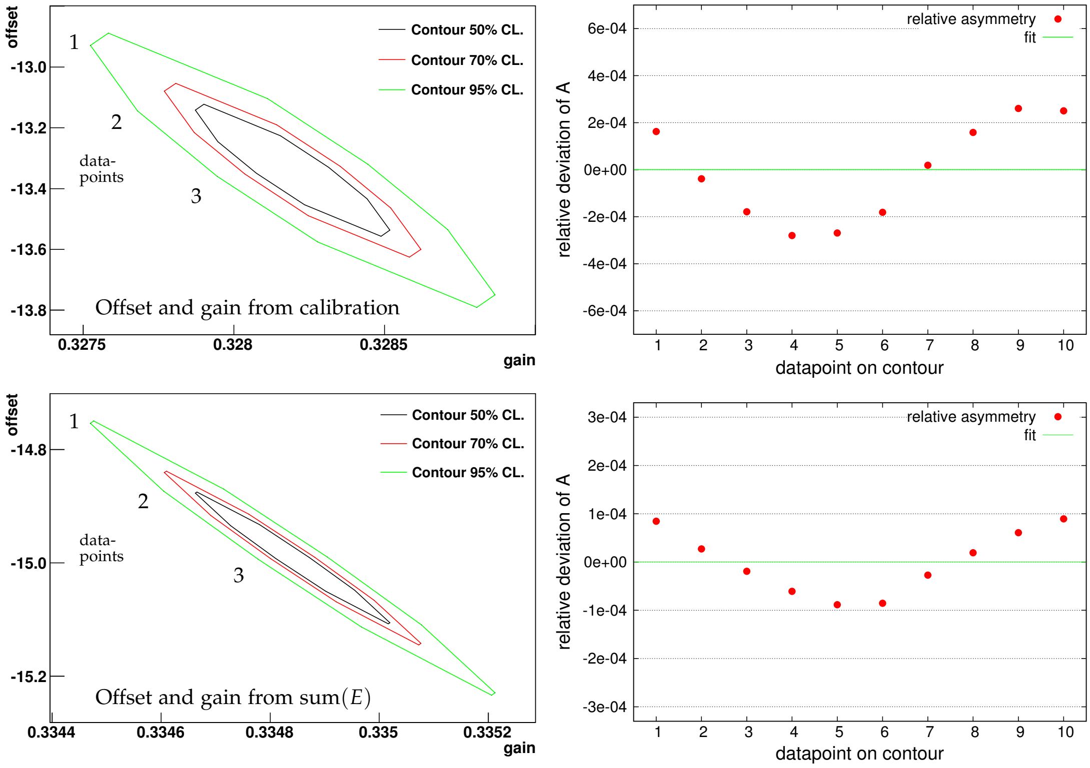

Figure 5.31: The left figures show 2-parameter scans with the free parameters offset O and gain g. The results of the 95 % confidence level ellipses were used as fix parameters to derive the asymmetry A, see right plot. In the upper analysis the two parameters are derived from 4-peak fits to a calibration set and the lower analysis tests the sensitivity of the neutron decay spectrum $\mathrm{sum}(E)$. The resulting relative uncertainties $\Delta A/A$ are $3 \cdot 10^{-4}$ and $1 \cdot 10^{-4}$.

Offset and gain can be derived from either the neutron decay spectrum $\mathrm{sum}(E)$ or from a simultaneous fit to the four calibration peaks. Both methods were

Data Source for Analysis	Variation of Gain, 95 % CL	Variation of Offset, 95 % CL	Resulting Effect on A
calibration	$\pm 2.3 \cdot 10^{-3}$	$\pm 3.3 \cdot 10^{-2}$	$\pm 3 \cdot 10^{-4}$
sum(E)	$\pm 1.2 \cdot 10^{-3}$	$\pm 1.7 \cdot 10^{-2}$	$\pm 1 \cdot 10^{-4}$

Table 5.9: Variations of gain g and offset O with resulting effect on asymmetry A.

applied in this analysis and the results are shown in fig. 5.31 and table 5.9. The variations of A are of the order $\mathcal{O}(3 \cdot 10^{-4})$ and $\mathcal{O}(1 \cdot 10^{-4})$, where the latter value corresponds to the method using the spectrum sum(E).

5.7.2 Asymmetry as Function of the Chosen Fitrange

In section 5.1.1 several approached are introduced to determine and describe the non-linear energy to channel relation of the detector for low energies. Widening the range of the fit to the experimental asymmetry $A_{\text{exp}}(E)$ to lower energies is expected to decrease the statistical error, when the *correct* non-linear approach is applied. To prove this assumption and to test the exponential non-linear approach, the correlation coefficient A is derived using three different fitranges: 200–700 keV, 250–700 keV and 300–700 keV. Table 5.10 shows the measured decrease of the uncertainty normalized to the fitrange of 300–700 keV.

Fitrange	Measured Rel. Uncertainty
300–700 keV	1
250–700 keV	0.97
200–700 keV	0.93

Table 5.10: Normalized measured decrease of the statistical uncertainty as function of the chosen fitrange.

In fig. 5.32 the derived values are shown for the three fitranges. Since the improvement in the statistical uncertainty is less than 10 % and the detector is assumed to be absolutely linear above 300 keV, the fitrange of 300–700 keV was finally used to determine the asymmetry A.

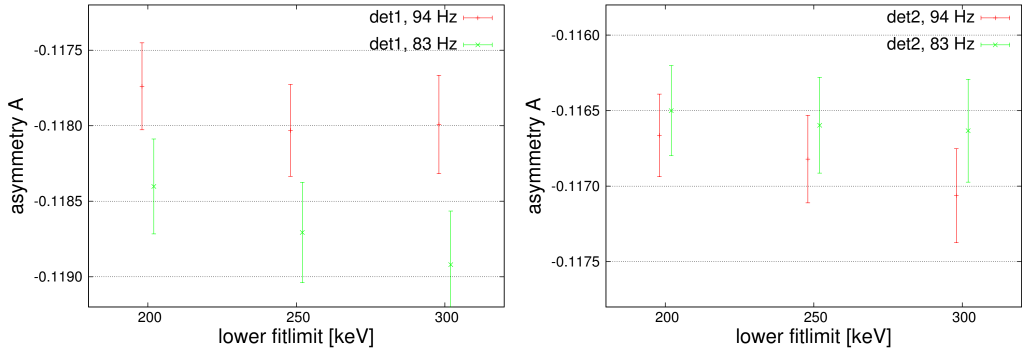

Figure 5.32: Derived asymmetry as function of the fitrange, which is used to fit the experimental asymmetry $A_{\mathrm{exp}}(E)$. The upper limit was fixed to 700 keV.

5.7.3 Final Derivation of the Asymmetry *A*

During the beamtime the detector was calibrated twice per day, see section 4.3. The neutron decay data, which were measured between two consecutive calibration measurements, were drift corrected and summed to one data subset. The asymmetry A was derived for each of these subsets, using offset O and gain g from the respective spectrum $\mathrm{sum}(E)$ and the number of photo-electrons PE from the subsequent detector calibration. The corrections due to the magnetic mirror and background depend on the particular detector and the chosen chopper frequency. Therefore, four packages of data-subsets were bundled and the respective asymmetry was derived with a constant fit.

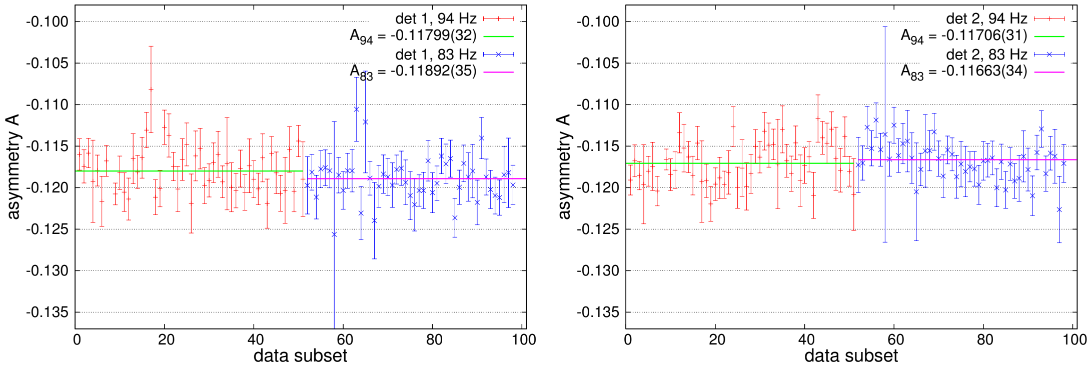

Figure 5.33: Derived asymmetries A for each of the data subsets together with a constant fit.

Figure 5.33 shows the four fits to the data subsets and table 5.11 lists the fitresults together with χ^2 and probabilities. In the last column the final values of the background corrected asymmetries A are presented.

Data	Asymmetry A	χ^2 / ndf	Prob.	Bg. Corr. A
det 1 94 Hz	-0.11799(32)	57 / 49	0.20	-0.11796(32)
det 1 83 Hz	-0.11892(35)	32 / 46	0.94	-0.11892(35)
det 2 94 Hz	-0.11706(31)	55 / 49	0.26	-0.11701(31)
det 2 83 Hz	-0.11663(34)	38 / 46	0.79	-0.11663(34)

Table 5.11: Derived asymmetry A with uncertainty, χ^2 and probability from a constant fit to the data subsets. The last column represents the background corrected values for A (table 5.6). Note: the correction due to the magnetic mirror is not applied here, see section 6.1.

Chapter 6

Final Results

In this chapter the results of the asymmetry measurement and the subsequent data analysis are presented. The data evaluation was performed blinded. Two major contributions of the expected systematic corrections were analyzed separately from the analysis presented in this thesis: the polarization $\mathcal{P}$ with spinflip efficiency $\mathcal{F}$ and the magnetic mirror correction, see section 3.3.1. The final unblinding of the data is planned for the scientific publication.

Hence, in this thesis these values are only estimated before further tests are performed. All systematic and statistic effects are collected and a preliminary value of the correlation coefficient A is derived. Using the V–A model, the coupling ratio λ and the CKM matrix element V_{ud} are determined. These are used to perform several tests on Standard Model unitarity and physics beyond. The hypothesis of right-handed currents is tested in section 6.3.2, while limits on scalar and tensor contributions are determined in section 6.3.3

Finally, the derived uncertainties on asymmetry A are compared with the most precise PERKEO II measurement and the latest result of the UCNA collaboration, section 6.4.

6.1 Determination of Correlation Coefficient *A*

The data analysis is blinded by the separate analysis of different evaluation aspects from different individuals of the PERKEO III collaboration. These aspects are:

- Neutron polarization $\mathcal{P}$ and spinflip efficiency $\mathcal{F}$,
- Magnetic mirror effect,
- Analysis of β-asymmetry from neutron decay, this thesis.

Since the blinded quantities are only estimated, the uncertainties of the assessments are of the order $\mathcal{O}(5 \cdot 10^{-3})$ (see below) and therefore almost three times as large as the statistical and systematical uncertainties of the final result, see table 6.2. This ensures the perpetuation of the blinded data analysis.

The value of the spinflip efficiency $\mathcal{F}$ is taken from [Sch07b], since the same spinflipper was used. The polarization $\mathcal{P}$ of a typical super-mirror polarizer at neutron wavelength $\lambda \cong 5\,\text{Å}$ is (e.g. [Rei99]):

$$\mathcal{P} = 98.7(4)\,\% \quad \text{and} \quad \mathcal{F} = 1.000^{(+0)}_{(-1)} \,. \tag{6.1}$$

The expected final uncertainties on these quantities for the PERKEO III measurement are [Sol11]:

$$\frac{\Delta\mathcal{P}}{\mathcal{P}} \leq 1 \cdot 10^{-3} \quad \text{and} \quad \frac{\Delta\mathcal{F}}{\mathcal{F}} \leq 1 \cdot 10^{-3} \,. \tag{6.2}$$

In [Wer09] a raw estimation is made to assess the magnetic mirror effect. The resulting correction on the asymmetry A is based on a calculated magnetic field and a Monte Carlo generated neutron beam profile:

$$\frac{M}{1-k^2} = 1 - 0.004(2) \,, \tag{6.3}$$

see also section 3.3.1 and eq. (3.37). The expected uncertainty on the magnetic mirror effect is [Mär11a]:

$$\frac{\Delta A}{A}_{\text{magn.}} \leq 8 \cdot 10^{-4} \,. \tag{6.4}$$

6.1.1 Asymmetry *A* Including Estimated Blinded Quantities

Table 6.1 presents the asymmetry A from table 5.11 with the applied corrections due to estimated polarization and magnetic mirror effect according to eq. (6.1) and (6.3). The given uncertainties on A include only statistics. **Note 1:** these values already contain the radiative corrections from eq. (2.25) [GT92]. **Note 2:** the scatter between the individual values is expected, since the final unblinding of the magnetic mirror effect is not done yet, see eq. (3.36).

Dataset	Asymmetry A
det 1 94 Hz	$-0.12010(32)_{\text{stat}}$
det 2 94 Hz	$-0.11913(35)_{\text{stat}}$
det 1 83 Hz	$-0.12108(31)_{\text{stat}}$
det 2 83 Hz	$-0.11875(34)_{\text{stat}}$
average	$-0.11977(16)_{\text{stat}}(60)_{\text{blind}}$

Table 6.1: Final asymmetry A from table 5.11 including the corrections due to the estimated values for polarization eq. (6.1) and magnetic mirror effect eq. (6.3).

6.1.2 Final Table of the Asymmetry Measurement

In table 6.2 all systematic effects including the respective uncertainties are listed and a preliminary value for the total uncertainty on A is given.

Effect on Asymmetry A	Relative Correction	Relative Uncertainty	Reference
$^{\bullet}$Polarisation $\mathcal{P}$	$\approx 1.3 \cdot 10^{-2}$	$\left.\right\}\leq 10 \cdot 10^{-4}$	eq. (6.2), prelim.
$^{\bullet}$Spinflip efficiency $\mathcal{F}$			
$^{\bullet}$Magn. mirror effect	$\approx 4 \cdot 10^{-3}$	$\leq 8 \cdot 10^{-4}$	eq. (6.4), prelim.
*Background	$-2.0 \cdot 10^{-4}$	$0.9 \cdot 10^{-4}$	tab. 5.6, 5.11
*Deadtime	$-5.0 \cdot 10^{-4}$	$2 \cdot 10^{-4}$	eq. (5.69)
*Detector drift		$4 \cdot 10^{-4}$	eq. (5.57)
*Detector calibration		$5 \cdot 10^{-4}$	eq. (5.25)
*Short gate time		$1.4 \cdot 10^{-4}$	eq. (5.49)
$^{\star\bullet}$Systematics	$\approx 1.8 \cdot 10^{-2}$	$\leq 14.6 \cdot 10^{-4}$	table 6.2
†Ext. radiative corr.	$9 \cdot 10^{-4}$	$5 \cdot 10^{-4}$	eq. (2.25)
*Statistics		$13.7 \cdot 10^{-4}$	table 6.1
Total	$\approx \mathbf{1.9 \cdot 10^{-2}}$	$\leq \mathbf{2.1 \cdot 10^{-3}}$	

Table 6.2: Corrections and uncertainties on the asymmetry A. The blinded quantities, marked with a $^{\bullet}$bullet, were estimated (see above) with an uncertainty of the order $\mathcal{O}(5 \cdot 10^{-3})$, which is about three times as large as the final uncertainty on A. The external radiative correction, emphasized with a †dagger, originates from theory [GT92]. The parts analyzed in this thesis are labeled with a *star.

The derived values for the asymmetry A and the coupling ratio λ are:

$$A_{\text{blind}} = -0.11977(18)_{\text{sys}}(16)_{\text{stat}}(60)_{\text{blind}} = -0.11977(25)(60)_{\text{blind}} , \tag{6.5}$$

$$\lambda_{\text{blind}} = -1.27620(50)_{\text{sys}}(44)_{\text{stat}}(161)_{\text{blind}} = -1.27620(67)(161)_{\text{blind}} . \tag{6.6}$$

6.2 Neutron Lifetime

The neutron lifetime is currently under discussion. The result published in [Ser05], which is not yet included in the PDG average [NG10], deviates by about 6σ from the world average, while the corresponding uncertainties are comparable:

$$\tau_{\text{PDG}} = 885.7(8)\text{ s} \quad \text{and} \quad \tau_{\text{Ser}} = 878.5(8)\text{ s} . \tag{6.7}$$

In [Mär11b, Kon10, DS11] a new average is proposed, which combines recent lifetime measurements, including the latest one [Pic10]:

$$\tau_{\text{ave}} = 881.8(1.4)\text{ s} . \tag{6.8}$$

The uncertainty of this number is scaled by 2.5 to account for the χ^2 of the average, according to the PDG standards. This value is used within this thesis.

6.3 Tests on the Standard Model and Physics Beyond

In chapter 2 the Standard Model and some extensions are briefly introduced. Since the assumed errors on the blinded quantities are nearly three times larger than the final uncertainty on asymmetry A, tests on Standard Model unitarity and physics beyond were performed with the value of the most precise PERKEO II measurement [Mun06] together with the uncertainty of this PERKEO III measurement. Therefore, the asymmetry A and the coupling ratio λ, used for further tests, are:

$$A_{\text{test}} = -0.11943(25) \quad \text{and} \quad \lambda_{\text{test}} = -1.27520(67) . \tag{6.9}$$

The tests in this section were solely done to illustrate the effect of the small uncertainty of this measurement. They will be finalized once the measurement is unblinded.

6.3.1 CKM Unitarity

The CKM matrix element V_{ud} can be derived using the value of λ in eq. (6.9), the new neutron lifetime in eq. (6.8) and the relation in eq. (2.17):

$$V_{\mathrm{ud}} = \left(\frac{4908.7(1.9)}{\tau_{\mathrm{ave}} \cdot (1 + 3\,\lambda^2)} \right)^{1/2} \quad \Rightarrow \tag{6.10}$$

$$V_{\mathrm{ud}}^{\mathrm{test}} = 0.9731(5)_\lambda(8)_\tau(2)_{\mathrm{theo}} = 0.9731(10)\ . \tag{6.11}$$

This value differs by about 1σ from the PDG average

$$V_{\mathrm{ud}}^{\mathrm{PDG}} = 0.97425(22)\ , \tag{6.12}$$

which is dominated by super allowed nuclear β-decay. According to eq. (2.8) the CKM unitarity can be tested using:

$$1 - \Delta = |V_{\mathrm{ud}}|^2 + |V_{\mathrm{us}}|^2 + |V_{\mathrm{ub}}|^2\ . \tag{6.13}$$

The values of the CKM matrix elements V_{us} and V_{ub} are derived from Kaon decay respectively semileptonic decay of B-mesons. The actual PDG values are:

$$V_{\mathrm{us}} = 0.2252(9) \quad \text{and} \quad V_{\mathrm{ub}} = 0.00389(44)\ . \tag{6.14}$$

An unitarity test using the two values of V_{ud} in eq. (6.11) and (6.12) gives:

$$\Delta_{\mathrm{test}} = 0.002(2) \quad \text{and} \quad \Delta_{\mathrm{PDG}} = 0.0001(6)\ . \tag{6.15}$$

The deviation from unity of this measurement as well as the PDG deviation are consistent with the Standard Model expectation.

6.3.2 Right-Handed Currents

To perform the analysis on right-handed currents and to determine limits on the associated parameters, at least three neutron decay observables including their uncertainties have to be used, see section 2.3.1. These three parameters are: ratio of axialvector to vector current λ', squared ratio of mass eigenstates of the W boson $\delta = (W_1/W_2)^2$ and mixing angle ζ. The comparison in fig. 6.1 uses the following two parameter sets.

Parameter Set	**Neutron Decay Observable** A	B	τ
PDG	$-0.1173(13)$	$0.9807(30)$	$885.7(8)$ s
NEW	$-0.11943(25)$	$0.9807(30)$	$881.8(1.4)$ s

Table 6.3: Parameter sets used for right-handed exclusion analysis. Note that asymmetry A in parameter set NEW is taken from eq. (6.9).

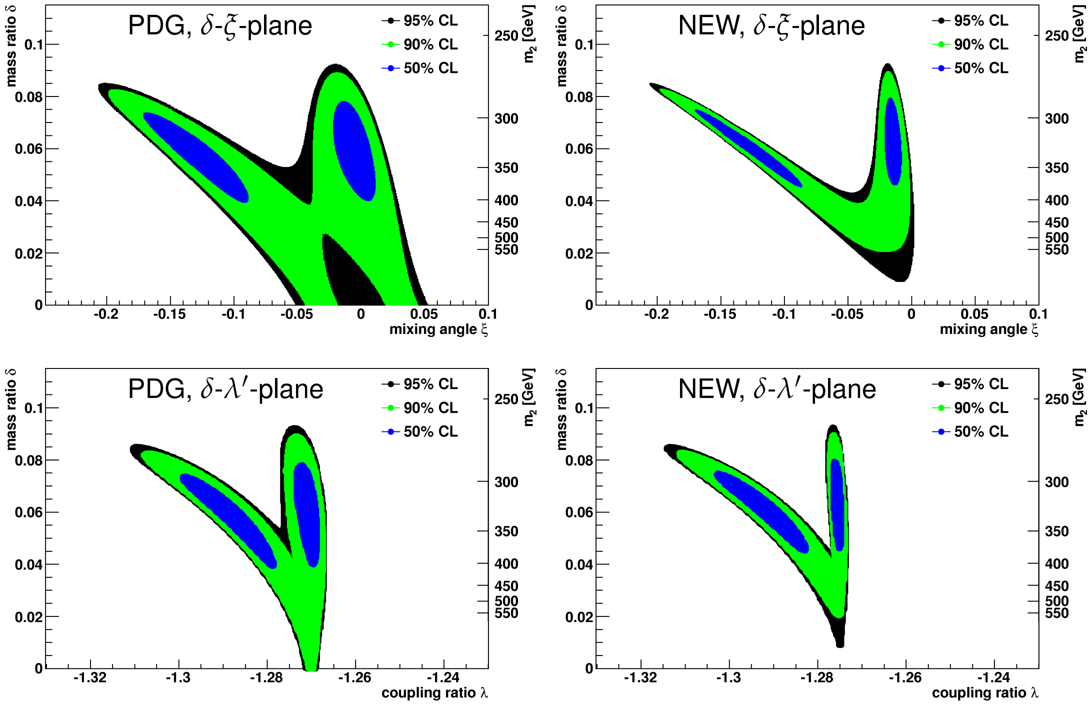

Figure 6.1: Exclusion plots for right-handed currents, projected to the δ-ξ-plane (upper plots) and to the δ-λ'-plane (lower plots). **Left:** parameter set PDG, **right:** parameter set NEW. With the new PERKEO III uncertainty on asymmetry A_{test} and the new neutron lifetime τ_{ave} the Standard Model (at $\delta = \xi = 0$) would be excluded on a 95 % CL (right).

In the parameter set PDG only values and uncertainties from [NG10] are used, see table 2.1. The parameter set NEW uses the asymmetry A_{test} from eq. (6.9), the neutron lifetime τ_{ave} from eq. (6.8) and the PDG value of B.

The exclusion plots in fig. 6.1 using the two parameter sets present projections to the δ-ξ-plane (upper plots) and to the δ-λ'-plane (lower plots). The Standard Model would be excluded in the parameter set NEW on a 95 % CL. However, without unblinding this measurement it is not justified to give precise limits on right-handed parameters.

6.3.3 Right-Handed Scalar- and Tensor-Interactions

The analysis on right-handed scalar and tensor contributions is described in section 2.3.2.2, see also [Sch07a, Abe09]. The two input parameter sets in table 6.3 were extended by the PDG values of the proton asymmetry C and the electron-neutrino correlation a, see table 2.1. The exclusion analysis was performed on the two parameter sets and compared. Figure 6.2 shows projections to the g_T/g_A-g_S/g_V-plane.

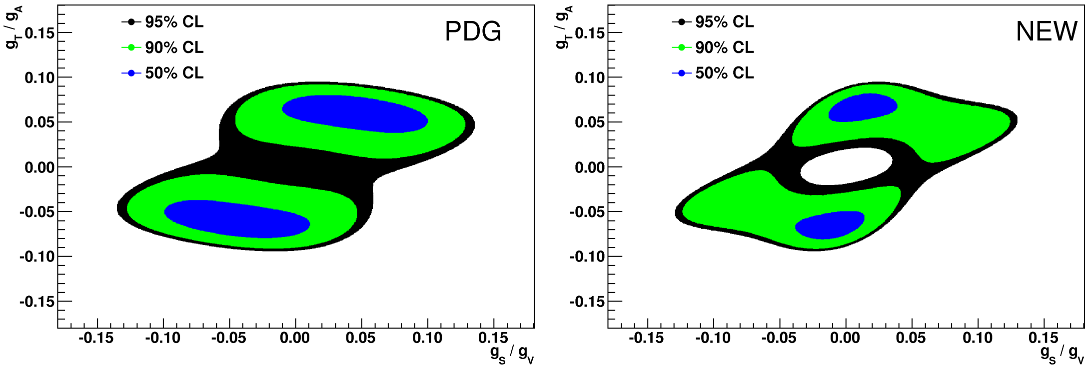

Figure 6.2: Exclusion plots for right-handed scalar and tensor interactions. **Left:** parameter set PDG, **right:** parameter set NEW, see table 6.3. Both parameter sets were extended by the PDG values of the proton asymmetry C and the electron-neutrino correlation a. The projections show that applying the new neutron lifetime τ_{ave} and the new PERKEO III uncertainty on asymmetry A, the Standard Model (at $g_T = g_S = 0$) would be excluded on a 95 % CL.

The exclusion plots in fig. 6.2 using the two extended parameter sets PDG and NEW present projections to the g_T/g_A-g_S/g_V-plane. Using the parameter set NEW, the Standard Model would be excluded on a 95 % CL, see right plot. Before precise limits on right-handed scalar and tensor interactions can be given, this asymmetry measurement has to be unblinded first.

6.4 Comparison with Previous Beta Asymmetry Measurements

In this section the derived uncertainties on the β-asymmetry A of this PERKEO III measurement are compared with recent results from the UCNA collaboration and measurements with the predecessor spectrometer PERKEO II.

6.4.1 Previous PERKEO II Measurement

In the past the spectrometer PERKEO II was used several times to measure the β-asymmetry A from mid of the 1990s to 2006 [Bae96, Abe97, Rei99, Abe02, Mun06]. Besides this, measurements to derive the neutrino asymmetry B and the proton asymmetry C were performed [Kre05a, Sch07b, Sch08]. The most precise measurements on these three neutron decay observables were performed with this spectrometer.

The most important differences between PERKEO II and PERKEO III are:

- In PERKEO II the magnetic field system is oriented perpendicular to the neutron beam.
- The symmetric detectors have a direct view to the calibration sources, which results in an additional contribution of γ-radiation in the measured calibration spectra.
- The magnetic field strength is about ten times higher in PERKEO II with the advantage of having smaller gyration radii of the electrons.
- The length of the decay volume is about ten times shorter in PERKEO II, $l \cong 20$ cm, which excludes a reasonable use of a pulsed neutron beam.

The last β-asymmetry measurement with PERKEO II as well as all previous measurements were performed with a continuous neutron beam. The measured average decay rate was about 300 Hz, which is comparable with the rate of this PERKEO III measurement, utilizing a pulsed neutron beam, see eq. (3.46). The corrections and uncertainties of the most precise measurement [Mun06] are taken from [Mär11a] and compared with the PERKEO III results of this measurement, see table 6.2:

Experiment	Systematic Corrections	Systematic Uncertainty	Statistical Uncertainty	Total Uncertainty
PERKEO II 2006	$0.9 \cdot 10^{-2}$	$2.1 \cdot 10^{-3}$	$3.8 \cdot 10^{-3}$	$4.3 \cdot 10^{-3}$
PERKEO III 2011	$\approx 1.9 \cdot 10^{-2}$	$1.5 \cdot 10^{-3}$	$1.4 \cdot 10^{-3}$	$2.1 \cdot 10^{-3}$

Table 6.4: Comparison between the most precise PERKEO II measurement and the new PERKEO III result. The total uncertainty is halved.

The new PERKEO III measurement halved the total uncertainty on asymmetry A compared with the most precise PERKEO II measurement.

6.4.2 Latest UCNA Result

The UCNA collaboration has developed an experimental program around the UCN source at Los Alamos National Laboratory's LANSCE facility (ultra cold neutrons, $E \leq 200\,\mathrm{neV}$). These neutrons are created via downscattering of a cold neutron beam from a spallation source in solid deuterium at $T = 5\,\mathrm{K}$. The same radioactive sources were used to calibrate a similar type of detector as in the PERKEO III setup.

The major systematic corrections and uncertainties result from geometric effects [Liu10]. The recently published result is:

$$A = -0.11966 \pm 0.00089^{+0.00123}_{-0.00140}\,, \tag{6.16}$$

with a total relative uncertainty of $1.4 \cdot 10^{-2}$. The following table compares the UCNA result with the new PERKEO III uncertainties.

Experiment	**Systematic Uncertainty**	**Statistical Uncertainty**	**Total Uncertainty**
UCNA 2010	$12 \cdot 10^{-3}$	$7.4 \cdot 10^{-3}$	$14 \cdot 10^{-3}$
PERKEO III 2011	$1.5 \cdot 10^{-3}$	$1.4 \cdot 10^{-3}$	$2.1 \cdot 10^{-3}$

In the PERKEO III measurement the asymmetry A is determined about seven times more precisely compared to the latest UCNA result.

Chapter 7

Summary and Outlook

In the decay of free polarized neutrons, the momenta of the decay products are correlated to the spin of the neutron. A precise determination of these correlations allows tests of the Standard Model or searches for physics beyond.

For years, experiments with spectrometers of the PERKEO family are at the forefront in terms of precision measurements of these neutron decay observables [Bop86, Bae96, Abe97, Rei99, Abe02, Kre05a, Mun06, Sch07b, Sch08].

In this thesis the latest PERKEO III measurement is described. The β-asymmetry correlation coefficient A was determined from data taken during a nine-month beamtime at the Institut Laue-Langevin in Grenoble, France. This beam facility provides the most intense cold neutron beam. For the first time, a pulsed neutron beam was applied in this kind of measurement. This was implemented to improve on systematic effects of continuous beam measurements.

Using a pulsed neutron beam allows to measure the neutron decay signal and the background simultaneously. It is no longer necessary to interrupt the neutron decay measurement to determine the background. Signal and background can be derived using separate time-cuts in the time of flight spectrum. In this way, beam independent ambient background is 100 % accessible. To confirm that beam related background is not an issue, numerous systematic tests were performed. The final background uncertainty was reduced to $\Delta A/A \leq 1 \cdot 10^{-4}$.

The response of a scintillation detector is not linear for energies below about 200 keV. In this thesis, several approaches were discussed to describe this intrinsic property. Due to lack of calibration information in the energy range 100 keV $< E <$ 300 keV, the experimental asymmetry spectrum $A_{\mathrm{exp}}(E)$ was excluded below 300 keV in the determination of the correlation coefficient A.

The detector uniformity, which measures the plane dependent detector response, could be improved to ±1 % over the whole used surface of the scintillation detector. This is an improvement of one order of magnitude compared to previous PERKEO measurements. The consequence is that the detector response on point-like beams like the radioactive calibration sources is the same compared with areal beams from neutron decay.

In total, the final systematic uncertainty on the asymmetry A decreased by about 40 % compared to the previously most precise measurement [Mun06] to $\Delta A/A = 1.5 \cdot 10^{-3}$. The total number of measured signal events was seven times larger in the new measurement, which reduced the statistical uncertainty by a factor of 2.7. The final total uncertainty on the β-asymmetry of $\Delta A/A = 2 \cdot 10^{-3}$ halved the uncertainty of the previously best measurement and is about $1/5$ of the uncertainty quoted by the PDG.

The still blinded result already confirms the previous measurements with spectrometer PERKEO II, see fig. 7.1. After unblinding the polarization $\mathcal{P}$ and the magnetic mirror effect, this β-asymmetry measurement will give the most precise value on neutron decay correlation coefficient A.

The dominant systematic uncertainties on the asymmetry A are, see table 6.2:

- Polarization: $\Delta A/A \leq 1 \cdot 10^{-3}$. This uncertainty is limited by statistics of the polarization measurement. The systematic uncertainty is due to a slightly inhomogeneous polarization on the beam profile. Using two polarizers in *crossed geometry* [Kre05b] improves not only the polarization $\mathcal{P}$ but also the systematic uncertainty. The feasible uncertainty of a ^{3}He polarization measurement is less than $1 \cdot 10^{-4}$, which was confirmed experimentally in November 2010 [Sol11].
- Magnetic mirror effect: $\Delta A/A \leq 8 \cdot 10^{-4}$. This uncertainty is linked to the precision of the magnetic field measurement and the temporal mapping of the chopper period to the data acquisition system. Further improvements will result in uncertainties less than $\Delta A/A \leq 4 \cdot 10^{-4}$ in PERKEO III measurements and $\Delta A/A \leq 1 \cdot 10^{-4}$ in the next instrument PERC, see section 7.3.
- Detector calibration: $\Delta A/A = 5 \cdot 10^{-4}$. To fit the asymmetry $A_{\mathrm{exp}}(E)$ to the non-linear region below 250 keV, more calibration information (additional sources) is needed in this particular energy range, e.g. ^{114}In.
- External radiative correction: $\Delta A/A = 5 \cdot 10^{-4}$. The theoretical calculations on external radiative correction were done in 1992 [GT92]. An update of these calculations would be preferable.

7.1 Classification of the Result

Figure 7.1 presents the results of the coupling ratio $\lambda = g_A/g_V$ derived from β-asymmetry measurements in the last 25 years. The data in blue are included in the current PDG average and the black datapoint [Abe08] combines the results of [Bae96, Rei99, Mun06]. In red the recent result of the UCNA collaboration is shown. On the right the result of this PERKEO III measurement is presented including two errorbars: the green one (smaller one) represents the total uncertainty of the measurement and the red one (larger one) emphasizes the still blinded corrections due to polarization $\mathcal{P}$ and magnetic mirror effect.

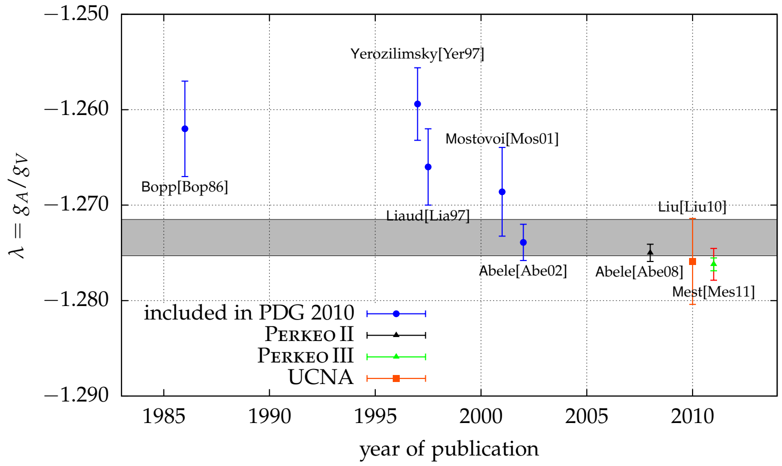

Figure 7.1: Ratio of axialvector to vector coupling λ, derived from β-asymmetry measurements [Bop86, Yer97, Lia97, Mos01, Abe02, Abe08, Liu10] and this measurement. The publications in blue are included in the current PDG average [NG10]. The result of [Abe08] combines three measurements with PERKEO II. The given value of this PERKEO III measurement has two errorbars: green for the total uncertainty of the measurement and red to emphasize the still blinded value.

7.2 Upcoming PERKEO III Measurement

The pulsed beam measurement with spectrometer PERKEO III was found to be very suitable in β-asymmetry measurements. Some future projects are conceivable: e.g. another continuous beam measurement to get access to the weak magnetism κ, or a proton asymmetry measurement.

Currently PERKEO III is used to study detector properties related to the new project PERC.

7.3 Future Project PERC

The next generation instrument PERC[1] is designed to improve the sensitivity of neutron decay studies by one order of magnitude, compared to actual and previous measurements. The charged decay products are collected by a strong longitudinal magnetic field of $B \approx 1.5\,\mathrm{T}$ directly from inside a neutron guide. This results in a high phase space density of decay products. A magnetic mirror at $B \approx 6\,\mathrm{T}$ serves to limit the phase space, which reduces related systematic errors. Due to the length of the decay volume of $l \cong 8\,\mathrm{m}$, decay rates of some 100 kHz are expected in continuous beam measurements. Systematic errors related to electron spectroscopy have been shown to be of the order of 10^{-4}, which is about one order of magnitude below that achieved today [Dub08a, Dub07].

The tools developed during this work will serve to support the analysis and studies on electron backscattering and non-linearity of the detector, which are necessary to achieve the aimed uncertainties.

PERC is under development by an international collaboration: PI Heidelberg, Atominstitut TU Wien, Uni Mainz, ILL Grenoble and Physik-Department E18 TU München. At present, the commissioning of this new spectrometer is planned for 2013. It will be set up at the beam site MEPHISTO of the Forschungs-Neutronenquelle Heinz Maier-Leibnitz (FRM II), München. A schematic of PERC is shown in fig. 7.2.

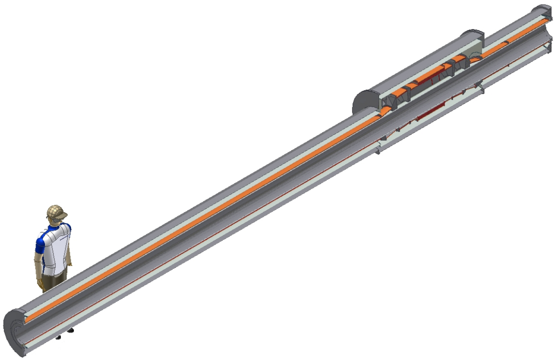

Figure 7.2: Schematic of the new project PERC. The neutrons decay in a $l = 8\,\mathrm{m}$ decay volume inside a non-magnetic neutron guide. Using a couple of tilted solenoids, the charged particle beam is routed away from the neutron beam and back to the original axis behind the neutron beam stop [Hor11].

---

[1] Proton Electron Radiation Channel, see http://www.physi.uni-heidelberg.de/../PERC/.

Appendix A

Theoretical Attachments

A.1 Lagrangian Density of the Electroweak Interaction

The full Electroweak Lagrangian density is:

$$\begin{aligned}\mathcal{L} = & \underbrace{\sum_i \overline{\psi}_i (\mathrm{i}\gamma^\mu \partial_\mu - m_i)\psi_i}_{\mathcal{L}_{\text{Dirac}}} \underbrace{-e\sum_i q_i \overline{\psi}_i \gamma^\mu \psi_i A_\mu}_{\mathcal{L}_{\text{em}}} \\ & \underbrace{-\frac{g}{2\sqrt{2}} \sum_i \overline{\psi}_i \gamma^\mu (1-\gamma_5)(T^+ W^+ + T^- W^-)\psi_i}_{\mathcal{L}_{\text{weak, charged}}} \\ & \underbrace{-\frac{g}{2\cos\theta_W} \sum_i \overline{\psi}_i \gamma^\mu (g_V^i - g_A^i \gamma_5)\psi_i Z_\mu}_{\mathcal{L}_{\text{weak, uncharged}}} \\ & \underbrace{-\sum_i \overline{\psi}_i \frac{g m_i H}{2 m_W} \psi_i}_{\mathcal{L}_{\text{Higgs}}} \ . \end{aligned} \tag{A.1}$$

A.2 Phase Space Factor

The phase space factor (density of states) $F(E)$ is derived using:

$$\mathrm{d}n = \frac{\mathrm{d}^3\mathbf{p}}{4\,\pi}\,\frac{\mathrm{d}^3\mathbf{q}}{4\,\pi} \quad \text{with} \tag{A.2}$$

$$\mathrm{d}^3\mathbf{P} \ll \mathrm{d}^3\mathbf{p},\, \mathrm{d}^3\mathbf{q}\ , \tag{A.3}$$

where $\mathbf{p}$, $\mathbf{q}$ and $\mathbf{P}$ denote the momenta of electron, electron neutrino and proton. Using:

$$\begin{aligned} p^2 &= (E + m_\mathrm{e})^2 - m_\mathrm{e}^2 \quad \Rightarrow && \text{(A.4)} \\ p\,\mathrm{d}p &= (E + m_\mathrm{e})\,\mathrm{d}E\ , && \text{(A.5)} \end{aligned}$$

and assuming massless neutrino:

$$\begin{aligned} \mathrm{d}^3\mathbf{q} &= 4\,\pi\,q^2\,\mathrm{d}q \overset{m_\nu \cong 0}{\longrightarrow} 4\,\pi\,(E_0 - E)^2\,\mathrm{d}E_0 \quad \text{and} && \text{(A.6)} \\ \mathrm{d}^3\mathbf{p} &= 4\,\pi\,p^2\,\mathrm{d}p = 4\,\pi\,(E + m_\mathrm{e}) \cdot \sqrt{(E + m_\mathrm{e})^2 - m_\mathrm{e}^2}\ \mathrm{d}E\ , && \text{(A.7)} \end{aligned}$$

with E and E_0 denoting the kinetic and the endpoint energy of the electron and m_e being the electron mass. Now the phase space factor becomes:

$$\frac{\mathrm{d}n}{\mathrm{d}E} \equiv F_\mathrm{theo}(E) = (E_0 - E)^2 \cdot (E + m_\mathrm{e}) \cdot \sqrt{(E + m_\mathrm{e})^2 - m_\mathrm{e}^2}\ . \qquad \text{(A.8)}$$

Appendix B

Attachments to Experimental Setup

B.1 Polarization with a ^{3}He Cell

An alternative to a super-mirror polarizer (section 3.1.3) is the polarization with a ^{3}He-cell as opaque spin filter [Zim99, Sur97]. The absorption cross section of the ^{3}He nucleus is strongly spin dependent, hence this cell is transparent only for neutrons with the appropriate spin direction. A drawback is that this property depends on the wavelength of the neutrons and the pressure of the helium gas. Another challenge is the limited lifetime and therefore polarization efficiency of a polarized helium cell, which is also sensitive to external magnetic fields. Thus, this method is only suitable for very narrow wavelength distributions. The polarization $\mathcal{P}$ can be increased up to unity, while transmission gets very low. Nevertheless, polarized ^{3}He is an ideal tool for the determination and analysis of the polarization $\mathcal{P}$ of a neutron beam.

B.2 Fermi Chopper

Figure B.1 shows a schematic of a Fermi Chopper (see section 3.4.2). Depending on the angle of the rotating chopper to the incoming neutron beam, the particles get either transmitted or absorbed.

B.3 Photomultipliers

A photomultiplier is a device, which converts an optical signal (photon) to an electrical signal. The conversion is realized by a photo-sensitive cathode with a defined quantum efficiency (probability of creating a photo-electron from one

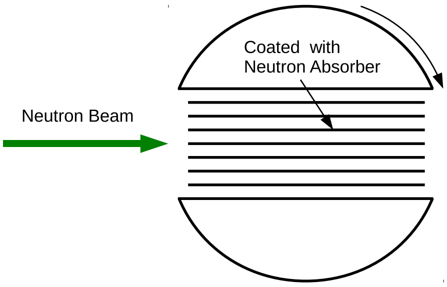

Figure B.1: Schematic of a Fermi Chopper. The parallel blades are made of a neutron absorber.

incident photon). The generated small number of electrons is amplified by a structure of several dynodes, which are connected to a descending high-voltage cascade. Finally the electrical signal is coupled out of the vacuumed tube.

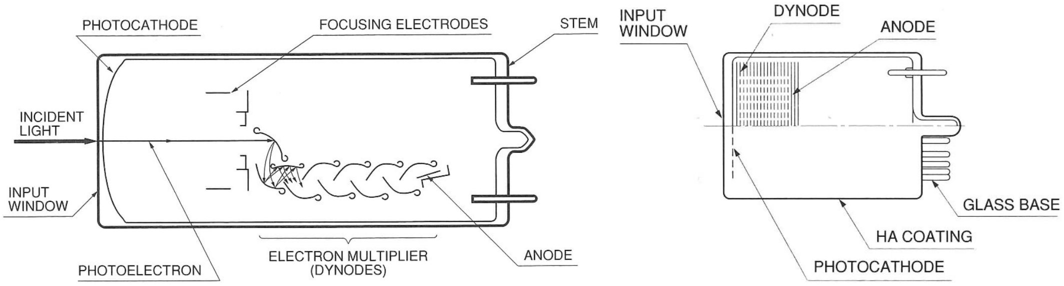

Figure B.2: Left: Conventional dynode type of a photomultiplier. The incoming photons reach the first dynode, are multiplied and reflected to the second dynode and so on. This type is sensitive on external magnetic fields. **Right:** Mesh dynode type. The several mesh dynodes are arranged in parallel. Because of the large number of mesh dynodes and the dense parallel arrangement, the sensitivity on external magnetic field is strongly decreased – mesh photomultipliers work in fields up to 1 T. The schematics are taken from Hamamatsu datasheets.

The left schematic in fig. B.2 shows this type of photomultiplier. However, this conventional dynode structure is sensitive to external magnetic fields, since the Lorentz force acts on electrons during their motion between the dynodes. As an alternative the so-called Mesh-photomultiplier can be used in such environments, see right schematic in fig. B.2. Here the dynodes are arranged in parallel and very close to each other, so that the sensitivity on external magnetic fields can be strongly decreased.

B.4 Electrical Power Supply

The electrical power supply for the magnetic field system of PERKEO III was realized by two modules from company Danfysik with the following characteristic data:

- Type: MPS855 System 8500
- $U_{\max} = 300\,\mathrm{V}$, $I_{\max} = 600\,\mathrm{A}$, $P_{\max} = 180\,\mathrm{kW}$
- Stability class: 100 ppm for long / short term drift
- Load regulation: $< 0.5\,\mathrm{ppm}$ for $\pm 10\,\%$ resistance change
- Output voltage ripple: $< 1\,\%$ of U_{out}
- Temperature coeff.: ambient 0.2 ppm/K, cooling water 0.05 ppm/K
- Cooling water temperature: $T = 15$–$35\,^{\circ}\mathrm{C}$
- Cooling water flow: 32 l/min

One module was connected to the solenoids of the decay volume, whereas the other one supplied the magnetic field of the two detector vessels of PERKEO III. The output power of both modules was set to: $P_{\mathrm{rel}} = 90\,\% \mathrel{\widehat{=}} I = 540\,\mathrm{A}$, which was necessary to have a magnetic field of $B \cong 150\,\mathrm{mT}$ in the decay volume. As part of the monitoring system the water flux to cool these modules was observed, see section 4.1.

Two additional power supply modules were necessary for the various correction coils (see section 3.3.1 and 4.4.1).

B.5 Cooling

Several parts of the experimental setup were included in the cooling setup:

- Magnetic field system of PERKEO III,
- Two main power supply modules,
- Turbo pumps,
- Electronics cabinet.

The reactor of the ILL as well as the several experiments are cooled, using the water of the river *Drac*. Since water of the primary cooling circuit must not be poured back to the river, a special heat exchange circulation pump was used.

The water flow in every single cooling circuit was observed using a monitoring system, which was able to switch off the electrical power supply in case of any incident. Figure B.3 shows a schematic of the installed cooling framework at the magnetic field system of PERKEO III.

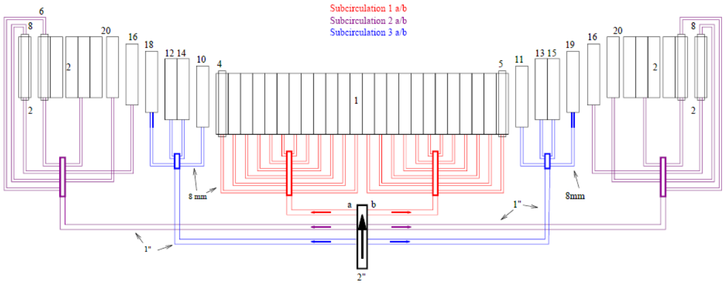

Figure B.3: Cooling schematic of the PERKEO III solenoid system. The water was distributed to six subcircuits, which were monitored separately [Kap07].

B.6 Decay Scheme of Copper

The attached figures describe the decay schemes of natural copper (69.2 % of ^{63}Cu + 30.8 % of ^{65}Cu) after activation due to absorption of a neutron.

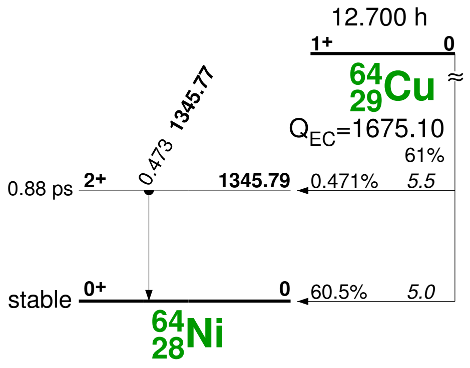

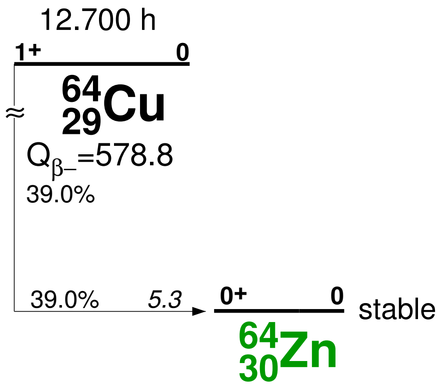

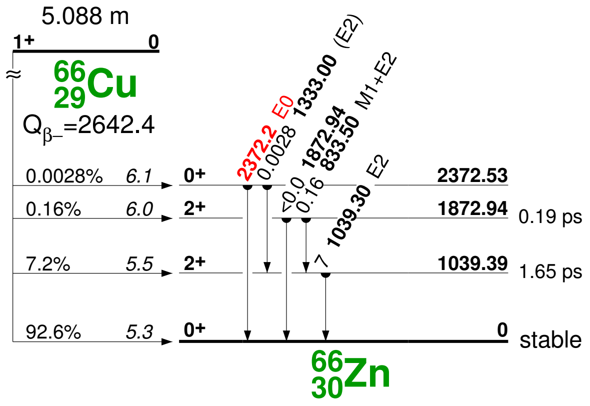

Figure B.4: Decay schemes of ^{64}Cu ($t_{1/2} = 12.7\,\mathrm{h}$) and ^{66}Cu ($t_{1/2} = 5.1\,\mathrm{min}$) from [Fir96].

B.7 Theoretical Descriptions of Calibration Spectra

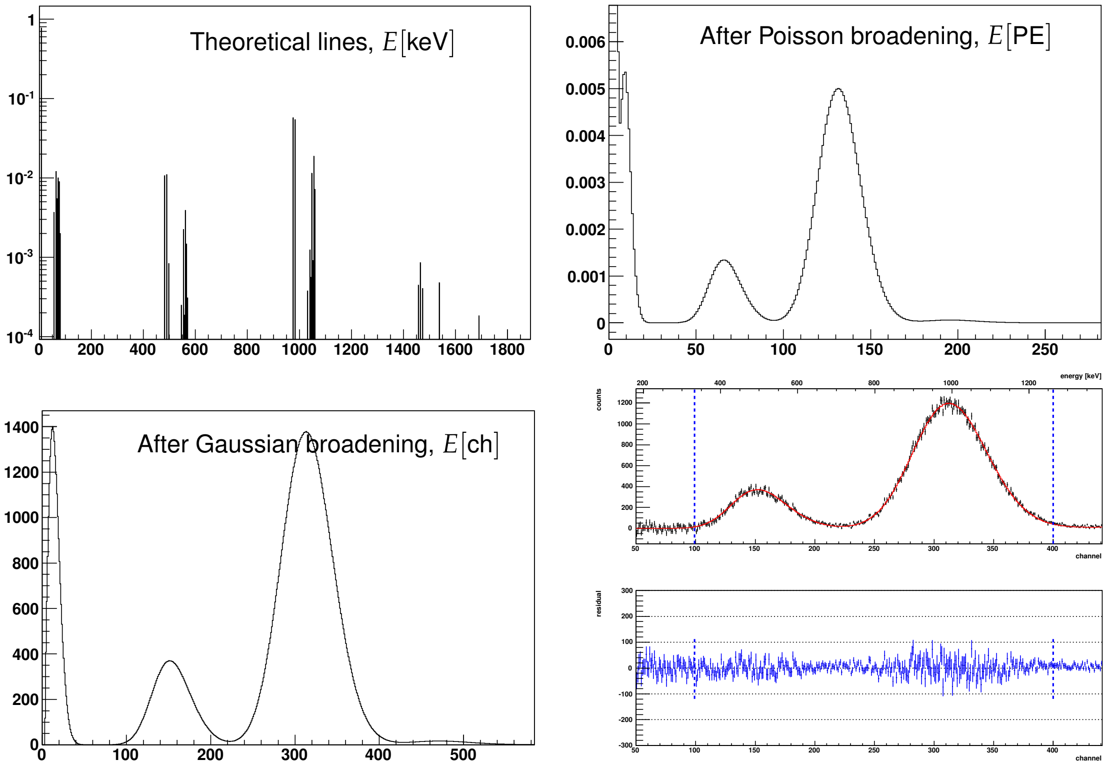

Figure B.5: Evolution from the theoretical description of the calibration source ^{207}Bi (upper left) via Poisson and Gaussian broadening to the function, used to fit the measured date (red, lower right). The residual spectrum (blue) shows no structure in this quite broad energy fit.

The theoretical descriptions of the calibration spectra, used by the fit-program *p3fit*, are described for the example source ^{207}Bi. Starting with the line spectrum (upper left plot in fig. B.5), several broadening functions and the trigger function are applied (see section 3.3.2) until the spectrum can be used to fit the measured data (lower right plot). The residual spectrum of this fit is rather flat without any structure. The used theoretical description of the energy lines together with the intensities follow in table B.1.

Table B.1: Energy lines of ^{207}Bi, resulting from all possible combinations of conversion electrons with Auger electrons, from updated database, see also [Roi10].

Electrons	**Energy [keV]**	**Intensity**
LMM	8.156	46.1803
KLL	56.352	0.222643
KLL+LMM	64.508	0.729611
KLM	68.362	0.327796
KLL+2LMM	72.664	0.597742
KLM+LMM	76.518	0.537102
KMM	80.372	0.12059
K(1,0)	481.623	0.636108
K(1,0)+LMM	489.779	0.659384
K(1,0)+2LMM	497.935	0.0503811
K(1,0)+KLL	537.975	0.00436745
K(1,0)+KLL+LMM	546.131	0.0148274
K(1,0)+KLM	549.985	0.00643017
L(1,0)	553.839	0.135627
K(1,0)+KLL+2LMM	554.287	0.0134133
K(1,0)+KLM+LMM	558.141	0.0112943
L(1,0)+LMM	561.995	0.233494
K(1,0)+KMM	561.995	0.00236553
K(1,0)+KLL+3LMM	562.443	0.00138276
M(1,0)	565.849	0.088119
K(1,0)+KLM+2LMM	566.297	0.00124248
L(1,0)+2LMM	570.151	0.0184588
M(1,0)+LMM	574.005	0.00731935
K(2,0)+LMM	817.876	0.00112253
K(3,1)	975.585	3.43829
K(3,1)+LMM	983.741	3.27851
K(3,1)+KLL	1031.94	0.0226613

Continued on next page

Table B.1 – continued from previous page

Electrons	Energy [keV]	Intensity
K(3,1)+KLL+LMM	1040.09	0.0742622
K(3,1)+KLM	1043.95	0.0333642
L(3,1)	1047.8	0.685139
K(3,1)+KLL+2LMM	1048.25	0.0608402
K(3,1)+KLM+LMM	1052.1	0.054668
K(3,1)+KMM	1055.96	0.012274
L(3,1)+LMM	1055.96	1.12262
M(3,1)	1059.81	0.432544
K(1,0)+K(3,1)	1457.21	0.0268305
K(1,0)+K(3,1)+LMM	1465.36	0.0511674
K(1,0)+K(3,1)+2LMM	1473.52	0.0243948
K(1,0)+K(3,1)+KLL+LMM	1521.72	0.00149624
L(1,0)+K(3,1)	1529.42	0.00572065
K(1,0)+L(3,1)	1529.42	0.00534646
K(1,0)+K(3,1)+KLL+2LMM	1529.87	0.00205467
K(1,0)+K(3,1)+KLM+LMM	1533.73	0.00134971
L(1,0)+K(3,1)+LMM	1537.58	0.0148282
K(1,0)+L(3,1)+LMM	1537.58	0.0138583
M(1,0)+K(3,1)	1541.43	0.00371679
K(1,0)+M(3,1)	1541.43	0.00337534
L(1,0)+K(3,1)+2LMM	1545.74	0.00893783
K(1,0)+L(3,1)+2LMM	1545.74	0.00835319
M(1,0)+K(3,1)+LMM	1549.59	0.00354407
K(1,0)+M(3,1)+LMM	1549.59	0.00321849
L(1,0)+L(3,1)	1601.64	0.00113994
L(1,0)+L(3,1)+LMM	1609.8	0.00373564
L(1,0)+L(3,1)+2LMM	1617.95	0.00306046
M(1,0)+L(3,1)+LMM	1621.81	0.00121355
L(1,0)+M(3,1)+LMM	1621.81	0.0011792
K(4,1)	1682.16	0.0067606
K(4,1)+LMM	1690.32	0.0110343
K(4,1)+2LMM	1698.48	0.00437465
L(4,1)+LMM	1762.54	0.00195803
K-Auger	61.5861	2.85378
KLL	56.352	1.7453
KLM	68.362	0.973247
KMM	80.372	0.135229

Continued on next page

Table B.1 – continued from previous page

Electrons	Energy [keV]	Intensity
LMM	8.156	54.6037
K	481.623	1.54794
L	553.839	0.429277
M	565.849	0.105706
K	809.72	0.0023497
L	881.936	0.000392477
M	893.946	9.16639e-05
K	975.585	7.12343
L	1047.8	1.84626
M	1059.81	0.441757
K	1354.07	0.00035638
L	1426.28	6.15446e-05
M	1438.29	1.44393e-05
K	1682.16	0.0235117
L	1754.38	0.00382237
M	1766.39	0.00088822

Bibliography

[Abe02] Hartmut Abele et al. “Is the Unitarity of the Quark-Mixing CKM Matrix Violated in Neutron β-Decay?” In: *Phys. Rev. Lett.* 88.21 (2002), p. 211801.

[Abe06] Hartmut Abele et al. “Characterization of a ballistic supermirror neutron guide”. In: *Nuclear Instruments and Methods A* 562 (2006), pp. 407–417.

[Abe08] Hartmut Abele. “The neutron. Its properties and basic interactions”. In: *Progress in Particle and Nuclear Physics* 60.1 (2008), pp. 1–81.

[Abe09] Hartmut Abele. “The neutron alphabet: Exploring the properties of fundamental interactions”. In: *Nuclear Instruments and Methods A* 611 (2009), pp. 193–197.

[Abe97] Hartmut Abele et al. “A measurement of the beta asymmetry A in the decay of free neutrons”. In: *Physics Letter B* 407 (1997), p. 212.

[Ahm04] S. Ahmed et al. “Measurement of the Total Active ^{8}B Solar Neutrino Flux at the Sudbury Neutrino Observatory with Enhanced Neutral Current Sensitivity”. In: *Phys. Rev. Lett.* 92 (2004), p. 181301.

[Arn87] Markus Arnold. “Messung der Lebensdauer freier Neutronen”. PhD thesis. Universität Heidelberg, 1987.

[Bae96] Stefan Baeßler. “Die Betaasymmetrie im Zerfall des freien Neutrons”. PhD thesis. Universität Heidelberg, 1996.

[Baz93] A.N. Bazhenov et al. “An adiabatic resonance spin-flipper for thermal and cold neutrons”. In: *Nuclear Instruments and Methods A* 334 (1993), pp. 534–536.

[Bég77] M. A. B. Bég et al. “Manifest Left-Right Symmetry and its Experimental Consequences”. In: *Phys. Rev. Lett.* 38.22 (1977), pp. 1252–1255.

[Bic] Bicron. *BC-400 / BC-404 / BC-408 / BC-412 / BC-416 Premium Plastic Scintillators, General Description*. Datasheet.

[Bir52] J.B. Birks. "Theory of the Response of Organic Scintillation Crystals to Short-Range Particles". In: *Phys. Rev.* 86.4 (1952), p. 569.

[Bir64] J.B. Birks. *The Theory and Practice of Scintillation Counting*. Pergamon Press, 1964.

[Boh32] Niels Bohr. "Faraday lecture. Chemistry and the quantum theory of atomic constitution". In: *J. Chem. Soc.* (1932), pp. 349–384.

[Bop86] Peter Bopp et al. "Beta-Decay Asymmetry of the Neutron and g_A/g_V". In: *Phys. Rev. Lett.* 56 (1986), pp. 919–922.

[BS53] J.B. Birks and M.E. Szendrei. "The Absolute Scintillation Efficiency of Anthracene". In: *Phys. Rev.* 91 (1953), pp. 197–198.

[CA11] D0 Collaboration and V. Abazov. "Search for W'->tb resonances with left- and right-handed couplings to fermions". In: (2011). eprint: `arXiv:1101.0806`.

[Cab63] Nicola Cabibbo. "Unitary Symmetry and Leptonic Decays". In: *Phys. Rev. Lett.* 10 (1963), pp. 531–533.

[Cha14] J. Chadwick. "The Intensity Distribution in Magnetic Spectrum of β-Rays of Radium B + C". In: *Verhandl. Dtsch. Phys. Ges.* 16 (1914), p. 383.

[Cha32] J. Chadwick. "The Existence of a Neutron". In: *Proceedings of the Royal Society of London. Series A* 136.830 (1932), pp. 692–708.

[Cho52] C.N. Chou. "The Nature of the Saturation Effect of Fluorescent Scintillators". In: *Phys. Rev.* 87.5 (1952), pp. 904–905.

[Dai] Daimler-Benz Aerospace, Dornier Satellitensysteme GmbH. *Neutron Velocity Selector, Blade rotor developed by Dornier/GKSS/PTB*. Datasheet.

[DG81] Savas Dimopoulos and Howard Georgi. "Softly broken supersymmetry and SU(5)". In: *Nuclear Physics B* 193.1 (1981), pp. 150–162.

[Döh90] J. Döhner. "Der Beta-Zerfall freier Neutronen und rechtshändige Ströme". PhD thesis. Universität Heidelberg, 1990.

[DS11] Dirk Dubbers and Michael G. Schmidt. "The neutron and its role in cosmology and particle physics". In: (2011). eprint: `arXiv:1105.3694`.

[Dub07] D. Dubbers et al. "A clean, bright, and versatile source of neutron decay products". In: (2007). DOI: `10.1016/j.nima.2008.07.157`. eprint: `arXiv:0709.4440`.

[Dub08a] D. Dubbers et al. “A clean, bright, and versatile source of neutron decay products”. In: *Nuclear Instruments and Methods A* 596 (2008), pp. 238–247.

[Dub08b] D. Dubbers et al. “The point spread function of electrons in a magnetic field, and the beta-decay of free neutrons”. In: (2008). eprint: `arXiv:0812.0347`.

[EM91] B.G. Erozolimsky and Yu.A. Mostovoi. “Determination of the coupling constants of beta decay from experimental data on decay of a free neutron”. In: *Sov. J. Nucl. Phys.* 53 (1991), pp. 260–262.

[ERM05] J. Erler and M.J. Ramsey-Musolf. “Low energy tests of the weak interaction”. In: *Progress in Particle and Nuclear Physics* 54.2 (2005), pp. 351–442.

[Fer34] Enrico Fermi. “Versuch einer Theorie der β-Strahlen”. In: *Zeitschrift für Physik* 88 (1934), p. 161.

[Fie37] Markus Fierz. “Zur Fermischen Theorie des β-Zerfalls”. In: *Zeitschrift für Physik A Hadrons and Nuclei* 104 (1937), pp. 553–565.

[Fir96] Richard B. Firestone. *Table of Isotopes*. Tech. rep. Lawrence Berkeley National Laboratory, 1996.

[FKK53] Milton Furst, Hartmut Kallmann, and Bernard Kramer. “Absolute Light Emission Efficiency of Crystal Anthracene for Gamma-Ray Excitation”. In: *Phys. Rev.* 89 (1953), pp. 416–417.

[Fri08] Felix Friedl. “Einfluss der Detektorfunktion auf die Messung des schwachen Magnetismus im Neutronzerfall”. Diploma thesis. Universität Heidelberg, 2008.

[GG74] Howard Georgi and S.L. Glashow. “Unity of All Elementary-Particle Forces”. In: *Phys. Rev. Lett.* 32.8 (1974), pp. 438–441.

[GJL95] F. Glück, I. Joó, and J. Last. “Measurable parameters of neutron decay”. In: *Nuclear Physics A* 593 (1995), pp. 125–150.

[Gla61] Sheldon L. Glashow. “Partial-symmetries of weak interactions”. In: *Nuclear Physics* 22.4 (1961), pp. 579–588.

[Glü11a] F. Glück. *Axis-symmetric magnetic field calculation with zonal harmonic expansion*. To be published. 2011.

[Glü11b] F. Glück. *Relativistic charged particle tracking with 8th order Runge-Kutta method*. To be published. 2011.

[GT36] George Gamow and Edward Teller. “Selection Rules for the β-Disintegration”. In: *Phys. Rev.* 49 (1936), pp. 895–899.

[GT92] F. Glück and K. Tóth. “Order-α radiative corrections for semileptonic decays of polarized baryons”. In: *Phys. Rev. D* 46.5 (1992), pp. 2090–2101.

[Häs02] H. Häse et al. “A long ballistic supermirror guide for cold neutrons at ILL”. In: *Nuclear Instruments and Methods A* 485.3 (2002), pp. 453–457.

[Hor11] Miklos Horvath. Personal communication. 2011.

[HT09] J.C. Hardy and I.S. Towner. “Superallowed $0^+ \to 0^+$ nuclear β decays: A new survey with precision tests of the conserved vector current hypothesis and the standard model”. In: *Phys. Rev. C* 79.5 (2009), p. 055502.

[Jac02] J.D. Jackson. *Klassische Elektrodynamik*. dritte, überarbeitete Auflage. de Gryuter, 2002. ISBN: 3-11-016502-3.

[JTW57] J.D. Jackson, S.B. Treiman, and Jr. H. Wyld. “Possible Tests of Time Reversal Invariance in Beta Decay”. In: *Phys. Rev.* 106 (1957), pp. 517–521.

[Kap07] Alexander Kaplan. “Preparing a weak magnetism measurement in free neutron decay with the new spectrometer PERKEO III”. Diploma thesis. Universität Heidelberg, 2007.

[KM73] Makoto Kobayashi and Toshihide Maskawa. “CP-Violation in the Renormalizable Theory of Weak Interaction”. In: *Progress of Theoretical Physics* 49.2 (1973), pp. 652–657.

[Kon10] G. Konrad et al. “Impact of Neutron Decay Experiments on non-Standard Model Physics”. In: (2010). eprint: `arXiv:1007.3027`.

[Kre04] Jochen Krempel. “Optimierung und Durchführung einer β-Asymmetriemessung im Zerfall polarisierter Neutronen”. Diploma thesis. Universität Heidelberg, 2004.

[Kre05a] Michael Kreuz et al. “A measurement of the antineutrino asymmetry B in free neutron decay”. In: *Physics Letter B* 619 (2005), pp. 163–270.

[Kre05b] Michael Kreuz et al. “The crossed geometry of two super mirror polarizers – a new method for neutron beam polarization and polarization analysis”. In: *Nuclear Instruments and Methods A* 547 (2005), pp. 583–591.

[Kre99] Michael Kreuz. "Test und Einbau eines Presampler-Kalorimeters für das Kleinwinkel-Neutronenkalorimeter FNC des H1-Experiments". Diploma thesis. Universität Heidelberg, 1999.

[Leo94] W.R. Leo. *Techniques for Nuclear and Particle Physics Experiments*. Springer-Verlag Berlin, 1994.

[Lia97] P. Liaud et al. "The measurement of the beta asymmetry in the decay of polarized neutrons". In: *Nuclear Physics A* 612 (1997), pp. 53–81.

[Liu10] J. Liu et al. "Determination of the Axial-Vector Weak Coupling Constant with Ultracold Neutrons". In: *Phys. Rev. Lett.* 105.18 (2010), p. 181803.

[LSI80] M.A. Lone, D.C. Santry, and W.M. Inglis. "MeV neutron production from thermal neutron capture in Li and B compounds". In: *Nuclear Instruments and Methods* 174 (1980), pp. 521–529.

[LY56] T.D. Lee and C.N. Yang. "Question of Parity Conservation in Weak Interactions". In: *Phys. Rev.* 104.1 (1956), pp. 254–258.

[Mar03] J. W. Martin et al. "Measurement of electron backscattering in the energy range of neutron β decay". In: *Phys. Rev. C* 68.5 (2003), p. 055503.

[Mär06] Bastian Märkisch. "Das Spektrometer PERKEO III und der Zerfall des freien Neutrons". PhD thesis. Universität Heidelberg, 2006.

[Mär11a] Bastian Märkisch. Personal communication. 2011.

[Mär11b] Bastian Märkisch. "Experimental Status of V_{ud} from Neutron Decay". In: *CKM2010, the 6th International Workshop on the CKM Unitarity Triangle*. 2011.

[Max65] James Clerk Maxwell. "A Dynamical Theory of the Electromagnetic Field". In: *Phil. Trans. R. Soc. Lond.* 155 (1865), pp. 459–512.

[MM09] Bastian Märkisch and Holger Mest et al. "The new neutron decay spectrometer PERKEO III". In: *Nuclear Instruments and Methods A* 611 (2009), pp. 216–218.

[Mos01] Y.A. Mostovoi. "Experimental value for G_A/G_V from a measurement of both p-odd correlations in free neutron decay". In: *Phys. At. Nucl.* 64 (2001), p. 1955.

[MS06] W.J. Marciano and Alberto Sirlin. "Improved Calculation of Electroweak Radiative Corrections and the Value of V_{ud}". In: *Phys. Rev. Lett.* 96.3 (2006), p. 032002.

[Mun06] Daniela Mund. “Messung der Betaasymmetrie A im Neutronenzerfall”. PhD thesis. Universität Heidelberg, 2006.

[Nac86] Otto Nachtmann. *Phänomene und Konzepte der Elementarteilchenphysik*. Vieweg Verlag, 1986. ISBN: 3-528-08926-1.

[Ndb] *Neutron Data Booklet*. Institut Laue-Langevin. 2003.

[NG10] K Nakamura and Particle Data Group. “Review of Particle Physics”. In: *Journal of Physics G: Nuclear and Particle Physics* 37.7A (2010), p. 075021.

[NI10] J. Nilsson and M. Isaksson. “A comparison between Monte Carlo-calculated and -measured total efficiencies and energy resolution for large plastic scintillators used in whole-body counting”. In: *Radiation Protection Dosimetry* (2010), pp. 1–5.

[Pai77] A. Pais. “Radioactivity’s two early puzzles”. In: *Rev. Mod. Phys.* 49.4 (1977), pp. 925–938.

[Pic10] A. Pichlmaier et al. “Neutron lifetime measurement with the UCN trap-in-trap MAMBO II”. In: *Physics Letters B* 693.3 (2010), pp. 221–226.

[Plo00] Christian Plonka. “Verbesserung der Lichtauskopplung zur Messung der Neutrinoasymmetrie mit PERKEO II”. Diploma thesis. Universität Heidelberg, Jan. 2000.

[PRMT07] S. Profumo, M. J. Ramsey-Musolf, and S. Tulin. “Supersymmetric contributions to weak decay correlation coefficients”. In: *Phys. Rev. D* 75.7 (2007), p. 075017.

[Rav95] Carsten Raven. “Erste Messungen mit Perkeo II: β-Asymmetrie im Neutron-Zerfall”. Diploma thesis. Universität Heidelberg, 1995.

[Rei99] Jürgen Reich. “Winkelkorrelationen im Zerfall polarisierter Neutronen”. PhD thesis. Universität Heidelberg, 1999.

[RMS08] M.J. Ramsey-Musolf and S. Su. “Low-energy precision tests of supersymmetry”. In: *Physics Reports* 456 (2008), pp. 1–88.

[Roi10] Christoph Marcus Roick. “Simulation von Elektronenbahnen in PERKEO III”. Bachelor thesis. Universität Heidelberg, 2010.

[Rus08] Rudolf Rusnyak. *Analog Part of Circuit Diagram SU717*. Circuit Diagram. 2008.

[SA08] Marc Schumann and Hartmut Abele. “Unrecognized backscattering in low energy beta spectroscopy”. In: *Nuclear Instruments and Methods A* 585.1-2 (2008), pp. 88–92.

[Sal68] A. Salam. *Elementary Particle Theory*. Almquist & Wiksells, 1968.

[SBNC06] Nathal Severijns, Marcus Beck, and Oscar Naviliat-Cuncic. “Tests of the standard electroweak model in nuclear beta decay”. In: *Rev. Mod. Phys.* 78.3 (2006), p. 991.

[Sch04] Marc Schumann. “Probing the Standard Model: Preparation of a new Electron Asymmetry Measurement in the Decay of Polarized Neutrons”. Diploma thesis. Universität Heidelberg, 2004.

[Sch07a] Marc Schumann. “Measurement of Neutrino and Proton Asymmetry in the Decay of polarized Neutrons”. PhD thesis. Universität Heidelberg, 2007.

[Sch07b] Marc Schumann et al. “Measurement of the Neutrino Asymmetry Parameter *B* in Neutron Decay”. In: *Phys. Rev. Lett.* 99.19 (2007), p. 191803.

[Sch08] Marc Schumann et al. “Measurement of the Proton Asymmetry Parameter in Neutron Beta Decay”. In: *Phys. Rev. Lett.* 100.15 (2008), p. 151801.

[Ser05] A.P. Serebrov et al. “Measurement of the neutron lifetime using a gravitational trap and a low-temperature Fomblin coating”. In: *Physics Letter B* 605 (Jan. 2005), pp. 72–78.

[Sol11] Torsten Soldner. Personal communication. 2011.

[SPP02] T. Soldner, A. Petoukhov, and C. Plonka. *Installation and first tests of the new PF1b polariser*. Tech. rep. ILL03SO10T. ILL Grenoble, 2002.

[SS89] O. Schaerpf and N. Stuesser. “Recent progress in neutron polarizers”. In: *Nuclear Instruments and Methods A* 284 (1989), pp. 208–211.

[Sur97] R. Surkau et al. “Realization of a broad band neutron spin filter with compressed, polarized ^{3}He gas”. In: *Nuclear Instruments and Methods A* 384 (1997), pp. 444–450.

[VA72] D.V. Volkov and V.P. Akulov. “Possible universal neutrino interaction”. In: *JETP Lett.* 16 (1972), pp. 438–440.

[Wei67] Steven Weinberg. “A Model of Leptons”. In: *Phys. Rev. Lett.* 19.21 (1967), pp. 1264–1266.

[Wei92] Steven Weinberg. *Dreams of a final theory*. 1st ed. Pantheon Books, New York, 1992. ISBN: 0679419233.

[Wer09] Dominik Werder. "Development and Characterization of a Pulsed Beam for Neutron Decay Experiments". Diploma thesis. Universität Heidelberg, 2009.

[Wie05] F.E. Wietfeldt et al. "A backscatter-suppressed beta spectrometer for neutron decay studies". In: *Nuclear Instruments and Methods A* 538 (2005), pp. 574–591.

[Wil82] D.H. Wilkinson. "Analysis of neutron β-decay". In: *Nuclear Physics A* 337 (1982), pp. 474–504.

[Wu57] C. S. Wu et al. "Experimental Test of Parity Conservation in Beta Decay". In: *Phys. Rev.* 105.4 (1957), pp. 1413–1415.

[Yer97] B. Yerozolimsky et al. "Corrigendum: Corrected value of the beta-emission asymmetry in the decay of polarized neutrons measured in 1990". In: *Physics Letter B* 412.3 (1997), p. 240.

[Yuk35] Hideki Yukawa. "On the interaction of elementary particles". In: *Proc. Phys. Math. Soc. Jap.* 17 (1935), pp. 48–57.

[Zim99] Oliver Zimmer. "A method for precise neutron beam polarisation analysis using an opaque spin filter". In: *Physics Letter B* 461 (1999), pp. 307–314.